Atomic Scale Influences on the Tribology of Nano to Meso-scale Systems

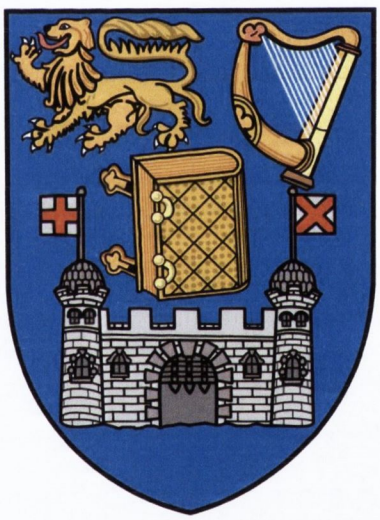

PhD thesis

2014

James Annett

I declare that this thesis has not been submitted as an exercise for a degree at this or any other university and it is entirely my own work.

I agree to deposit this thesis in the University's open access institutional repository or allow the library to do so on my behalf, subject to Irish Copyright Legislation and Trinity College Library conditions of use and acknowledgement.

James [illegible] 29/4/15

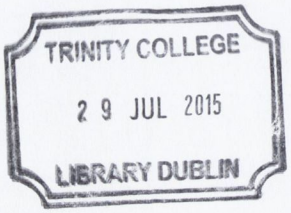

Acknowledgements

I would sincerely like to thank my supervisor Prof Graham Cross for the opportunity to pursue a PhD within his research group. His guidance, encouragement and support have been invaluable to me through the years. I have greatly benefited from his hard work, dedication, clarity of thought and his uncompromising high standards of experimental science for which I am very grateful. By extension I would like to thank all the past and present members of the Cross group who have assisted in my work. In particular I thank Evelyn Doherty, Roseanne Reilly and Johann de Silva for their assistance in experimental design and the interpretation of results. I would like to thank Alexis Potie for all of his assistance with AFM.

I have greatly benefited from collaborations with colleagues from the University of Tennessee. In particular I thank Dr Barry Lucas for all of his help in the understanding and operation of the 3D nano contact system. I thank Prof Yan Fei Gao for the development of his contact theory which proved to be very useful in understanding the behaviour of nano-scale contacts. I thank Prof Erik Herbert and Prof Warren Oliver for their assistance in understanding nanoindentation methodologies.

I am grateful for the funding I have received through SFI and the opportunity to pursue my research within CRANN which is a world class institution which boasts excellent facilities and a great working environment. I am also very grateful to the school of physics for the education I have received throughout my years of study. I would like to thank Prof George Deusberg for the use of his facilities, in particular the Raman spectrometer. I sincerely thank Hugo Nolan and Dr Niall Mc Evoy for their assistance and useful discussions surrounding Raman spectroscopy.

I would like to express my gratitude to my parents, George and Nuala Annett who have enthusiastically supported me in the pursuit of the PhD. I also express my gratitude to Lavinia Forde for her encouragement and support and to all of my friends and family.

Abstract

It has been known for many years that atomic scale effects can directly influence the tribological behaviour over a wide variety of contact sizes ranging from the nano-scale to macroscale. A newly developed load and depth sensing three dimensional nano-contact system has been used to investigate and experimentally characterise new ways in which atomic scale properties can influence the behaviour of nano to meso-scale contacts in room temperature ambient conditions. The 3D nano-contact system involves conventional indentation deformation normal to the surface with oscillations superimposed in the lateral direction which allows for the investigation of the tribological behaviour of over contact sizes which range from the nano to meso-scale. The 3D contact system was used to measure the friction anisotropy of single crystal Ni in nano to meso-scale contacts. This friction anisotropy is a direct result of the arrangement of the atomic crytsal structure. The 3D contact system was also used to invetigate the the role of graphene, a layer of carbon atoms bonded in a 2D plane, as a protective lubricating coating in nano to meso-scale contacts. Even a single atomic layer of graphene was found to have excellent lubricating properties when placed between contacting surfaces. The integrity of the lubrication was maintained up to high contacting pressures of up to 10GPa. Finally a novel self-assembly phenomenon in graphene was discovered which involves the spotaneous and directed folding, sliding and fracture of graphene resulting in folded strucutres. Using the available values, within the literature, of the surface interactions, the elastic strain energy and the cost of fracturing the graphene lattice we have formulated a theory which predicts the energetic favourability of the spontaneous growth of the folded structures. The phenomenon may extend to a broad class of 2D materials, and may have uses in lithography and nano-electromechanical devices (NEMS). The phenomenon may also provide a new route for studying the mechanical properties of 2D materials such as folding, fracture and adhesion.

Table of contents

Table of figures

Symbols used

σ_{ij}	Normal stress (GPa)
τ_{ij}	Shear stress (GPa)
A_0	Cross sectional area
P	Applied normal load (N)
T	Applied tangential load (N)
L	Length of a crack
L_i	Initial length of a crack
ΔL	Change in length of a crack
ν	Poisson's ratio
ε_{ij}	Normal strain
γ_{ij}	Shear strain
E	Youngs modulus (GPa)
G	Shear modulus (GPa)
σ_h	Hydrostatic pressure
σ_d	Deviatoric stress
F	Force (N)
μ	Coefficient of friction
A_{real}	Real contact area
A_{asp}	Area of single asperity
δ_z	Normal indentation displacement

$\delta_{x/y}$	Lateral displacement
δ_{z_c}	Projected contact depth
δ_{z_f}	Depth of final impression
A_c	Projected contact area
K_f	Stiffness of the indenter frame (N/m)
K_i	Stiffness of the indenter support springs (N/m)
K_c	Contact stiffness (N/m)
K_{tot}	Total stiffness (N/m)
D_i	Damping coefficient of indenter (Ns/m)
D_c	Damping coefficient of the contact (Ns/m)
D_{tot}	Total damping coefficient (Ns/m)
ϕ	Phase angle
S_z	Normal stiffness (N/m)
S_x	Lateral stiffness (N/m)
E^*	Reduced modulus (GPa)
G^*	Reduced shear modulus (GPa)
a	Radius of projected contact area
c	Radius of the projected area of the stick zone
$\delta_{x,elastic}$	Elastic tangential displacement
$\delta_{x,slip}$	Tangential slip
τ_0	Interfacial shear strength (GPa)
U	Total energy of the system (joule)
$U_{elastic}$	Stored elastic energy (Joule)

$U_{fracture}$	Energy cost associated with advance of fracture (J/m)
$F_{fracture}$	Fracture force associated with the graphene lattice
$U_{surface}$	Energy associated with surface interactions
$F_{surface}$	Force associated with the change in the surfaces
U_{fold}	Energy stored within the fold
F_{fold}	Force associated with the folded graphene lattice
R	Radius of the folded graphene
κ	Curvature of the fold
ψ	Rate of bond dissociation
k_b	Boltzman's constant
h	Planks constant
v	Velocity of crack front
v_0	Rate constant
a_0	Lattice spacing
ΔE_{ZZ}	Fracture toughness of graphene (Zig-Zag)
ΔE_{AC}	Fracture toughness of graphene (Armchair)
t	Time

Chapter 1: Introduction

1.1 Introduction and outline

Nanotechnology involves the exploitation of physical properties of materials with spatial dimensions on the order of 100nm or less. In recent years, huge interest has been placed on the mechanical, optical, thermal and electronic properties of low dimensional materials such as quasi 0D dots, quasi 1D nanotubes or wires however since the discovery of graphene, in 2004, the properties of quasi 2D sheets have been aggressively investigated which was initially motivated by the exotic electronic properties of graphene [1-3]. The electronic properties of graphene are strongly dependant on the contacting substrate since the roughness and charge impurities present on SiO_x have resulted in inferior electronic properties in comparison to suspended graphene [4]. Very recently it has been demonstrated that 2D dialectic crystals such as hBN can provide excellent substrates for preserving the intrinsic electronic properties of graphene [5], which is due to the atomically smooth surfaces which are free from dangling bonds or charge traps. For this reason attention has been focused on the entire family of quasi 2D materials which includes graphene, hBN and transition metal dichalcogenides (TMD's) and in particular how the intrinsic properties of individual sheets can be isolated and/or married together in heterostructures which may be fabricated in working devices [6].

Graphene and other 2D sheets have also exhibited remarkable mechanical properties with exceptional strength [7], frictional and wear properties [8-9]. For this reason graphene has been purposed as a protective, dry lubricating coating in micro and nano electromechnical devices (MEMS/NEMS) [10]. Dry lubrication in nano-scale contacts are advantageous in comparison to liquid lubrication because solids resist wear under demanding environmental conditions such as high stress and elevated temperatures where loss of lubrication due to evaporation is prohibited. Other advantageous are also afforded over liquid lubrication in nano-scale contacts since viscous effects and squeeze out are avoided [11].

In general the mechanical properties of nano-scale contacts are crucial to the fabrication and operation of nano-scale devices since new scalable, high yield, fabrication techniques

are required to build scalable working devices [12]. The focus of the thesis is on the investigation and experimental characterisation of new ways in which atomic scale properties can directly influence the behaviour of nano to meso-scale contacts in room temperature ambient conditions. This has been investigated in three ways. First the friction and elastic anisotropy of a single crystal Ni in air was measured using a newly developed unique 3D nano-contact system. Easy slip was found along the [110] direction which suggests Schmid type behaviour where easy glide occurs along the close pack direction, which is described in chapter 2. Second the role of graphene as a lubricating protective coating in nano to meso-scale contacts was investigated. Even a single atomic layer of graphene was found to lubricate the surface of the SiO_x substrate under large average contact pressures of up to 10 GPa, the details of which are described in chapter 3. Finally a novel self-assembly process in graphene was discovered which involves the spontaneous and directed reorganisation of graphene into self assembled folded structures through folding, sliding and fracture. Using the available values, within the literature, of the surface interactions, the elastic strain energy and the cost of fracturing the graphene lattice we have formulated a theory which predicts the energetic favourability of the growth of the folded structures. Based on this theory we believe the self-assembly process is ultimately driven by a reduction of the free energy of the graphene sheet by the reduction of the area of the exposed graphene surface. A comprehensive theoretical model, along with the experimental results, is provided in chapter 4. A discussion and description of the concepts and the experimental techniques is presented in the remaining sections of this chapter.

1.2 Literature review

Tribology is the study of the mechanics of moving interfaces which involves the principals of lubrication, wear, adhesion, elastic and plastic deformation between the contacting surfaces. The purpose of this literature review is to briefly discuss some of the most significant published work in the area of nano tribology which is relevant to the work presented within this thesis. It has been known for centuries that the friction forces between macroscopic bodies in contact is independent of the contact area and linearly dependent upon the compressive load which was first summarized by Amonton [13]. This apparent contradiction can be understood by distinguishing between the real and apparent contact area which was first proposed by Bowden and Tabour [14]. They suggest that any macroscopic surface contains

local hills and valleys resulting in small local contact areas within the macroscopic contact, known as asperities. The Bowden and Tabour model assumes that the friction force can be determined by taking the product of the real contact area and the interfacial shear strength τ_0 [15]. The friction force is the result of energy loss during sliding and is therefore referred to as plastic deformation. Bowden and Tabour investigated the sliding behaviour of dry metallic surfaces and demonstrated the "stick slip" behaviour which generates heat during sliding, illustrating the detailed nature of interfacial sliding [16]. The central aim of tribology is to fully understand the nature of the interface and to determine the associated deformation and energy dissipation mechanisms [17].

Traditional tribological instruments, such as tribometers or surface force apparatus measure the tribological properties of macroscopic surfaces. The scanning tunnelling microscope (STM) led to the development of the atomic force microscope (AFM) which is used to measure forces between an atomically sharp tip and any chosen surface [18]. It was soon realised that the AFM could be used to measure friction forces between the tip and the sample, known as friction force microscopy (FFM) [19]. Before the development of the AFM tribology was studied on effectively macroscopic surfaces which means the interfacial behaviour must be averaged over the apparent contact area making it difficult to determine the fundamental deformation and energy dissipation mechanisms during sliding [20-21]. However the size of AFM tips range between the atomic scale and 100nm which ensures that single asperity contacts are made between the tip and the sample which has proven to be very useful in investigating the fundamental deformation and energy dissipation mechanisms associated with interfacial sliding.

The arrangement of the lattice and the registry between crystalline contacts continues to be an ongoing area of enquiry which can have dramatic effects on the tribology of the contacts [22]. Friction anisotropy refers to the orientation dependence on the friction between crystalline contacts which has been reported on a large number of materials [23-25]. Superlubricity is a remarkable phenomenon, related to friction anisotropy, whereby the friction force becomes vanishingly small as the contact transitions from commensurability to an incommensurate state which was first reported by Hirano and Shinjo in 1991 [26-27]. Superlubricity has been

rigorously studied since 1991 and has been reported on a number of interfaces [28-32]. The principal has also been demonstrated between graphite surfaces on a 10μm length scale [33-36].

In addition to structural lubricity, third body lubrication is of major importance to the field of tribology which is of both tremendous practical and scientific importance. The study of third body lubrication presents an opportunity to investigate how stress is transmitted and how deformation mechanisms occur across complex interfaces. Lubrication is most commonly achieved by adding liquid to the interface. Experiments have shown that the tribological behaviour of liquids can be dramatically different from the bulk value when confined to the nanoscale [37]. Experiments have also shown that the presence of atmospheric gasses can alter the tribological properties of materials [38]. Since the discovery of graphene in 2004 [39], the friction characteristics of atomically thin sheets have come under increased scrutiny [9, 40-45]. Atomically thin sheets have been shown to alter the tribology of contacts, exhibiting exceptional friction and wear characteristics which may be of particular interest in engineering protective coatings on nanoscale contacts [10].

Tribology continues to be an area of active research, the ultimate aim of which is to understanding all of the length, time and temperature scale dependencies as well as the fundamental deformation and energy dissipation mechanisms associated with interfacial mechanics.

1.3 Continuum mechanics

Continuum mechanics is the study of the deformation of mater which is based on the concepts of stress, strain, elasticity, plasticity and the failure of materials. Contact mechanics is the study of the deformation of mater under the application of an external load (P) through contacting surfaces. The relationship between the applied load and the resultant deformation is usually described in terms of stress and strain because stress and strain relate the deformation to the intrinsic, non dimensional, properties of the material. A standard example, which illustrates the concept of stress and strain, is the case of uniaxial uniform tension acting on a cylindrical bar with uniform cross sectional area [46], which is shown by the schematic in Figure 1.3.1.

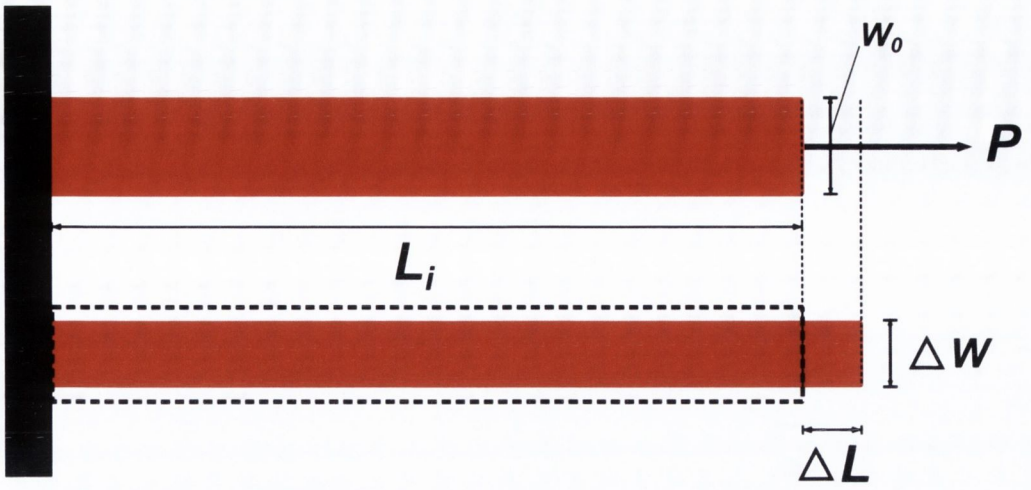

Figure 1.3.1: Schematic representation of the application of uniform tension acting upon a cylindrical bar with uniform cross sectional area.

The average stress, or engineering stress, is defined by the applied load (P) divided by the cross setional area (A_0) which is given by

$$\sigma = \frac{P}{A_0} \tag{1.1}$$

The engineering strain (ε) is a measurement of the average deformation within the deformed volume and is given by

$$\varepsilon = \frac{\Delta L}{L_i} \tag{1.2}$$

where L_i is the initial length of the cylinder and ΔL is the change in length under the application of the stress.

Any strain parallel to the direction of the applied stress will produce a strain in the lateral direction due to the change in the volume of the specimen, which is shown schematically in Figure 1.2.1. Poisson's ratio is defined as the ratio of the lateral strain divided by the normal strain [46] which is given by

$$\nu = \frac{\varepsilon_{\perp}}{\varepsilon_{\square}} \tag{1.3}$$

The Young's or elastic modulus (E) is defined as the ratio of the stress to strain which is a measurement of the intrinsic elasticity of a specimen [46], given by

$$E = \frac{\sigma}{\varepsilon} \tag{1.4}$$

A schematic representation of the stress strain response of a ductile material under uni-axial tension acting over a uniform cross sectional area is shown below in Figure 1.3.2. The initial linear loading section of the stress strain curve results in elastic deformation which is fully recoverable upon the removal of the applied stress. The slope of the initial linear response is equal to the Young's modulus and represents a measurement of the intrinsic elasticity of the material. If the material is loaded beyond the yield stress (σ_0) the material will deform plastically which results in permanent residual deformation.

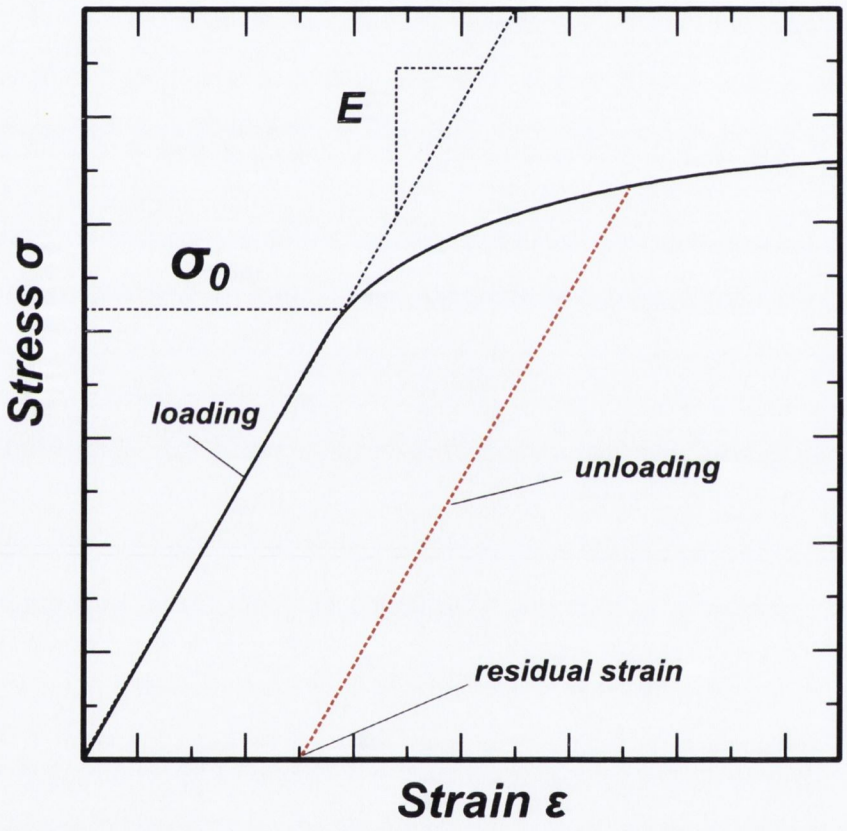

Figure 1.3.2: Schematic representation of the stress strain response of a cylindrical bar with uniform cross sectional area under tension.

In general the state of stress between contacts is not uniform, usually resulting in a complex state of stress which varies in magnitude and direction within the deformed volume. The state of stress on an infinitesimal element of material can be resolved into components perpendicular to the faces of the element, which are called normal stress's (σ), and components parallel with the faces of the element, which are called shear stresses (τ) which is shown schematically in Figure 1.3.3.

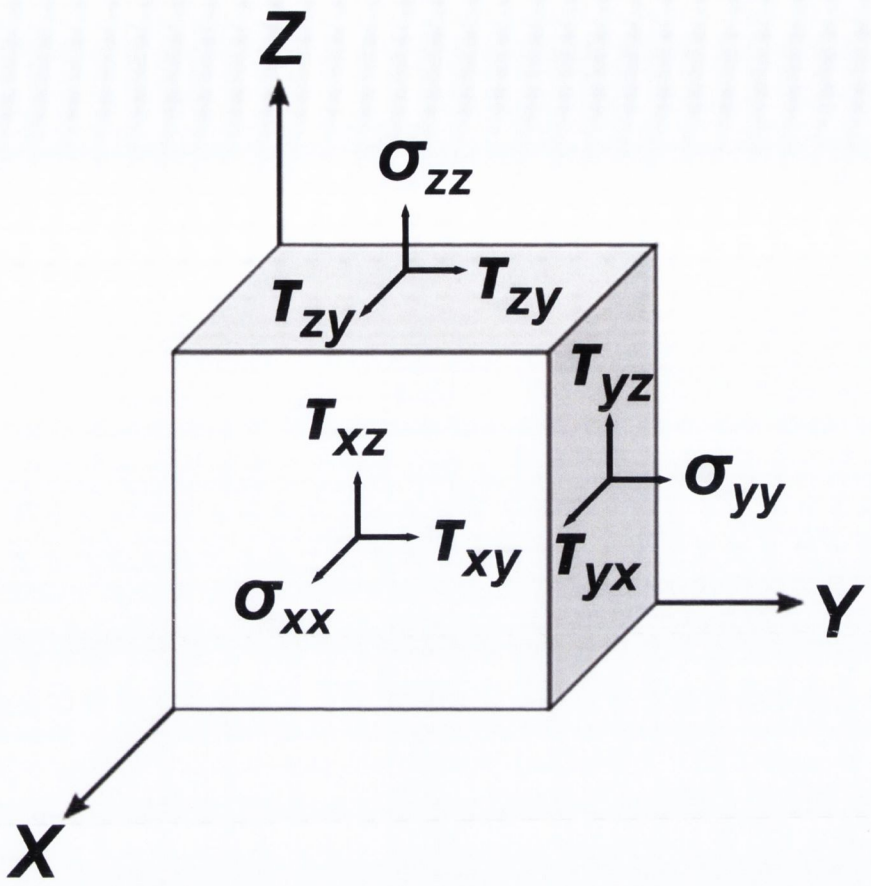

Figure 1.3.3: Schematic representation of the state of stress on an element.

Nine components of stress are required to fully define the state of stress which is given in matrix form [46] by

$$\begin{bmatrix} \sigma_{xx} & \tau_{xy} & \tau_{xz} \\ \tau_{xy} & \sigma_{yy} & \tau_{zy} \\ \tau_{xz} & \tau_{yz} & \sigma_{zz} \end{bmatrix} \tag{1.5}$$

A significant simplification can be made by considering the equilibrium condition where summing the moment of forces about each yields

$$\begin{aligned} \tau_{xz} &= \tau_{zx} \\ \tau_{yz} &= \tau_{zy} \\ \tau_{xy} &= \tau_{yx} \end{aligned} \tag{1.6}$$

Under equilibrium conditions the state of stress is defined by a total of 6 components, $\sigma_{xx}, \sigma_{yy}, \sigma_{zz}, \tau_{xy}, \tau_{yz}, \tau_{xz}$.

The complex stress state results in a complex, non uniform, state of strain. Strain is a measure of the deformation of a specimen which is represented schematically in Figure 1.3.4. The point B which resides within the specimen in an un-deformed state, undergoes a displacement u_x, u_y, u_z along the X, Y and Z axes, to the point B' under the application of stress. The linear strains along each axis is given by

$$\varepsilon_x = \frac{du_x}{dx}$$
$$\varepsilon_y = \frac{du_y}{dy} \tag{1.7}$$
$$\varepsilon_z = \frac{du_z}{dz}$$

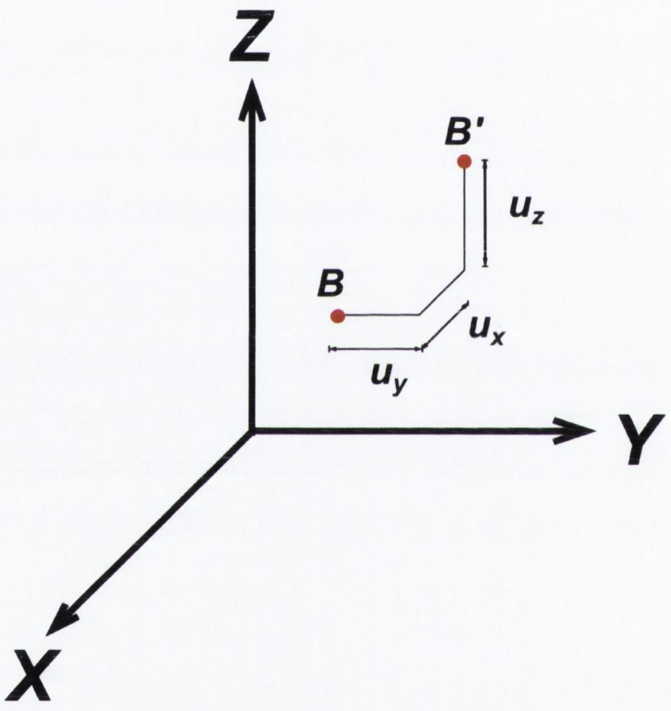

Figure 1.3.4: Schematic representation of the strain at a point B, which undergoes a displacement u_x, u_y, u_z along the X, Y and Z axes to a position B'.

In general the deformation within the volume will result in shear strain. The shear strain along the X,Y plane is represented in Figure 1.3.5 which results in a distortion of an element as the point B undergoes the displacement to B'. The shear strain along each direction is given by

$$\varepsilon_{xy} = \frac{1}{2}\left(\frac{du_x}{dy} + \frac{du_y}{dx}\right)$$
$$\varepsilon_{yz} = \frac{1}{2}\left(\frac{du_y}{dz} + \frac{du_z}{dy}\right) \tag{1.8}$$
$$\varepsilon_{xz} = \frac{1}{2}\left(\frac{du_x}{dz} + \frac{du_z}{dx}\right)$$

The shear modulus (G) is usually defined in terms of the engineering shear strain (γ) which is given by

$$G_{ij} = \frac{\tau_{ij}}{\gamma_{ij}} = \frac{\tau_{ij}}{2\varepsilon_{ij}} \tag{1.9}$$

where

$$\gamma_{ij} = 2\varepsilon_{ij} \tag{1.10}$$

where the subscripts i and j refer to the direction.

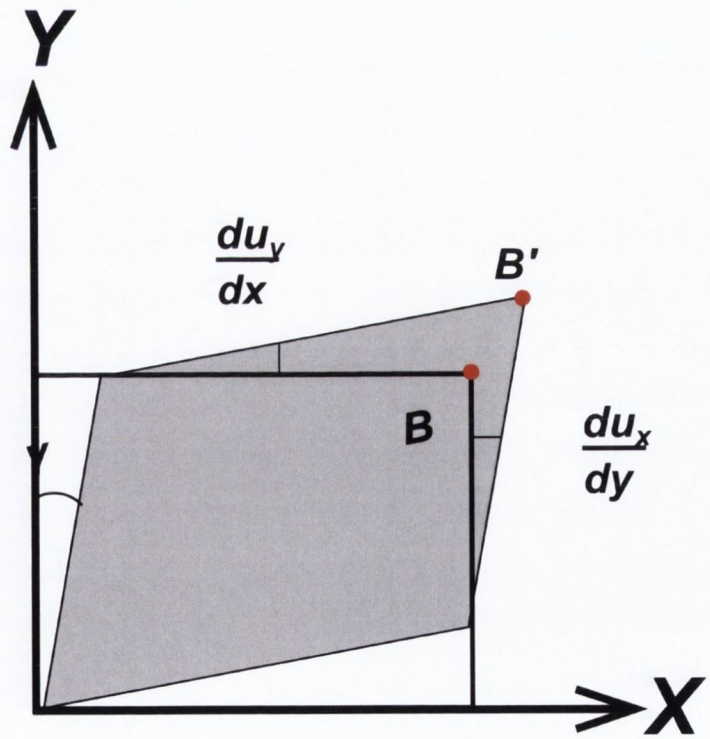

Figure 1.3.5: Schematic representation of shear strain in the X,Y plane as the point B undergoes displacement to the point B'.

The state of strain can be written in tensor form given by

$$\begin{bmatrix} \varepsilon_x & \varepsilon_{xy} & \varepsilon_{xz} \\ \varepsilon_{xy} & \varepsilon_y & \varepsilon_{zy} \\ \varepsilon_{zx} & \varepsilon_{yz} & \varepsilon_z \end{bmatrix} \tag{1.11}$$

Similar to the state of complex stress, the state of strain can be represented by 6 components of strain because the strain matrix is symmetrical where

$$\begin{aligned} \varepsilon_{xy} &= \varepsilon_{yx} \\ \varepsilon_{xz} &= \varepsilon_{zx} \\ \varepsilon_{zy} &= \varepsilon_{yz} \end{aligned} \tag{1.12}$$

The stress is related to the strain by 36 elastic constants (C_{ij}) given by

$$\begin{bmatrix} \sigma_{xx} \\ \sigma_{yy} \\ \sigma_{zz} \\ \tau_{xz} \\ \tau_{yz} \\ \tau_{xy} \end{bmatrix} = \begin{bmatrix} C_{11} & C_{21} & C_{31} & C_{41} & C_{51} & C_{61} \\ C_{12} & C_{22} & C_{32} & C_{42} & C_{52} & C_{62} \\ C_{13} & C_{23} & C_{33} & C_{43} & C_{53} & C_{63} \\ C_{14} & C_{24} & C_{34} & C_{44} & C_{54} & C_{64} \\ C_{15} & C_{25} & C_{35} & C_{45} & C_{55} & C_{65} \\ C_{16} & C_{26} & C_{36} & C_{46} & C_{56} & C_{66} \end{bmatrix} \begin{bmatrix} \varepsilon_{xx} \\ \varepsilon_{yy} \\ \varepsilon_{zz} \\ \gamma_{xz} \\ \gamma_{yz} \\ \gamma_{xy} \end{bmatrix} \tag{1.13}$$

Further simplifications of the constants can be made by considering the symmetry of the crystal planes. An elastically isotropic material is one that has the same elastic properties in all directions which simplifies the elastic solutions significantly [46]. The application of a general state of stress on an elastically isotropic material is given by

$$\begin{bmatrix} \sigma_{xx} \\ \sigma_{yy} \\ \sigma_{zz} \\ \tau_{xz} \\ \tau_{yz} \\ \tau_{xy} \end{bmatrix} = \begin{bmatrix} 1/\mathrm{E} & -\nu/E & -\nu/\mathrm{E} & 0 & 0 & 0 \\ -\nu/E & 2/E & -\nu/E & 0 & 0 & 0 \\ -\nu/E & -\nu/\mathrm{E} & 1/E & 0 & 0 & 0 \\ 0 & 0 & 0 & 1/G & 0 & 0 \\ 0 & 0 & 0 & 0 & 1/G & 0 \\ 0 & 0 & 0 & 0 & 0 & 1/G \end{bmatrix} \begin{bmatrix} \varepsilon_{xx} \\ \varepsilon_{yy} \\ \varepsilon_{zz} \\ \gamma_{xz} \\ \gamma_{yz} \\ \gamma_{xy} \end{bmatrix} \tag{1.14}$$

The general state of stress within an element can be resolved into hydrostatic and deviatoric stresses. The hydrostatic stress (σ_h) is responsible for the uniform compression or tension along all three axes [47] and can be defined by

$$\sigma_h = \frac{\sigma_x + \sigma_y + \sigma_z}{3} \tag{1.15}$$

The deviatoric stress (σ_d) is responsible for the distortion or shape change of the element [47] which is given by

$$\begin{aligned}\sigma_{dx} &= \sigma_x - \sigma_h \\ \sigma_{dy} &= \sigma_y - \sigma_h \\ \sigma_{dz} &= \sigma_z - \sigma_h\end{aligned} \tag{1.16}$$

If only hydrostatic stresses are present, no shear stresses are generated and no plastic deformation will occur however if deviatoric stresses are present the shear stress may be sufficient to cause plastic deformation. The minimum stress which results in plastic deformation is called the yield stress (σ_0). The onset of plasticity continues to be an area of active research because the yield stress, unlike elasticity, is not an intrinsic material property. The yield stress is heavily dependent on the population and concentration of defects. The Von Mises yield criterion establishes the state of stress which gives rise to plastic flow [47], and is given by

$$\sigma_0 = \sqrt{\frac{1}{2}\left[\left(\sigma_x - \sigma_y\right)^2 + \left(\sigma_y - \sigma_z\right)^2 + \left(\sigma_z - \sigma_x\right)^2\right]} \tag{1.17}$$

1.4 Tribology

Friction is an everyday experience from which we form much of the basis of our tactile intuitions. For this reason friction has been studied for centuries and continues to be an area of scientific investigation to this day. The relative sliding between two surfaces in contact is sensitive to many conditions such as the contacting area [48], contacting geometries [49], temperature [50], charge transfer [51], chemical bonding, states of interfacial stress [52] as well as environmental conditions such as lubricating films of liquid or even atomic layers of environmental molecules between the contacting surfaces. Friction is also of major importance to any field of engineering or technology with moving contacting bodies where lubrication and the reduction of wear may be economically and functionally advantageous. Triboloy is the study of moving interfaces involving adhesion, friction, lubrication and wear which encompasses centuries of experimental and theoretical research the aim of which is to understand the fundamental deformation and energy dissipation mechanisms of moving interfaces.

According to the well known Amoton's law the friction force, F_f , experienced by the relative sliding between macroscopic surfaces in contact is, counter intuitively, independent of the macroscopic contact area and linearly proportional to the normal compressive load acting between the surfaces which is given by

$$F_f = \mu P \tag{1.18}$$

where μ is the friction coefficient and P is the compressive load normal to the contacting surfaces.

This relationship can be understood by differentiating between the real and the apparent contact areas which was originally proposed by Bowden and Tabour [48], and is shown schematically in Figure 1.3.1. The surfaces of macroscopic bodies are generally very rough which introduces a statistical variation in the topography of the contacting surfaces. This variation ensures that only a relatively small fraction of the contacting surfaces are close enough to interact significantly over an area, A_{asp} , which is called an asperity and is shown by the schematic in Figure 1.4.1 (b). The real contact area, A_{real} , between the surfaces can then be defined by the summation of the asperities within the apparent contact area which is given by

$$A_{real} = \sum A_{asp} \tag{1.19}$$

The contact area of the single asperity, and by extension the real contact area, will be dependent on the compressive load and the elastic and adhesive properties of the contacting surfaces however approximating each asperity as a spherical contact the area of each asperity is proportional to the compressive load raised to the power of 2/3 which is given by

$$A_{asp} \propto P^{\frac{2}{3}} \tag{1.20}$$

The interfacial shear strength (τ_0) is defined as friction force per unit area. The friction force between the two macroscopic surfaces is then given by

$$F_f = \tau_0 A_{real} \tag{1.21}$$

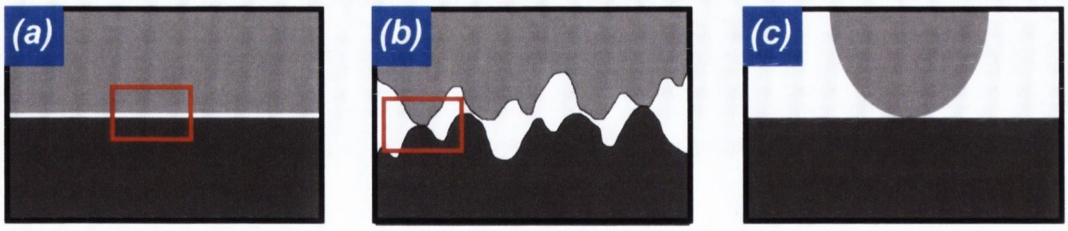

Figure 1.4.1: Schematic representation of (a) the apparent contact area of macroscopic surfaces in contact, (b) asperities within the apparent contact area and (c) Hertzian approximation of a single asperity contact.

Differentiating between the real and the apparent contact area remains a challenging aspect of tribology [48-49]. The fundamental deformation and energy dissipation mechanisms during sliding are critical to the understanding of the sliding behaviour, for example the sliding behaviour of contacting surfaces can be dramatically reduced by the presence of adsorbed molecules between the interface [38] alternatively the friction force can be increased by the presence of a liquid film due to viscous effects or capillary forces [53]. The complexity of the rough contacting geometries provides challenging experimental conditions towards understanding of the fundamental deformation mechanisms of interfacial sliding. For this reason tribological experiments are often conducted on single asperity nano scale contacts where the fundamental energy dissipation mechanisms of sliding can be investigated [54].

The sliding of two atomically smooth surfaces in contact can be understood in terms of the Tomlinson model [22] where the relative sliding between surfaces results in overlapping periodic potentials which must be overcome in order for the two surfaces to move relative to one another. A simple 1D schematic representation of the sliding of commensurate surfaces is shown in Figure 1.4.2 (a) where the lattice spacing's are perfectly matched. Each contacting atom remains in an energy minimum, E_0. The force required to overcome the energy barrier in the commensurate state, F_{com}, and hence friction force is given by

$$F_{com} = \frac{NE_0}{a} \tag{1.22}$$

where N is the number of atoms within the contact [28].

The periodicities and the lattice spacing's of incommensurate contacts are not perfectly matched, which is shown by the 1D schematic representation given in Figure 1.4.2 (b). In this configuration the overlapping potential corrugations cannot fit well into one another

which results in a reduction in the energy barrier, E_0 , which must be overcome for relative sliding to occur. The force required to overcome the energy barrier in the incommensurate configuration, F_{incom}, is much less than that of the commensurate, $F_{incom} << F_{com}$. Structural or superlubricity was first discovered by Hirano and Shinjo in 1990 by measuring the friction force between two mica sheets as a function of the in plane orientations where higher friction forces were measured along commensurate stacking configurations in comparison to the much lower friction forces of the incommensurate configurations [26-27]. In 2004 Dienwiebel et al performed FFM on graphite/graphite contacts and found large frictional forces in commensurate configurations and vanishingly small friction forces in incommensurate configurations [55]. Similarly structural lubricity has been found on a number of nano particles with lattices which are incommensurate with the underlying substrate [28-29].

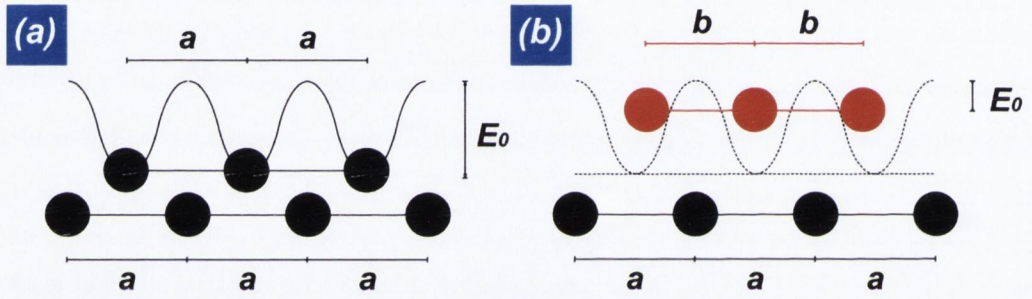

Figure 1.4.2: (a) 1D schematic representation of the sliding of commensurate surfaces in contact, (b) 1D schematic representation of the sliding of incommensurate surfaces.

Once the static friction force has been overcome the sliding motion should continue indefinitely in the absence of any dissipative mechanisms however all sliding interfaces dissipate energy. The dissipated energy may be due to the emission of phonons which are created as the atoms slide over one another [17, 56-57]. Energy can also be dissipated by the creation of electron hole pairs during sliding which is called electronic friction, for example the dramatic reduction in the friction coefficient during the superconducting transition [50]. Wear or interfacial plasticity is another dissipation mechanism which may be due to the formation or breaking of bonds within the sliding interface.

1.5 Nanoindentation

Nanoindentation is a technique used to probe the mechanical properties of small volumes of material by bringing an indentation tip, with well defined geometry, into contact with a test sample and applying a compressive load [58]. Traditional hardness tests such as

Rockwell, Brinell, Vickers and Knoop tests yield one measurement of deformation per applied load however the applied loads and resultant displacements are continuously measured during nanoindentation testing. The versatility of the instrument is due to the large range of apply able loads along with the high sensitivity and accuracy of measuring the applied loads and resultant displacements. For this reason the instrument has been used to investigate the fundamental deformation mechanisms of a wide variety of materials for example the nucleation and propagation of dislocations in brittle crystalline metals or the time dependant elastic and plastic properties of thin polymer films [59-61].

The essential deisgn features of a nanoindentation system are shown in Figure 1.5.1 and described as follows. The sample is coupled in parallel to a spring system that supports a load cell with high dynamic range and fine controllability with 10's nN resolution and peak loads of 10's N. The support springs are specified to be very compliant relative to the expected contact compliance in the direction of indentation so the whole system is under load control where the load applied is highly biased towards the sample. The spring stiffness in other directions is much higher to ensure one dimensional motion. This is achieved generally though use of asymmetric geometries like leaf springs. To reduce other compliance backgrounds, the load frame must have a very high stiffness. In addition to the correct mechanical coupling, nanoindentation systems rely on precise geometric specification and measurement of vertical displacement and contacting indenter tip shape. The latter is realized through the use of precisely machined diamond indenters that have both regular and known shape on a 10 nm scale as well as small propensity for deformation compared to most materials due to their 1 TPa elastic modulus. As no direct characterization of the indentation deformation geometry can be performed during nanoindentation, a predictable tip shape function is critical to the technique. Post-indentation characterization of residual deformation is possible via electron or atomic force microscopy. However this is tedious and less common, and does not reveal deformation strain under load. The instantaneous position of the indenter tip under the applied load is monitored by a high resolution (~0.1 nm), high dynamic range (~ mm's) displacement sensor. These are typically capacitive plate sensors or optical interferometers. The combination of the above features allows load vs. displacement measurements performed by a nanoindenter to characterize elastic and plastic mechanics in sub-micrometer volumes of metals, ceramics and soft matter. With sufficient bandwidth and lock-in amplification in the controller electronics the nanoindenter can also be operated in dynamic mode which approximates a damped simple harmonic oscillator.

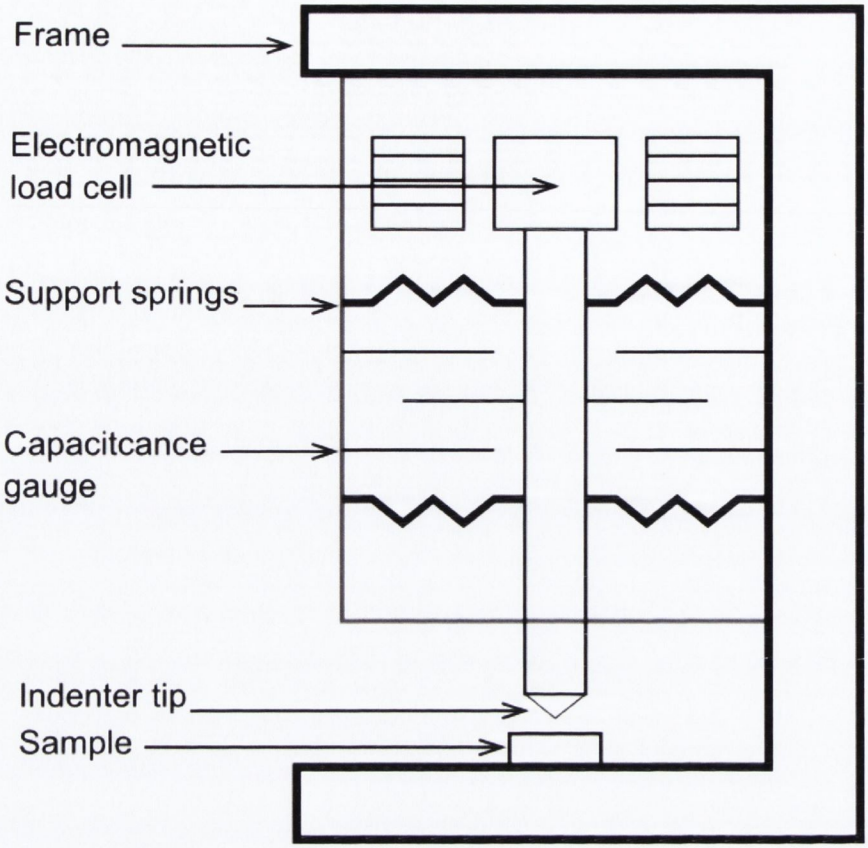

Figure 1.5.1: Schematic representation of the basic elements of a conventional 1D nanoindenter.

The traditional method for measuring the elastic and plastic properties of a material is through quasi-static loading. The test involves incrementally loading the tip while simultaneously measuring the resultant displacement within the sample. The experimental challenge is in the interpretation of the deformation within the sample material from the experimentally available measurements. In 1992 Warren Oliver and George Phar developed a highly successful method for differentiating between the elastic and plastic response during indentation testing which allowed for the successful measurements of Young's modulus and hardness of materials upon which the success of the field of nanoindentation was built [62].

The typical loading and unloading response of a three sided pyramidal Berkovich indentator into fused silica is shown below in Figure 1.5.2 (a). The key features of the loading cycle are illustrated by the schematic in Figure 1.5.2 (b). The initial loading results in elastic and plastic deformation of the initially flat surface up to a maximal load, P_{max}, under which the maximal displacement beneath the tip, δ_{z_max}, is reached. The elastic deformation of the indentation is not localised to within the contact area, instead the

indentation results in the deflection of the surface outside the contact area, δ_{z_s}, which is shown by the schematic in Figure 1.5.2 (b). The response of the material is purely elastic during the initial unloading, since all of the plastic deformation occurs during the loading. The slope of the initial unloading allows the stiffness, S_z , of the contact to be measured and the final depth of the impression, δ_{z_f} , is experimentally obtained by the depth at which the unloading curve cuts the axis.

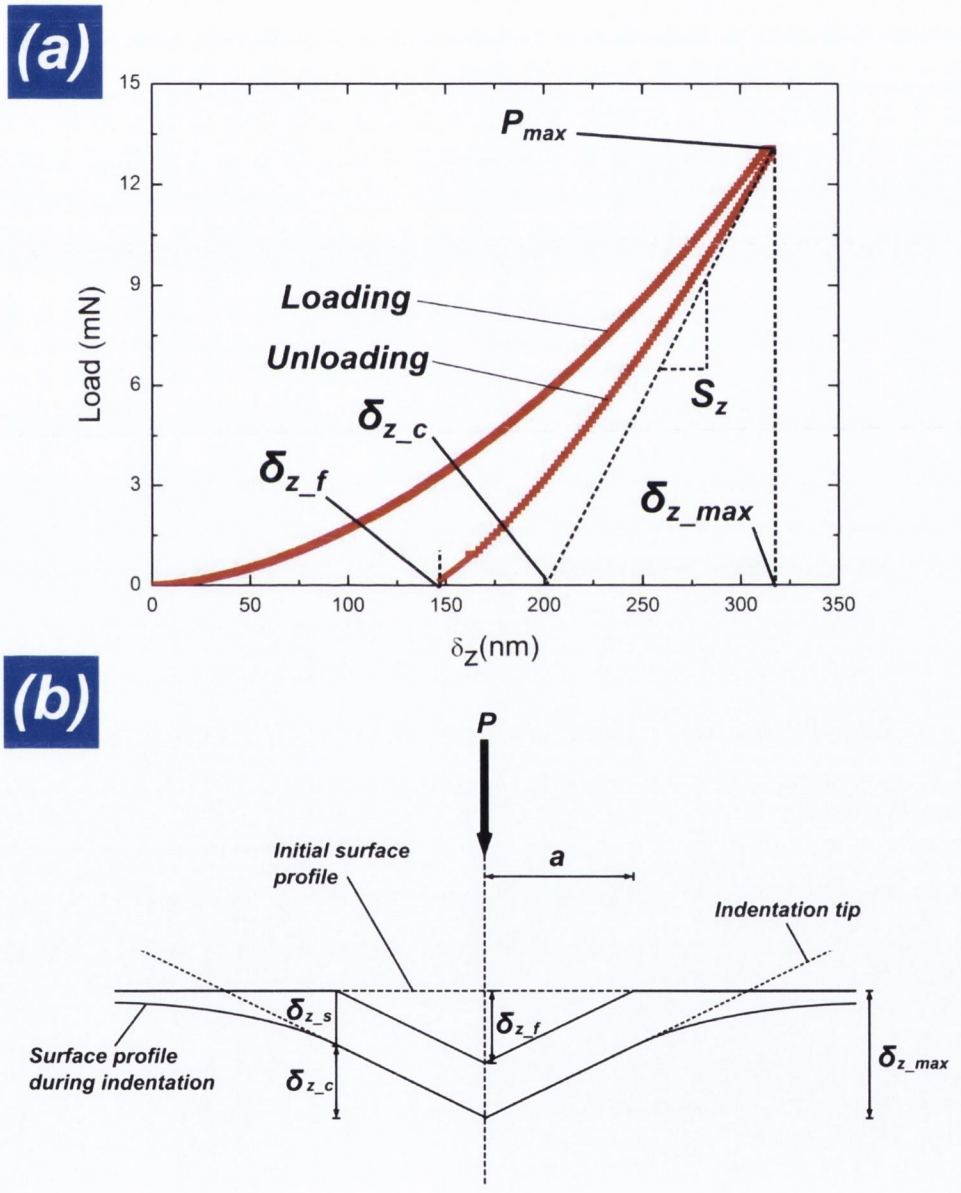

Figure 1.5.2: Schematic representation of quasi static indentation. (a) plot of load vs indentation depth for an indentation into fused silica, (b) schematic representation of the deformation of the indentation.

The contact depth at the maximal load can be obtained by extrapolating the initial unloading curve to the displacement which corresponds to zero load, which is shown in Figure 1.5.2 (a). This extrapolation is only valid in the case of a flat punch where the contact area remains constant during the unloading however any other indentation geometry results in a continual change in the contact area during unloading. In the case of a wedge shape indenter only the maximal and final displacements are experimentally obtainable from the load displacement curve. The real contact depth, δ_{z_c}, is the critical parameter which must be obtained to quantify the elastic and plastic response of the indentation. By considering the indentation it is clear that the maximal displacement is comprised of the contact depth and the surface deflection which is given by

$$\delta_{z\_c} = \delta_{z\_\max} - \delta_{z\_s} \tag{1.23}$$

The deflection of the surface can be obtained from elastic contact theory [63] and is given by

$$\delta_{z\_s} = \frac{\varepsilon P}{S} \tag{1.24}$$

where ε is a constant dependant on the geometry of the contact, which is 1 for a flat punch geometry and 0.72 for a conical wedge shape indenter.

Young's modulus can then be obtained by using the elastic solution of an axis-symmetric, frictionless contact on an elastic half space [64], given by

$$S_z = \frac{dP}{d\delta_z} = \frac{2E^*\sqrt{A_c}}{\sqrt{\pi}} \tag{1.25}$$

For any self similar geometry the contact area can be given as a function of indentation depth given by

$$A_c = f(\delta_{z\_c}) \tag{1.26}$$

The hardness, H, is defined as the mean pressure a material can support [64] which is given by

$$H = \frac{P_{\max}}{A_c} \tag{1.27}$$

The quasi static loading method allows for the elastic and plastic properties to be obtained per full loading and unloading cycle. John Pethica and Warren Oliver developed a method for continuously measuring the stiffness of the contact (CSM) during the loading and unloading cycle which offers significant advantages in being able to determine the elastic and plastic properties as a function of depth. The method involves superimposing a sinusoidal oscillation in the normal compressive load to maintain constant oscillation amplitude in the displacement which is small enough so as not to cause any further plastic deformation. The constant amplitude is achieved by feedback in the lock in amplifier circuit. The continuous stiffness model is based on a 1D damped harmonic oscillator which is represented schematically in Figure 1.5.3.

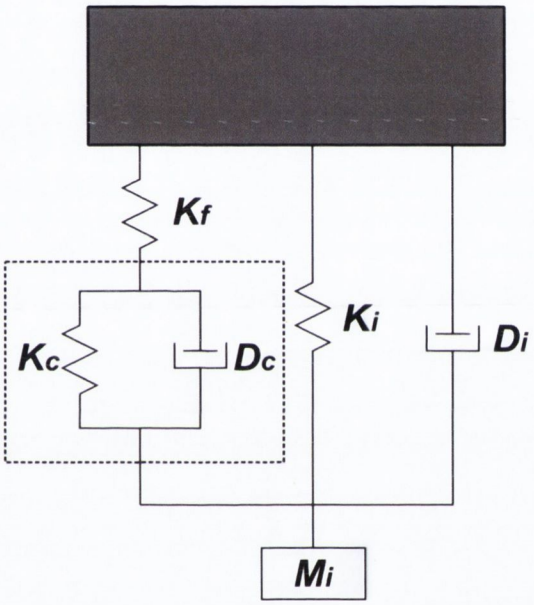

Figure 1.5.3: Schematic representation of a 1D damped harmonic oscillator which is representative of the behaviour of the nanoindenter.

The measured, total stiffness of the system (K_{tot}) is a result of the contact stiffness (K_c) in series with the frame stiffness (K_f) which are both in parallel with the support springs of the nanoindenter (K_i) [58, 65]. The total spring stiffness will be given by

$$K_{tot} = \left[\frac{1}{K_f} + \frac{1}{K_c} \right]^{-1} + K_i \tag{1.28}$$

The contact stiffness will then be given by

$$K_c = \frac{K_f (K_{tot} - K_i)}{K_f - (K_{tot} - K_i)} \tag{1.29}$$

Similarly the total damping of the system (D_{tot}) will be composed of the damping of the indenter components (D_i) and the damping of the contact (D_c) which is given by

$$D_{tot} = D_i + D_c \tag{1.30}$$

The sinusoidal oscillation in the normal load applied by the CSM is represented by

$$P(t) = \mathrm{P}_0 \exp^{(i\omega t)} \tag{1.31}$$

where ω is the frequency of the applied oscillating load P_0 .

The excitation load will result in an oscillating displacement amplitude which has the same frequency but lags the excitation signal a phase angle (ϕ) which is represented by

$$\delta_z(t) = \delta_{z\_0} \exp^{i(\omega t - \phi)} \tag{1.32}$$

Using the simple harmonic equation of motion we can model the response of the system in time by

$$M\ddot{\delta}_z(t) + D\dot{\delta}_z(t) + K\delta_z(t) = P(t) \tag{1.33}$$

where M is the mass of the indenter, D is the damping coefficient and K is the stiffness.

Using equation (1.32) first and second differentials with respect to time are given by

$$\dot{\delta}_z(\mathrm{t}) = \delta_{z\_0} i\omega \exp^{i(\omega t - \phi)} \tag{1.34}$$

and

$$\ddot{\delta}_z(\mathrm{t}) = -\delta_{z\_0} \omega^2 \exp^{i(\omega t - \phi)} \tag{1.35}$$

By substituting equations (1.34), (1.35) and (1.32) into equation (1.33) we obtain

$$-M\delta_{z\_0}\omega^2 \exp^{i(\omega t - \phi)} + Di\delta_{z\_0} \exp^{i(\omega t - \phi)} + K\delta_{z\_0} \exp^{i(\omega t - \phi)} = P_0 \exp^{(i\omega t)} \tag{1.36}$$

We simplify the equation by multiplying each term by

$$\frac{\exp^{(i\phi)}}{\delta_{z\_0}\exp^{(i\omega t)}} \tag{1.37}$$

which yields

$$-M\omega^2 + iD\omega + K = \frac{P_0}{\delta_{z\_0}}\exp^{(i\phi)} \tag{1.38}$$

By separating the real and imaginary parts we obtain

$$K - M\omega^2 = \frac{P_0}{\delta_{z\_0}}\cos(\phi) \tag{1.39}$$

for the real part and

$$D\omega = \frac{P_0}{\delta_{z\_0}}\sin(\phi) \tag{1.40}$$

for the imaginary part.

The phase angle, ϕ, between the excitation in the load and the response in the displacement is given by

$$\tan(\phi) = \frac{D\omega}{K - M\omega^2} \tag{1.41}$$

The small indentation volume underneath the tip contributes to the stiffness of the contact but not the mass. The stiffness of the contact can then be obtained by combining equations (1.39) and (1.29) which is given by

$$K_c = \frac{K_f\left[\frac{P_0}{\delta_{z\_0}}\cos(\phi) - \frac{P_0}{\delta_{z\_0}}\cos(\phi)\Big|_{free\_hanging}\right]}{K_f - \left[\frac{P_0}{\delta_{z\_0}}\cos(\phi) - \frac{P_0}{\delta_{z\_0}}\cos(\phi)\Big|_{free\_hanging}\right]} \tag{1.42}$$

Similarly the damping coefficient of the contact (D_c) can be obtained by subtracting the free hanging damping coefficient of the indenter (D_i) from the measured total value (D_{tot}) given by

$$D_c = D_{tot} - D_i \tag{1.43}$$

The CSM has been proven to be a useful tool for investigating the time dependant elastic behaviour by the frequency specific, phase sensitive harmonic oscillation. The time dependant viscoelastic behaviour of thin polymer films has been recently investigated by Herbert et al via CSM measurements [66].

The Berkovich is a commonly used indentation tip geometry which is shown by Figure 1.4.4. The self similarity of the indentation geometry ensures that the contact area is proportional to the indentation depth squared by a constant of proportionality [62] which is given by

$$A_c = 24.5\delta_z^2 \tag{1.44}$$

In contrast to flat punch, spherical or other blunt geometries the onset of plasticity is instantaneous in Berkovich indentation and the ratio of elastic to plastic deformation within the indentation volume remains constant at all contact depths which is qualitatively different to the behaviour of other non self similar geometries where the initial loading results elastic deformation until a yield stress is surpassed resulting in plastic deformation. Berkovich geometry was used in all the indentation testing reported within this thesis.

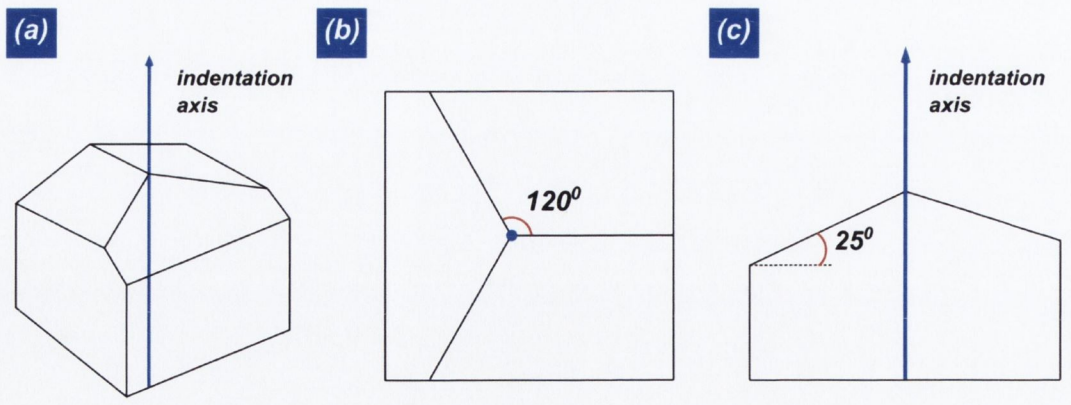

Figure 1.5.4: Schematic representation of the geometry of a Berkovich tip. (a) 3D representation, (b) top down view parallel to the indentation axis and (c) side on view parallel to one of the facets.

Shown below in Figure 1.5.5 is an example of a typical indentation into fused silica using a conventional 1D nanoindenter (DCM) with a Berkovich tip. The loading procedure of the indentation is shown by the plot of the load against time in Figure 1.5.5 (a). The loading segment is an example of constant strain rate loading which exponentially scales the loading rate with indentation depth. Constant strain rate loading is beneficial because the initial loading is very slow which ensures smooth controlled loading of the indenter as well as a high density of data collection in the initial loading segment. The maximal load is held constant for some length of time which should result in no further plasticity in the absence of any time dependent behaviour within the sample material. The load on the sample is then reduced by 90% which is again held constant during which time the thermal drift of the sample is measured and subtracted from the displacement signal throughout the indentation. The resultant load displacement curve is shown by Figure 1.5.5 (b) from which the elastic and plastic deformation of the indentation can be determined. A sinusoidal harmonic oscillation in the normal load is superimposed on the quasi static load and varied to maintain constant amplitude of 1nm during the indentation an example of which is shown below in Figure 1.5.5 (c). The normal stiffness of the contact can be measured throughout the indentation which is shown by the plot in Figure 1.5.5 (d). The linearity of the normal stiffness with indentation depth is predicted by the Sneddon solution since the stiffness is proportional to the square root of the contact area which is linear with indentation depth for Berkovich geometry.

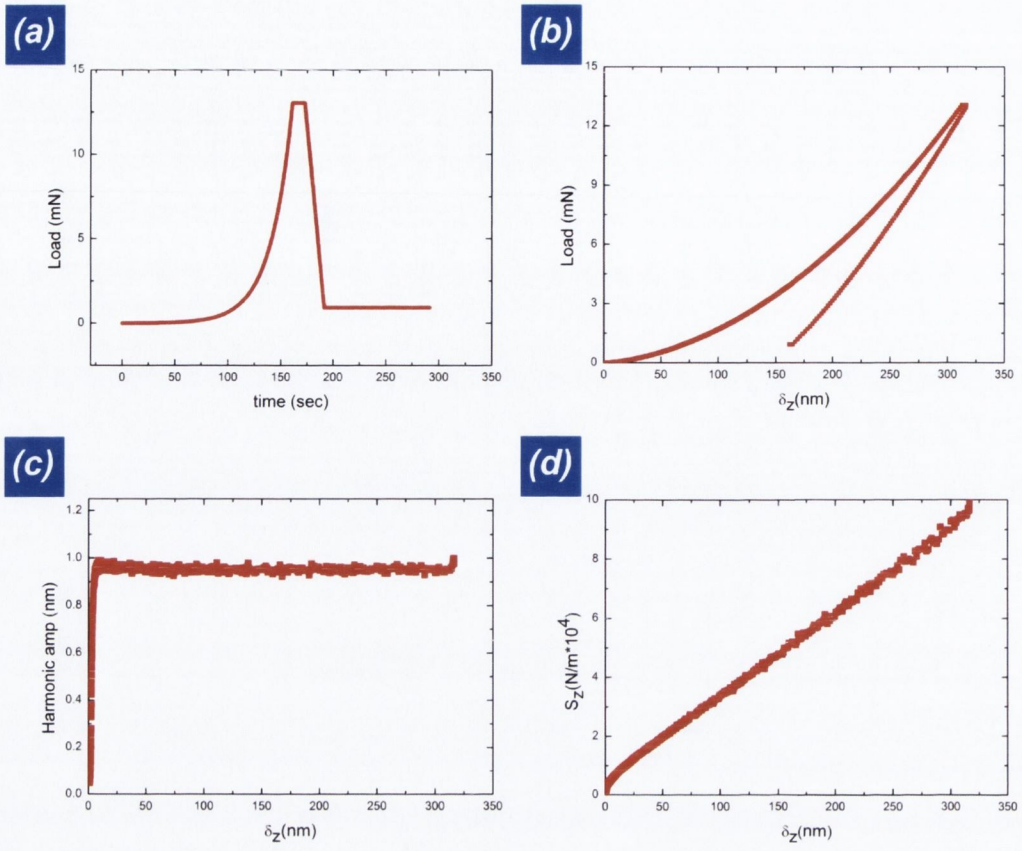

Figure 1.5.5: An example of conventional 1D Berkovich indentation into fused silica. (a) plot of load vs time, (b) plot of load vs displacement, (c) plot of harmonic amplitude vs indentation depth and (d) plot of the normal stiffness vs indentation depth.

1.6 3D Nanoindentation

A custom built multidimensional contact system has recently been developed which enables quantitative force and depth sensing in three dimensions (Fast Forward Devices). The instrument consists of three orthogonal indentation heads which are coupled together by fused silica rods which are approximately 400μm wide and 20mm long, shown by the schematic Figure 1.6.1. This results in a large mismatch between the stiffness parallel and perpendicular to the rod, the values of which are approximately 10^5N/m and 100N/m respectively. The high stiffness parallel to the indentation axis allows force to be transmitted in a controlled manner while the easy bending in the lateral direction act as support springs which is similar to the support springs in the conventional 1D indenter. Each axis can be modelled as a damped simple harmonic oscillator and the stiffness of the contact can be continuously measured in any of the three axes in a similar way to the case of the conventional indenter.

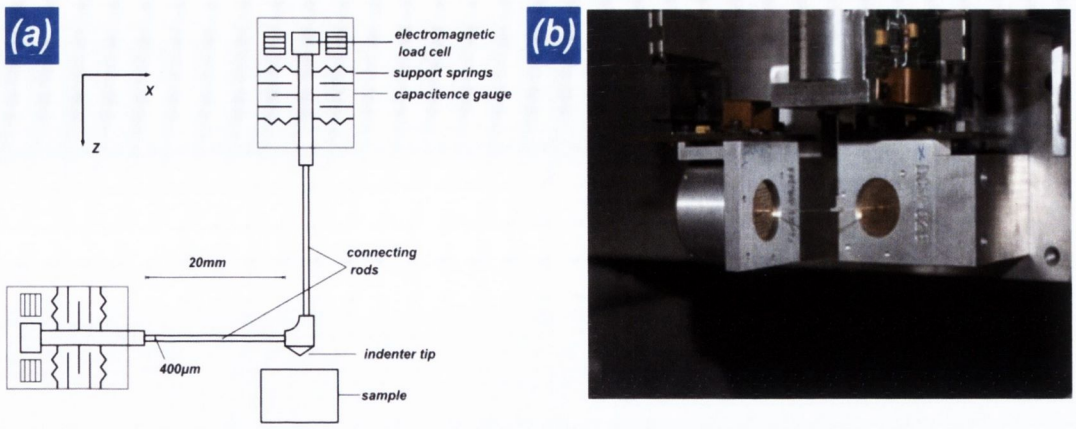

Figure 1.6.1: (a) Schematic representation of the 3D nano contact system showing only two of the three indentation actuators in the X, Z plane and (b) optical image of the 3D nano contact system.

The multidimensional contact system is capable of performing conventional uni-axial indentation testing with continual stiffness measurements allowing the hardness and modulus to be determined however the instrument is also capable of introducing shear stress into the contacts which allows measurements of the tribological properties of materials to be measured for example friction, wear, shear modulus and Poisson's ratio [52, 67-69]. The instrument offers a unique opportunity to study the role of shear stress in nano to meso scale contacts under increasing compressive indentation loading.

Shown below in Figure 1.6.2 is an example of an indentation into a fused silica sample using the 3D contact system with a Berkovich tip and continual stiffness measurements in the normal direction. The quasi static load history of the indentation is shown by the plot of the load against time shown in Figure 1.6.2 (a). The history consists of an initial constant strain rate loading to a maximal load which is held constant until the tip is unloaded to 25% of the maximal value which is again held constant to allow for the determination of the thermal drift after which the final unloading takes place. The resulting load displacement curve is shown in Figure 1.6.2 (c) which is typical of the continuous elastic and plastic deformation during Berkovich indentation. The harmonic oscillations in the normal and tangential directions are shown by the plot of the harmonic amplitudes against indentation depth in Figure 1.6.2 (c). The harmonic amplitudes show the minimal cross talk between each orthogonal axis which provides a good measurement of the stiffness of the contact. The linearity of the normal stiffness with indentation depth is similar to the conventional 1D indentation into fused silica which is predicted by elastic contact theory given by Sneddon.

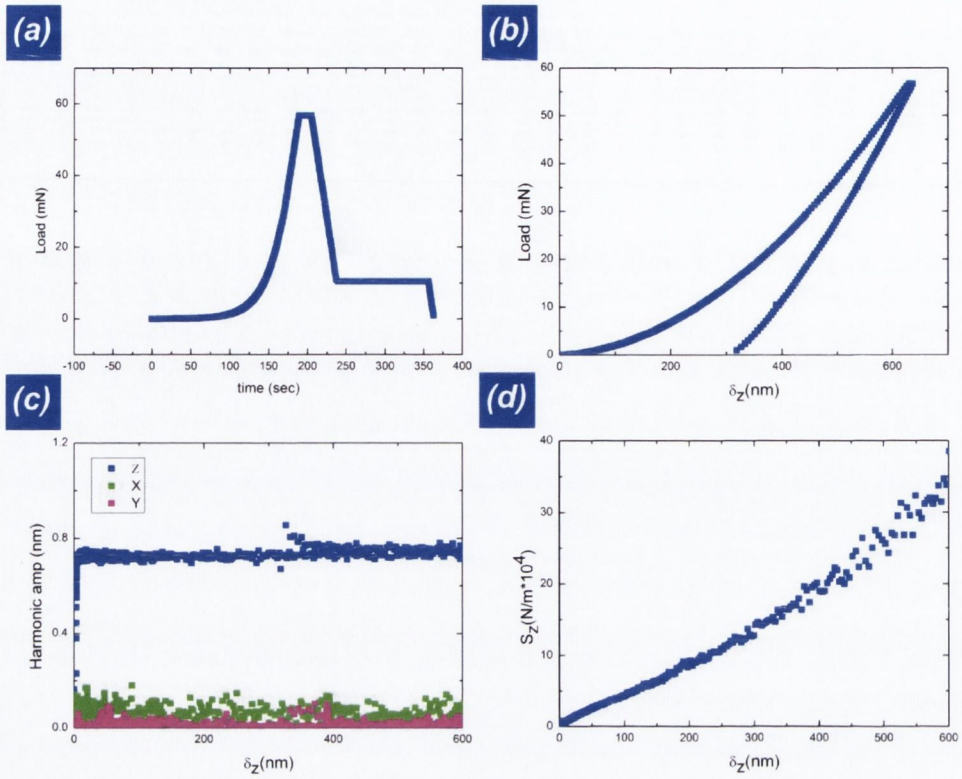

Figure 1.6.2: An example of normal-direction (i.e Z direction normal to the sample plane) CSM signals for indentation into fused silica using the 3D contact system and a Berkovich tip. (a) plot of the load vs time, (b) plot of the load vs indentation depth, (c) plot of the harmonic amplitude vs indentation depth and (d) plot of the lateral stiffness against indentation depth.

An example of an indentation into fused silica with continual stiffness measurement in the lateral direction is shown below in Figure 1.6.3. The loading history and load displacement curve are similar to the previous example however the harmonic load was applied in the tangential direction and the lateral stiffness of the contact was measured as a function of depth which is shown below by Figure 1.6.3 (d). At large depths the lateral stiffness changes linearly with displacement which is predicted by the Mindlin solution however at relatively small depths there is a departure from the elastic behaviour which is due to interfacial slip. The transition from sliding during the initial contact to the elastic solution at large depths can be used to investigate the tribological behaviour of materials.

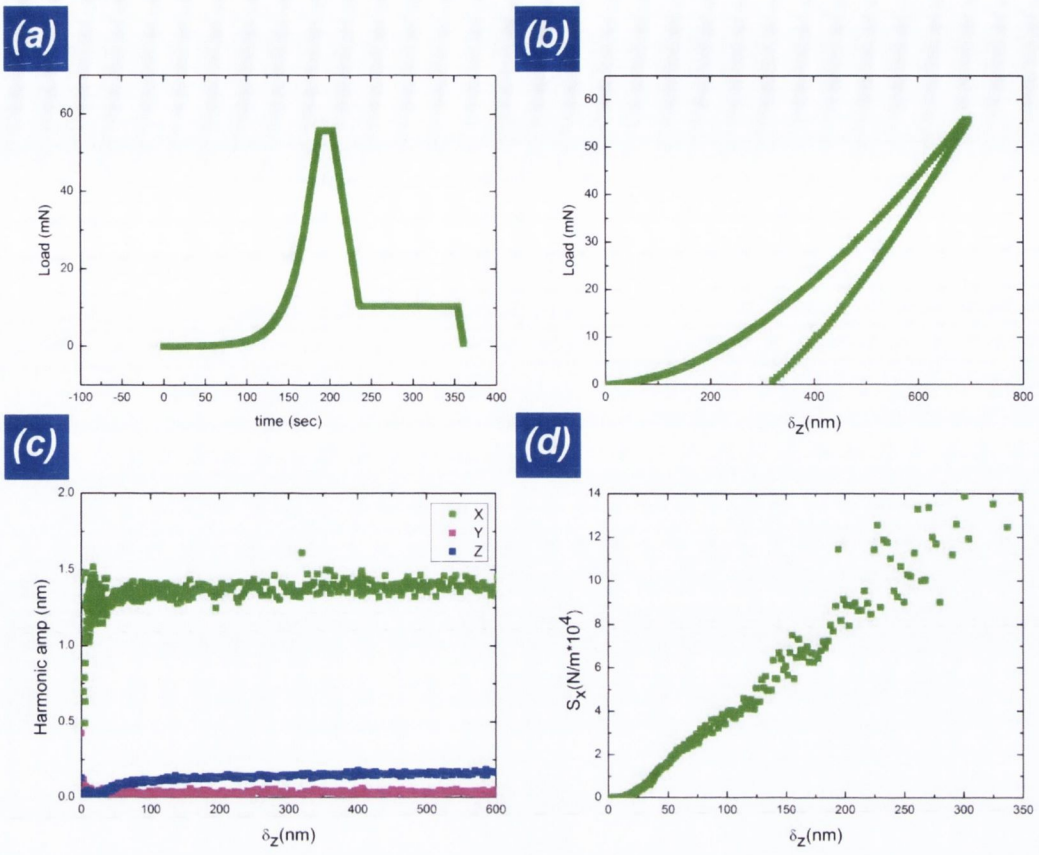

Figure 1.6.3: An example of lateral-direction (i.e X parallel to the sample plane) CSM measuremnet signals of indentation into fused silica using the 3D contact system using a Berkovich tip. (a) plot of the load vs time, (b) plot of the load vs indentation depth, (c) plot of the harmonic amplitude vs indentation depth and (d) plot of the lateral stiffness vs indentation depth.

1.7 Atomic Force Microscopy

Atomic force microscopy (AFM) is a versatile instrument [57] which was initially developed to measure atomic forces between an atomically sharp tip and a sample [18] however today it is more commonly used as a nano to micron scale imaging tool. The AFM tip is fabricated on the end of a cantilever with an appropriate stiffness usually between 40 N/m and 0.1 N/m. The position of the AFM tip is measured by the reflection of a laser from the end of the cantilever onto a photodetector which is shown schematically in Figure 1.7.1. The forces between the tip and the sample are measured by the deflection of the cantilever which can be imposed in two different ways. The first way is called contact mode where the sample is brought towards the tip until a predetermined deflection is registered which results in a force between the tip and the sample. The tip is then successively scanned across the surface of the sample and a map of the topography of the

surface is built. Contact mode can also be used to measure the lateral deflection of the cantilever as the tip is scanned across the surface which is the basis of friction force microscopy (FFM) [70].

The second and most common imaging method is called tapping mode AFM which operates by oscillating the AFM cantilever, near its resonant frequency in free air, with a fixed amplitude. The excitation is imposed by a piezo electric cell and the resultant amplitude of the tip is measured by the photo detector. The sample is then brought towards the tip until the amplitude of the oscillation has decreased by a predetermined amount, referred to as the set point. The tip is then scanned across the surface of the sample while feedback sensing adjusts the average position of the tip so as to maintain a constant set point. The topography of the surface of the sample is then built from successive line scans.

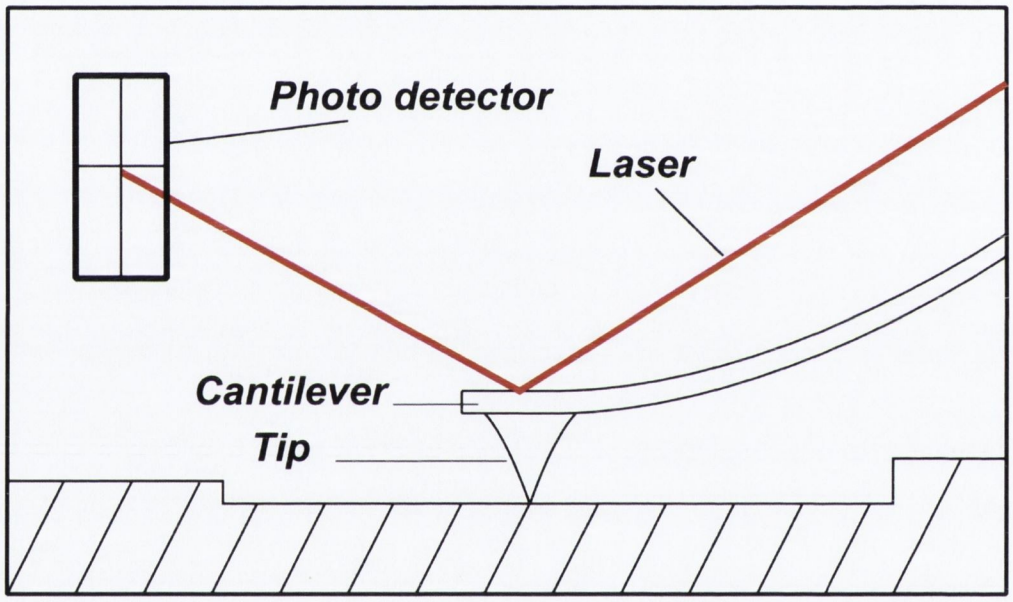

Figure 1.7.1: Schematic representation of the operation of an atomic force microscope.

1.8 Raman spectroscopy

Raman spectroscopy is a non destructive, efficient and accurate technique for probing the bonding structure of materials. It operates by detecting in-elastically scattered photons, which are specific to Raman active process' within the target sample. The high frequency electric field of the incident photon perturbs the energy of the electrons within the sample by an amount, $h\omega_i / 2\pi$, equal to the energy of the photon. In general the excited state will return to the original energy level emitting a photon with equal energy, $h\omega_e / 2\pi$. Rayleigh or elastic scattering occurs when the incident and emitted photon are of equal energy. Raman scattering occurs when the excited state either looses or gains energy due to the interaction with a phonon which results in either a decrease or an increase in the energy of the emitted photon which is called Stokes or Antistokes scattering respectively. Raman spectra are typically complex due to the large variety of Raman active processes and the relative scattering probabilities within the material however the Raman spectra of graphene is remarkably simple consisting of 3 main peaks [71-72]. The first of which is the G peak which results in a Raman shift of around 1580 cm^{-1}. The second predominant peak is the 2D peak which results in a Raman shift of around 2660 cm^{-1}. The third peak called the D peak, with a Raman shift of approximately 1350 cm^{-1}, occurs only in the presence of defects or dopants within the graphene lattice. In recent years Raman spectroscopy has been used to investigate the properties of graphene such as doping [73], edge states [74], defect concentration, chemical functionalisation, strain [75] and interlayer interactions [76-77]. The WiTec alpha 300R Raman spectrometer was used to quantitatively determine the thickness and quality of the mechanically exfoliated flakes which were produced during the course of the experiments. The Raman spectrometer consists of a 523 nm laser with a power output of 30mW and the spectra can be spatially resolved with a resolution of 200 nm from which a spatial map of the Raman spectra can be built. For the purpose of the analysis within this thesis we focus only on the Stokes process's in the Raman spectroscopy of graphene to quantitatively determine the thickness and stacking order of graphene flakes.

The G peak occurs by scattering from in plane traverse optical vibrations shown by the schematic in Figure 1.8.1 (a), which is present in all sp^2 carbon allotropes. The 2D peak is a double resonant process which involves the creation of an electron hole pair by an incident photon the excited electron then undergoes scattering by a phonon with momentum q, which corresponds to in plane breathing mode vibrations. The electron then gets backscattered by another phonon of momentum –q into a virtual state where the electron recombines with the hole emitting a photon with a Raman shift of approximately

2660cm^{-1}, which is shown by the schematic in Figure 1.8.1 (e). The 2D peak of single layer graphene results in a symmetrical peak due to the linear, single valence and single conduction bands. The D band occurs by a similar process to the 2D peak which involves the creation of an electron hole pair by an incident photon which undergoes a scattering process which gets elastically back scattered into a virtual state by the presence of a defect. The electron then recombines with the hole emitting a photon with a Raman shift of approximately 1350 cm^{-1}. The D band can only occur in the presence of defects which break the planarity of the sp^2 bonds in the graphene lattice. The intensity of the D band can be used to determine the concentration of defects in graphene.

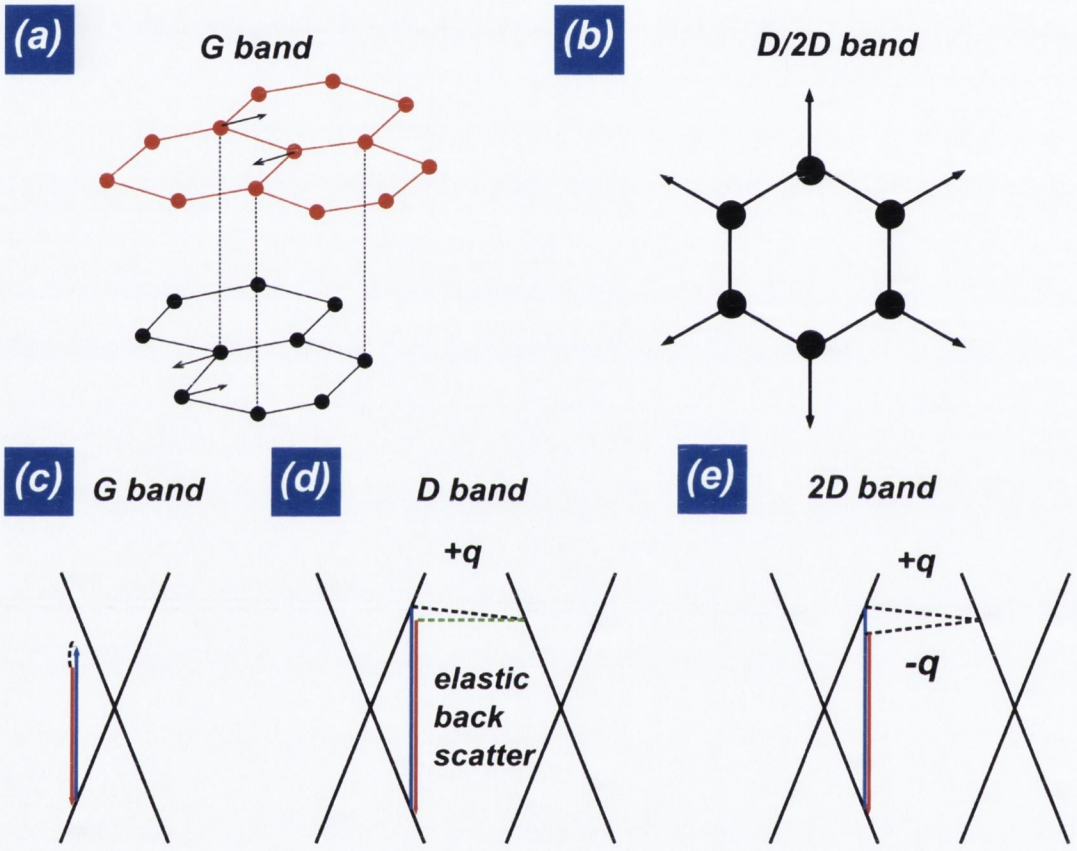

Figure 1.8.1: Schematic representations of the G, D and 2D Raman process's. (a) G band vibration mode, (b) D and 2D vibration mode, (c) G band Raman process, (d) D band Raman process and (e) 2D band Raman process.

The electronic band structure of graphene is comprised of a single π valence band and a single π^* conduction band as shown by the schematic in Figure 1.8.1 (c-e). The 2D peak of single layer graphene results in a single symmetrical Lorentzian peak with a FWHM of approximately 26 cm^{-1} which is due to the single linear π and π^* bands. In AB Bernal stacked bi-layer graphene the interaction between the graphene planes causes the valence and the conduction bands to split into two conduction and two valence bands. This results

in 4 sub peaks within the 2D band which results in significant broadening of the 2D band with a typical value of 52 cm^{-1} for the FWHM of 2D band. Similarly tri-layer graphene results in a further splitting of the electronic bands which results in further broadening of the 2D band. The G band is largely unaffected by the interaction between the layers however an increasing probability of G band scattering occurs with increasing thickness due to the increasing number of C-C bonds within the scanning area. The increase in the 2D band intensity with increasing thickness is less than that of the G band intensity increase since the scattering probability is shared between all the Raman active process's within the 2D band which results in a general decrease of the ratio of the 2D to G band intensities with increasing thickness. However the G and the 2D band intensities are sensitive to environmental conditions such as substrate interactions, charge impurities or doping and the 2D to G intensity ratio is typically used as a qualitative guide to the thickness of graphene flakes [73].

An example of the Raman spectra of single bi and few layer graphene is shown in Figure 1.8.2. The optical image in Figure 1.8.2 (a) demonstrates the increasing optical contrast with increasing thickness. The G band intensity map shown in Figure 1.8.2 (b) demonstrates the increasing G band intensity with increasing thickness however the 2D intensity map shown in Figure 1.8.2 (c) shows a decrease in the 2D intensity with increasing thickness. The map of the FWHM of the 2D band, shown in Figure 2 (d) shows the increase in the broadening of the 2D band with increasing thickness. The symmetry of the 2D peak of a single layer graphene can be seen in Figure 1.8.2 (f) with a FWHM of 26 cm^{-1} and a peak position around 2660 cm^{-1}. The 2D to G band intensities of the single bi and few layer graphene sheets can be seen by the Raman spectra shown in Figure 1.8.2 (e) with approximate values of 2, 0.5 and 0.2. The spectra also show a lack of any significant D band intensity which indicates a low concentration of defects throughout all the graphene sheets.

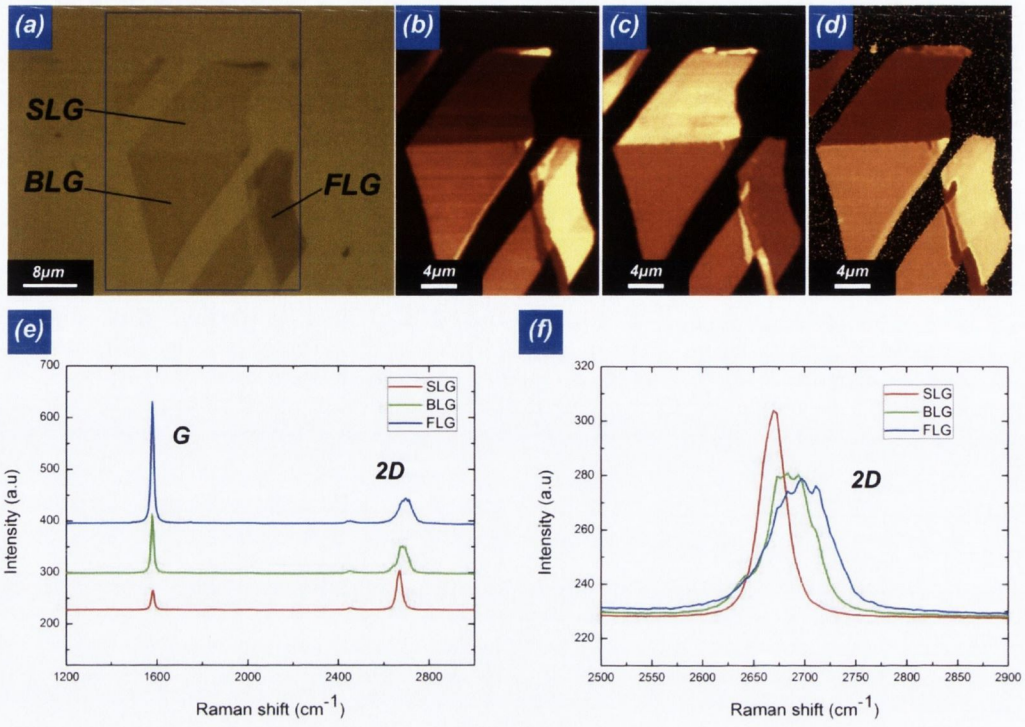

Figure 1.8.2: Raman spectra of single, bi and few layer graphene. (a) optical image of single, bi and few layer graphene, (b) G band intensity map, (c) 2D band intensity map, (d) map of the FWHM of the 2D band, (e) average spectra of the single, bi and few layer graphene and (f) average 2D band of the single, bi and few layer graphene.

Shown below in Figure 1.8.3 is a plot of the measured FWHM of the 2D band for 33 graphene samples of various thickness from which we can see the values fall into 4 ranges which are shown by table 1.8.1. We use the FWHM of the 2D band to quantitatively determine the thickness of the mechanically exfoliated flake used within the experiments. Beyond a thickness of 3 layers the FWHM of the 2D band becomes indistinguishable and we only use the ranges shown in table 1.8.1 to determine the thicknesses of single, bi and tri-layer graphene.

Number of layers	1	2	3	>3
2D FWHM	24-33 cm^{-1}	48-54 cm^{-1}	57-59.5 cm^{-1}	>62 cm^{-1}

Table 1.8.1: Range of the FWHM of the 2D band for the given number of layers.

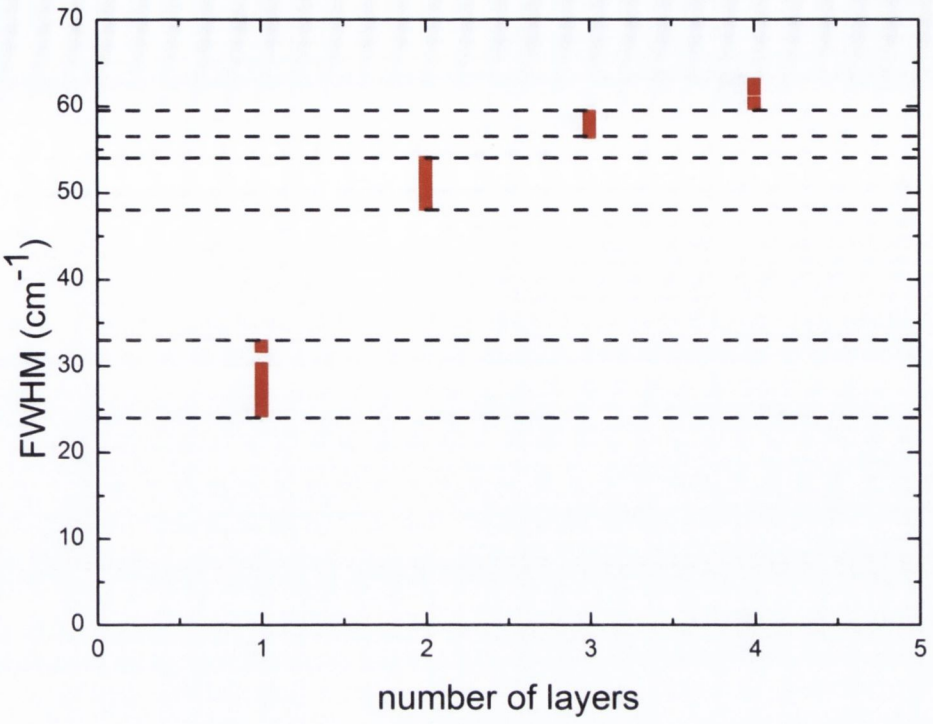

Figure 1.8.3: Measurements of the FWHM of the 2D band for 8 single layer, 16 bi-layer, 4 tri layer and 3 4 layer graphene samples.

Chapter 2: Friction Anisotropy of Single Crystal Ni

2.1 Introduction

The relative sliding of crystalline surfaces in contact has proven to be a scientifically rich area of interest. The interest is due to the many factors which affect the sliding behaviour which include charge transfer [78], lattice structure, orientation , length scale, contacting geometries [49], time, temperature and states of stress [52]. The focus of this chapter is on the elastic and friction anisotropy of a single asperity contact on a high quality single crystal Ni in ambient conditions [68]. A simple schematic of the experimental set up is shown below in Figure 2.1.1, which involves loading a sharp Berkovich tip normal to the surface of the crystal (P, δ_z) while superimposing a small sinusoidal oscillation of 1nm in the lateral direction (T, δ_x) from which the elastic and friction properties of the crystal were measured and by rotating the crystal with respect to the direction of the lateral oscillation the elastic and frictional anisotropy was measured.

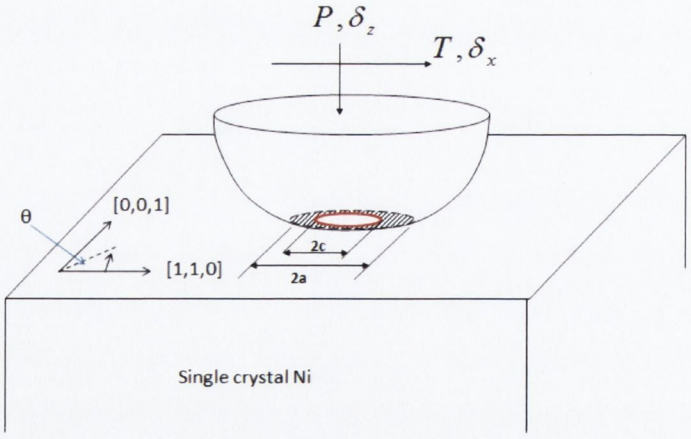

Figure 2.1.1: Schematic representation of the experimental set up.

Previous friction studies performed on contacting nickel surfaces (Ni(100)/Ni(100)), have revealed the friction anisotropy where sliding is preferred in the easy slip direction, even in the presence of layers of adsorbed sulphur and ethanol [79], which stands in good

agreement with the results presented within this chapter. The easy slip direction in our experiments was found to be along the close packed [110] direction which suggests Schmid type behaviour. The sliding in the experiments within this chapter differs from other experiments since the sliding is constrained by a feedback loop which varies the tangential load, T , to produce a constant oscillation amplitude of 1nm peak to peak on contact sizes ranging from 10-1000nm, which is much smaller than the 1cm contacts and macroscopic sliding imposed by Ko et al [79]. Sliding in nanoscale contacts can be facilitated by the nucleation and propagation of dislocations [80] or through the collective behaviour of the interface traversing a potential corrugation which is dependent on the lattice structure [26]. Different lattice structures between the diamond tip and the Ni surface ensures the incommensurability between the surfaces and a continuum of slip is expected between the tip and the sample instead of stick slip behaviour due to atomistic locking.

The nanoindentation involves the conventional quasi-static loading normal to the contacting surfaces which involves elastic and plastic deformation within the indentation volume. The stiffness normal to the surface was measured by introducing a sinusoidal oscillation in the normal load (P) which is varied by a feedback loop to produce a 1nm harmonic amplitude. The resulting stiffness is used with regard to the Sneddon solution [63] which relates the normal stiffness of the contact, S_z , to the contact area, A , and the reduced modulus, E^*, given by

$$S_z = \frac{dP}{d\delta_z} = \frac{2E^*\sqrt{A}}{\sqrt{\pi}} \tag{2.1}$$

where ν is Poissons ratio and the reduced modulus [64] is given by

$$E^* = \left[\frac{(1-\nu^2_{indenter})}{E_{indenter}} + \frac{(1-\nu^2_{sample})}{E_{sample}} \right] \tag{2.2}$$

The application of a tangential load (T) between two surfaces in contact can result in interfacial slip with relative displacement between coincident points within the contact however for a purely elastic contact all points within the contact remain coincident which results in elastic deformation within the indentation volume, shown by the schematic in Figure 2.1.2.

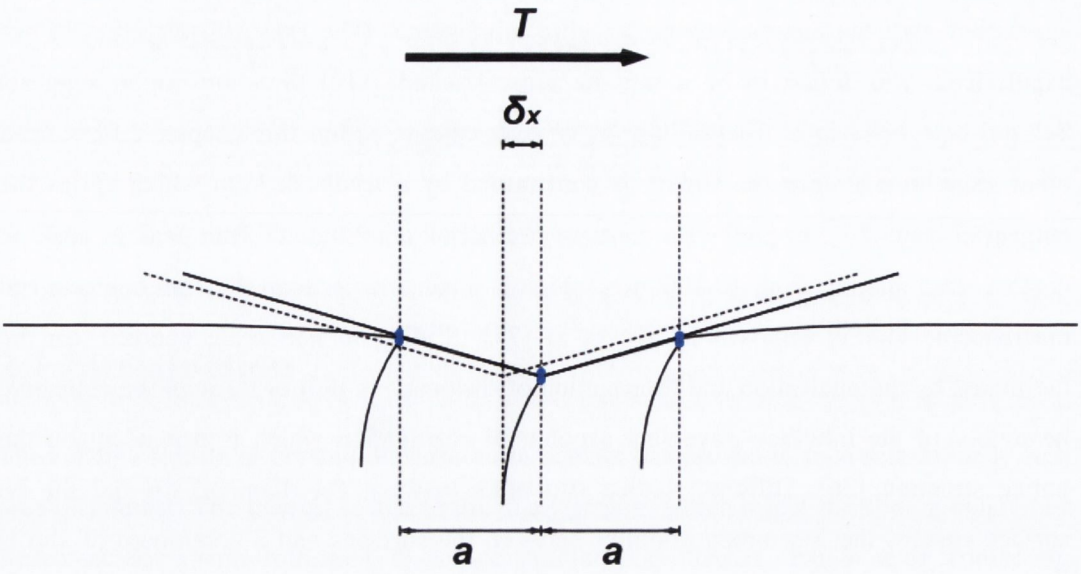

Figure 2.1.2: Schematic representation of the interface of a purely elastic contact with no relative displacement between coincident points within the contact.

The lateral stiffness (S_x) of an axis symmetric elastic contact is given by the Mindlin solution [64], which relates the stiffness to the reduced shear modulus, G^*, and contact area, given by

$$S_x = \frac{dT}{d\delta_x} = \frac{8G^*\sqrt{A}}{\sqrt{\pi}} \tag{2.3}$$

where the reduced shear modulus G^* is given by

$$G^* = \left[\frac{(2-\nu_{indenter})}{G_{indenter}} + \frac{(2-\nu_{sample})}{G_{sample}} \right] \tag{2.4}$$

The self similarity of the Berkovich indenter ensures that the radius of the contact area (a) scales linearly with depth of indentation (δ_z) by a constant of proportionality, β which is given by

$$a = \sqrt{\frac{A}{\pi}} = \beta\delta_z \tag{2.5}$$

The shear modulus can then be determined from the slope of the lateral stiffness with indentation depth, δ_z, which is given by

$$\left.\frac{dS_x}{d\delta_z}\right|_{elastic} = 8\beta G^* \tag{2.6}$$

Similarly Young's modulus will be given by

$$\left.\frac{dS_z}{d\delta_z}\right|_{elastic} = 2\beta E^* \tag{2.7}$$

2.2 Partial Slip model

The interfacial shear stress distribution for a spherical elastic contact is given by

$$\sigma_{xz}^{elastic} = \frac{T}{2\pi a\sqrt{a^2 - r^2}} \tag{2.8}$$

where T is the applied tangential load, a is the radius of the contact area and r is the radial distance from the initial point of contact along the line of centres [64].

The stress distribution has an inverse square root singularity at the periphery of the contact, where $r = a$. This singularity must be regularised by either interfacial slip or plastic deformation. The small amplitude of the lateral oscillation of 1nm appeared to have little effect the gross plasticity during testing which suggests that the lateral oscillations did not produce any significant wear or plastic deformation. Instead the lateral oscillations produced an annular region of slip, which is shown by the schematic in Figure 2.2.1.

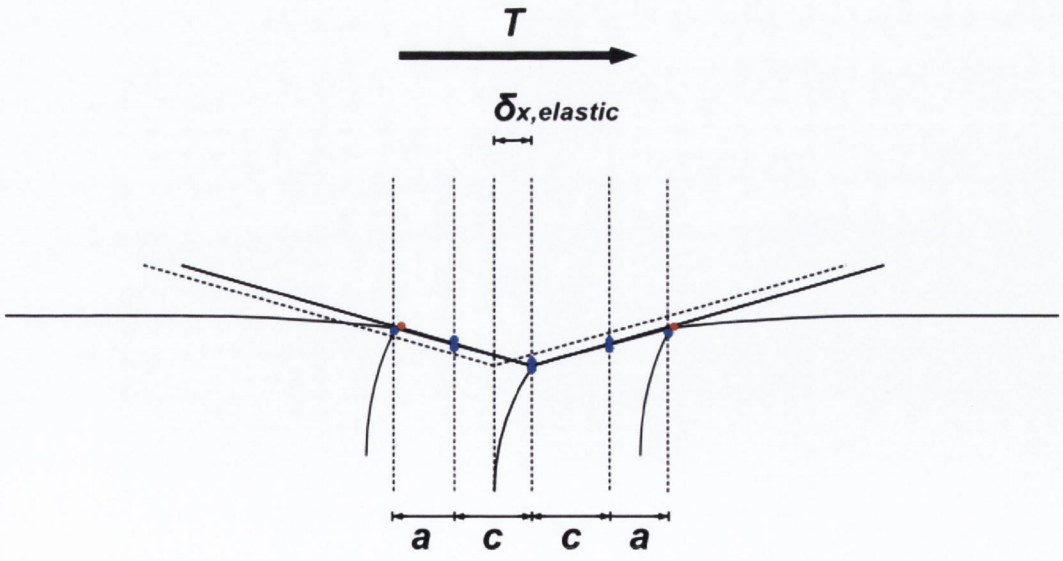

Figure 2.2.1: Schematic representation of the interface with partial slip at the periphery of the contact.

Considering that the interfacial stress at the periphery of the contact is limited by the interfacial shear strength, the shear stress distribution of the contact is modelled with a bi modal equation, derived by Yan Fei Gao and is given by

$$\sigma_{xz}^{slip}(r)=\begin{Bmatrix}\frac{\tau_0}{\pi}\cos^{-1}\left(\frac{2c^2-a^2-r^2}{a^2-r^2}\right), r\le c\\ \tau_0, c\le r\le a\end{Bmatrix} \tag{2.9}$$

where τ_0 is the interfacial shear strength [52, 81].

Within the slip zone (where $c<r<a$) the stress is represented by a single value, τ_0, and within the stick zone, where $r<c$, the stress is represented by a spherically symmetrical function of τ_0 , c and a. The tangential load, T , will then be given by [52]

$$T=\int_0^a \sigma_{xz}^{slip}(r)dr=2\tau_0 a^2\left[\cos^{-1}\left(\frac{c}{a}\right)+\frac{c}{a}\sqrt{1-\left(\frac{c}{a}\right)}\right] \tag{2.10}$$

A plot of the interfacial shear stress distribution against the radial distance for the partial slip solution with normalised shear strength and values of c/a between 0.2 and 0.95 is shown by the solid lines in Figure 2.2.2. The corresponding tangential load, for the given values of c/a, were obtained using equation (2.10) and the elastic interfacial shear stress distribution was plotted against the radial distance which is shown by the broken lines in Figure 2.2.2. At relatively small tangential loads, where $c/a\sim 1$, the elastic solution becomes indistinguishable from the partial slip solution however as the tangential load increases the breakdown of the elastic solution can be seen by the development of the annular slip zone which increases resulting in a large deviation from the elastic solution.

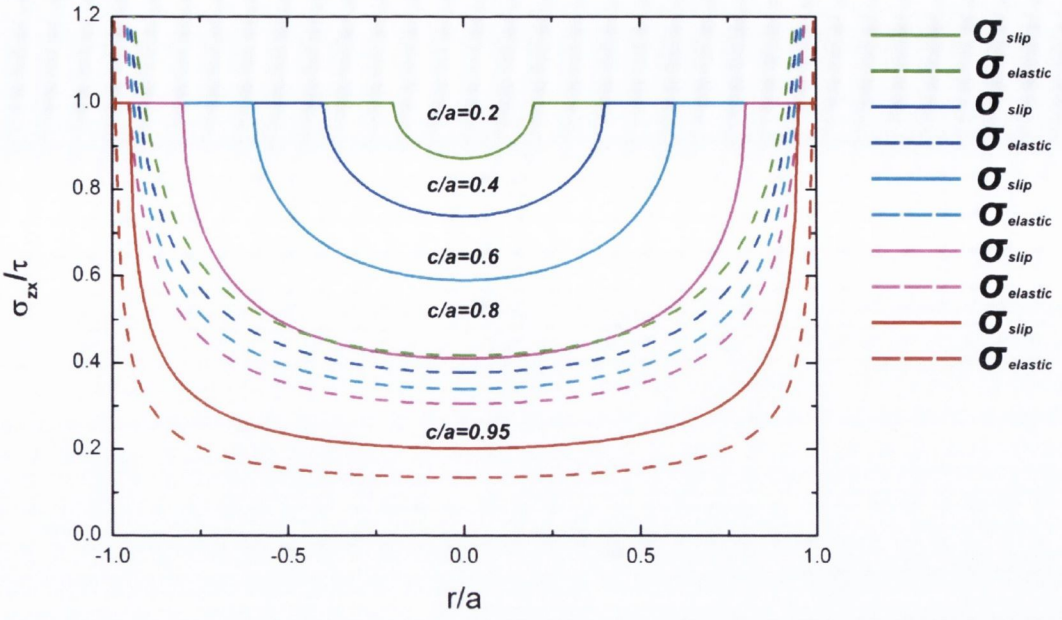

Figure 2.2.2: Plot of the interfacial shear stress distribution with the elastic solution shown by the broken line, with the partial slip solution shown by the solid line.

We define the lateral elastic displacement $\delta_{x,elastic}$ as the relative displacement between distant points perpendicular to the line of centres [64], which is shown by the schematic in Figure 2.2.1 and given by

$$\delta_{x,elastic} = \frac{T}{8cG^*} \tag{2.11}$$

The second distinct displacement is the relative displacement between coincident points within the slip zone, where $c < r < a$ [52, 68], which is given by

$$\delta_{x,slip} = \frac{\tau_0 a}{2G^*}\sqrt{1-\left(\frac{c}{a}\right)^2} \tag{2.12}$$

The maximal lateral displacement is constrained by the oscillation amplitude of 1nm peak to peak however the contact area (a) continues to grow throughout the indentation. Therefore there is an upper bound limit to the contact area which can result in the full slip amplitude which is given by

$$\delta_{\max} = \frac{\tau_0 a_{crt}}{2G^*} \tag{2.13}$$

where a_{crt} is a critical contact area beyond which c/a must be finite and greater than zero.

The elastic deformation within the indentation volume will dominate the measured stiffness in comparison to the stiffness due to the interfacial slip. Therefore the measured lateral stiffness of the contact will be proportional to c/a and by rearranging equation (2.12) c/a can be defined in terms of the lateral slip displacement $(\delta_{x,slip})$, the maximal slip displacement $(\delta_{\max})$, the radius of the contact area (a) and the critical contact area (a_{crt}) which is proportional to the measured stiffness and given by

$$S_x \propto \left(\frac{c}{a}\right) \propto \sqrt{1-\left(\frac{\delta_{x,slip} a_{crt}}{\delta_{\max} a}\right)^2} \tag{2.14}$$

By defining the stiffness at the critical depth, $S_{x,crt}$ by

$$S_{x,crt} = 8 a_{crt} G^* = 8\beta\delta_{z,crt} G^* \tag{2.15}$$

the stiffness of the contact at any depth will be given by

$$S_x = S_{x,crt} \frac{\delta_z}{\delta_{z,crt}} \sqrt{1-\left(\frac{\delta_{x,slip}\delta_{z,crt}}{\delta_{\max}\delta_z}\right)^2} \tag{2.16}$$

This representation of the stiffness allows for a spectrum of values of $\delta_{x,slip}$ between the elastic limit, where $\delta_{x,slip} = 0$, and the full slip condition, where $\delta_{x,slip} = \delta_{\max}$. While the slip displacement remains undetermined throughout the indentation we define an inequality given by

$$\left|\frac{\delta_{\max}\delta_z}{\delta_{x,slip}\delta_{z,crt}}\right| \geq 1 \tag{2.17}$$

which represents the maximum allowable slip displacements due to the experimentally constrained oscillation amplitude of 1nm. Since the elastic deformation of the contact will dominate the measured stiffness an approximation of zero stiffness due to interfacial sliding is used. The stiffness at any depth can be represented by the bimodal equation given by

$$S_x = \left\{ \begin{array}{l} \dfrac{S_{x,crt}\delta_z}{\delta_{z,crt}}\sqrt{1-\left(\dfrac{\delta_{z,crt}\delta_{x,slip}}{\delta_z\delta_{\max}}\right)^2}, \left|\dfrac{\delta_z\delta_{\max}}{\delta_{z,crt}\delta_x}\right| \geq 1 \\ 0, \left|\dfrac{\delta_z\delta_{\max}}{\delta_{z,crt}\delta_{x,slip}}\right| < 1 \end{array} \right\} \tag{2.18}$$

Shown below in Figure 2.2.3 is a plot of the normalised lateral stiffness, as derived from equation (2.18), against the normalised radius of the contact area for the elastic limit, where $\delta_{x,slip} = 0$, and the full slip condition, where $\delta_{x,\text{slip}} = \delta_{\max}$. The elastic solution is identical to the Mindlin solution given by equation (2.3). The measured stiffness of the contact must lie within the two limits throughout the indentation however the stiffness may be fitted by taking the average over the allowable slip displacements which is given by

$$\overline{S_x} = \frac{1}{\delta_{\max}} \int_0^{\delta_{\max}} S_x d\delta_x \tag{2.19}$$

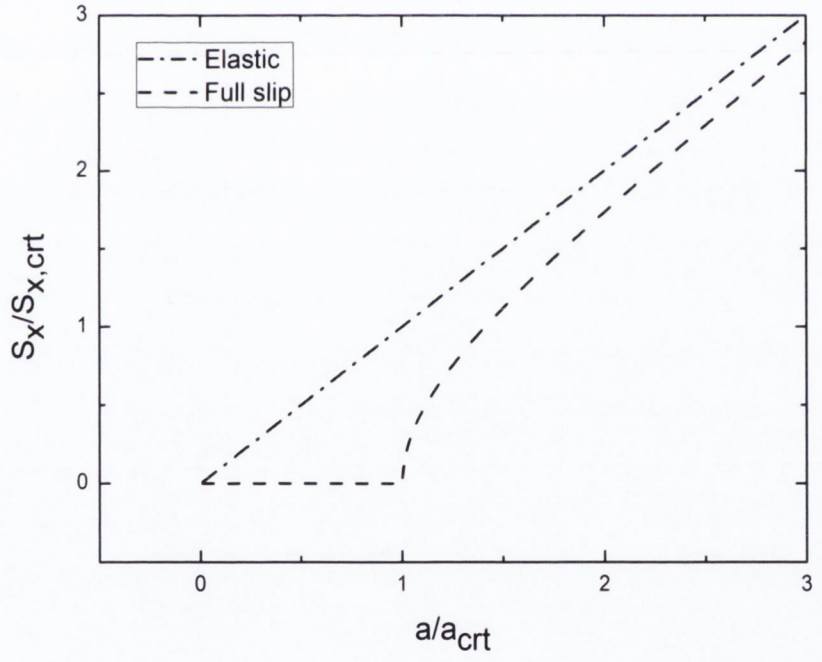

Figure 2.2.3: Plot of the normalised stiffness against the normalised radius of the contact area for the elastic and full slip limit.

The interfacial shear strength is determined by first fitting the linear elastic solution at large depths and then finding the critical depth, $\delta_{z,crt}$. The interfacial shear strength, τ_0, can then be obtained by rearranging equations (2.6) and (2.13) which is given by

$$\tau_0 = \left.\frac{dS_x}{d\delta_z}\right|_{elastic} \frac{\delta_{\max}}{4\beta^2 \delta_{z,crt}} \tag{2.20}$$

2.3 Experimental details

A high quality single crystal of nickel was placed in an ultra high vacuum chamber and LEED was performed to determine the crystallographic orientation. The sample was then removed from the UHV chamber into ambient conditions where it was initially mounted with the [110] direction aligned with the direction of tangential loading, as shown by the schematic in Figure 2.1.1. In order to measure the elastic and frictional anisotropy of the single crystal 11 sets of indentations with 4 indentations per set was performed. The Berkovich tip was brought towards the sample at a rate of 10nm/s until the surface of the sample was registered by a rise in measured stiffness. The tip was then loaded into the sample with a constant loading rate of 2μN/s while a simultaneous oscillation in the load was applied to the tip in the normal direction. This harmonic load, operating at 160 Hz, was varied, via a feedback loop, to maintain a constant harmonic displacement of 1nm allowing for the normal stiffness of the contact to be measured throughout the indentation. The applied normal load was then reduced by 60% and held constant for 60 seconds allowing a thermal drift correction to be determined, after which the tip was fully withdrawn from the sample. Indentation tests were repeated, in different locations, with the lateral CSM in operation allowing for the lateral stiffness of the contact to be measured throughout the indentation. The crystal was rotated through 100 degrees performing indentations every 10 degrees.

2.4 Results and Discussion

The typical quasi static load displacement response for indentations into the Ni [1-10] surface, with oscillations in the normal and lateral directions are shown comparatively in Figure 2.4.1 (a), from which we can see that the small amplitude of the lateral and normal oscillations had little effect on the gross plasticity of the indentation since both the maximal depth at the maximum normal load and the depth of the impression at the final unload are nearly identical. A plot of the normal stiffness against the normal displacement is shown in Figure 2.4.1 (b). The linear change in the normal stiffness with increasing displacement is predicted by the elastic Sneddon solution which indicates the high quality and the self similar geometry of the Berkovich tip. The plot of the lateral stiffness against displacement is shown in Figure 2.4.1 (c) which has two distinct regimes. At relatively large indentation depths, beyond 30nm, the lateral stiffness rises linearly with increasing depth which is predicted by the Mindlin elastic solution, however at relatively small depths there is a relative reduction in the lateral stiffness in comparison to the linear elastic solution. The origin of the reduction in the lateral stiffness is not likely to be due to the geometry of the tip since the normal stiffness portrays the self similar geometry even at low depths and we suggest that the reduced stiffness is due to interfacial microslip.

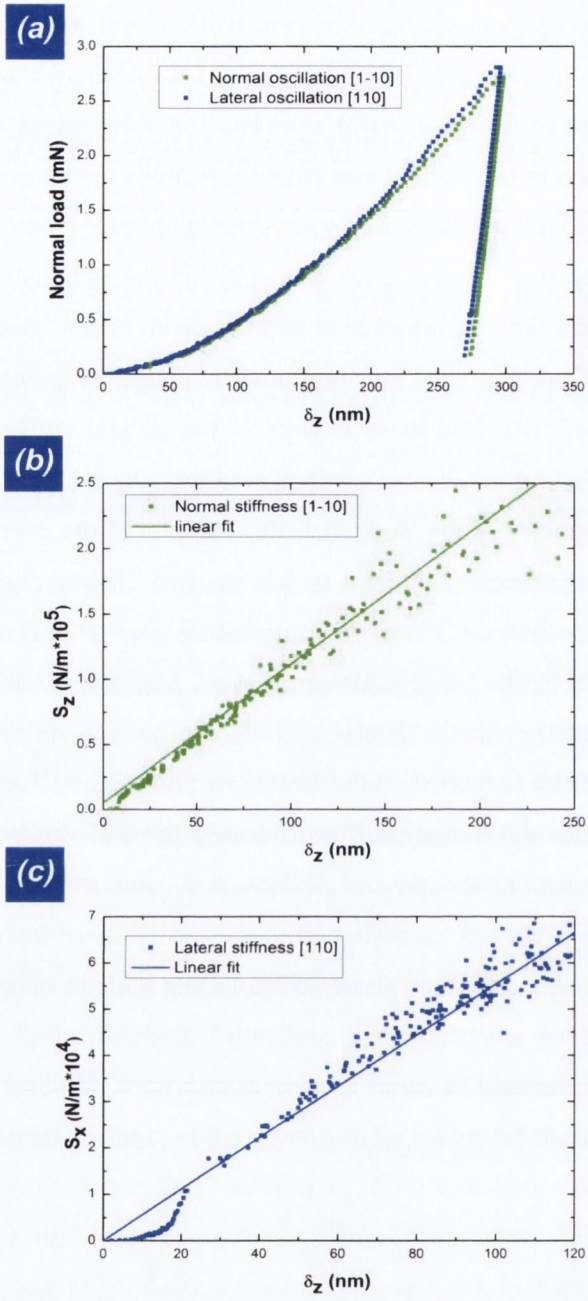

Figure 2.4.1: (a) Comparative plot of the load against displacement for indentations with normal and lateral oscillations in the [1-10] and the [110], (b) plot of the normal stiffness in the [1-10] direction against indentation depth and (c) plot of the lateral stiffness in the [110] direction against indentation depth.

The difference between the frictional and elastic behaviour in the [110], where $\theta = 0^0$, and the [001], where $\theta = 90^0$, directions can be seen by the comparative plot shown in Figure 2.4.2. At relatively large indentation depths the slope of the lateral stiffness is larger in the [001] than the [110] direction. The plot also highlights the difference in the friction behaviour with relatively easy slip occurring in the [110] direction in comparison to the [001] direction. Plotted with the measured stiffness's are the elastic solution (i), the full

slip condition (iii) and the fitted average over the allowable slip displacements (ii) which provides a good fit. The transition from the large scale slip to the elastic solution does not appear to be perfectly smooth. This may be due to discrete plasticity within the indentation volume which may alter the state of interfacial stress between the tip and the sample during indentation.

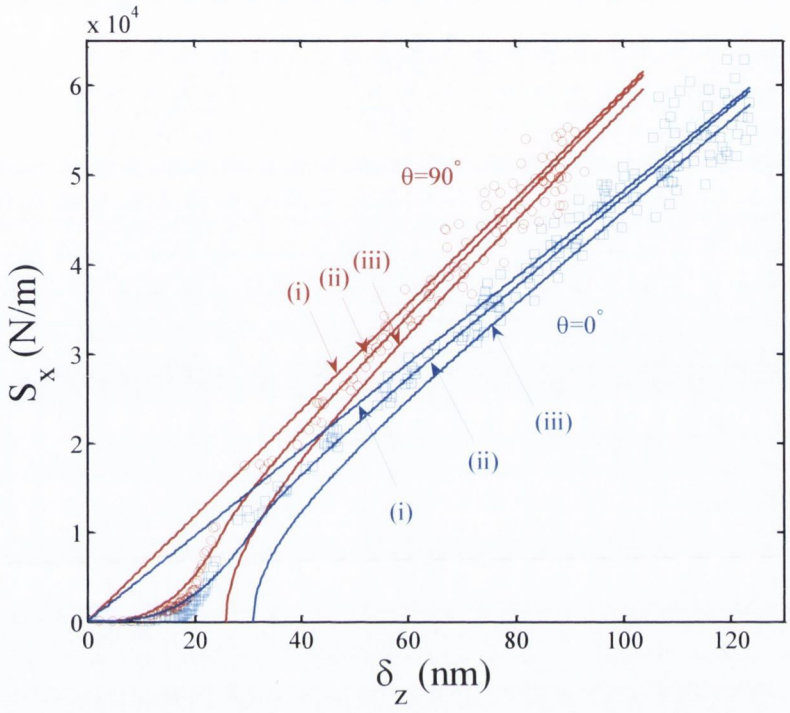

Figure 2.4.2: Comparative plot of lateral stiffness measurements in the [110], shown in blue, and the [001] directions. The elastic solution (i), the full slip solution (iii) and the linear average solution (ii) are also plotted.

Plotted in Figure 2.4.3 (a) are the measured slopes of the lateral stiffness's against orientation angle from which a 20% increase is found as the crystal is rotated from the [110] to the [001]. Plotted in Figure 2.4.3 (b) is the measured interfacial shear strength, τ_0 , against orientation angle and a 40% increase is measured as the crystal is rotated from the [110] to the [001] direction. Scatter is present in both the slopes of the lateral stiffness's and the interfacial shear strengths which may be due to discrete plasticity within the indentation volume.

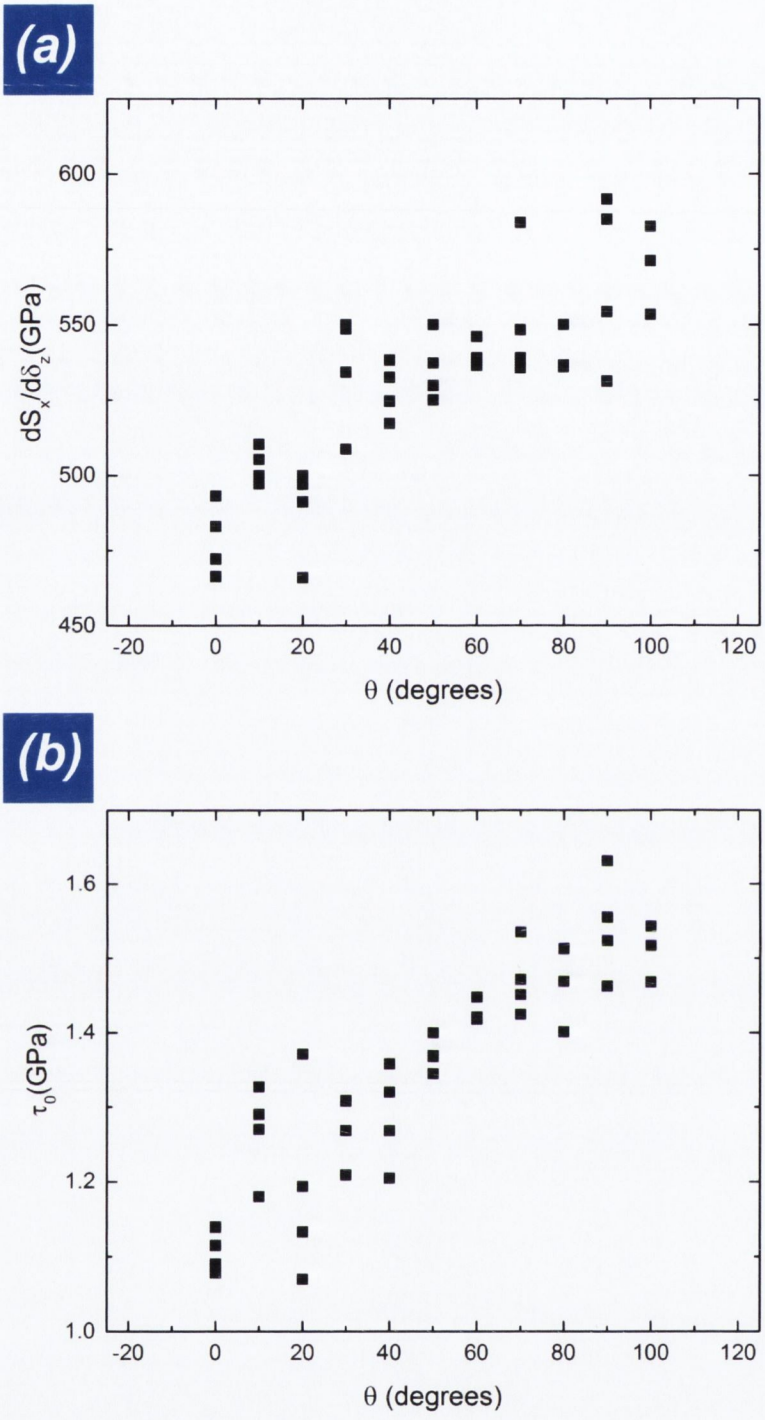

Figure 2.4.3: Summary of the elastic and friction anisotropy form the [110] $(\theta = 0^0)$ to the [001] $(\theta = 90^0)$ directions. (a) plot of the slopes of the lateral stiffness's against θ and (b) plot of the interfacial shear strength against θ .

2.5 Conclusion

The elastic and friction anisotropy of a high quality single crystal Ni has been measured by imposing a sinusoidal oscillation in the lateral direction from which the lateral stiffness was continuously measured throughout the indentation. A 20% increase in the slope of the lateral stiffness against indentation depth was found as the crystal was rotated from the [110] to the [001] direction which is in good agreement with the elastic prediction. An even larger increase of 40% in the measured interfacial shear strength was found as the crystal was rotated from the [110] to the [001] direction. The transition from the large scale slip at the initial contact to the elastic solution at large depths has proven to be a useful means of investigating the tribological properties of nano to meso-scale crystalline contacts in air. The unsmooth transition suggests that the rise in stiffness may be facilitated by discrete plasticity within the indentation volume which may alter the state of stress within the interface. Few experimental studies to date have investigated the transition from a sliding contact to a fully elastic contact on meso-scale. In addition few studies have focused on the effect of the registry between the lattices of contacts made in ambient conditions where adsorbed molecules and contamination are present. The work presented within this chapter clearly shows that the orientation of the lattices of crystalline contacts made in ambient conditions can still affect the friction even in the presence of atmospheric contamination and adsorbed molecules.

Chapter 3: Tribology of Graphene

3.1 Introduction

It has been known for many years that the tribological properties of surfaces in contact can be significantly altered by even a single layer of adsorbed molecules between the contacting surfaces [38, 82]. With the discovery of graphene, in 2004, the friction characteristics of atomically thin sheets have come under scrutiny [9, 83]. Recent tribological studies have shown that quasi 2D materials have excellent friction and wear characteristics making them an ideal candidate for dry lubricants in micro electro mechanical devices (MEMS) and nano electro mechanical devices (NEMS) which require resistance to wear during repetitive contacting under demanding conditions such as high pressure and temperature during the course of their operations [84]. Recently Carpick et al have shown the frictional characteristics of atomically thin sheets using frictional force microscopy [9]. They have shown that the friction force experienced by a sliding contacting AFM tip increases with decreasing number of atomic sheets. They suggest that the sliding AFM tip induces an elastic deformation or puckering advancing in front of the tip which causes an increase in the measured resistance to the sliding. This elastic puckering is suppressed with increasing thickness which explains the increase in the friction force with decreasing number of layers. This friction force dependency on the number of layers has also been found to be substrate dependent which is completely absent when graphene is deposited on atomically flat mica [85]. Other FFM studies by Choi et al have shown that the elastic puckering is dependent on the crystallographic orientation and the puckering decreases with increasing normal load [86]. The tribological properties of graphene have also been shown to be sensitive to surface chemistry where functionalisation of the surface with fluorine and hydrogen has resulted in much larger coefficients of friction during FFM testing [41, 87-88].

A similar layer dependency on the friction properties of graphene has been found during the course the experiments presented within this chapter however the experiments differ from FFM in two significant ways. The first is that the sliding is introduced by a small high frequency (120Hz) harmonic oscillation with displacement amplitudes of between 1 and 2 nm applied continuously in the lateral direction during the indentation. The contact areas during indentation are much larger than the amplitude of the lateral oscillations which is in direct contrast to FFM testing where the contact sizes are typically much smaller than the lateral displacements. The indentation testing results in repetitive cycles at the same location during deformation and through measurements of the lateral stiffness's

of the contacts the tribological properties can be investigated. The second is in relation to the quasi static loading normal to the surface which ensures that the graphene layer is placed under increasing contacting pressures resulting in tension on the graphene layer. The average contacting pressure (σ_z) is equal to the normal load divided by the contact area (A_c) which is given by

$$\sigma_z = \frac{P}{A_c} = \frac{P}{24.5\delta_z^2} \tag{3.1}$$

The dynamics of the contact is governed by two contributions which are distinguishable by the phase sensitive lateral oscillation imposed on the contact. The first is the elastic stiffness of the contact which results from the in phase contributions of the harmonic amplitude. The elastic stiffness, as given by the Mindlin solution, is proportional to the square root of the area of the stick zone (A_{stick}), given by

$$S_{x,crt} = 8cG^* \propto \sqrt{A_{stick}} \propto \delta_z \tag{3.2}$$

Any elastic deformation due to puckering of the 2D sheet at the periphery of the contact is likely to depend on the number of layers and should scale with the perimeter of the contact area and hence scale with indentation depth (δ_z).

The second contribution is due to the out of phase damping coefficient which is the result of energy dissipation within the contact. The interfacial sliding, between the tip and the 2D sheet, results in dissipation of energy as the surfaces slide over one another due to the creation of phonons. Recent FFM experiments by Filleter et al have shown a difference in the friction between single and bi-layer graphene which they attribute to the difference in the electron-phonon coupling between single and bi-layer graphene [89]. MD simulation by Dong et al suggest that the electron-phonon coupling of graphene and surface roughness can contribute to the friction dependence on the number of layers [90]. The lateral stiffness due to interfacial sliding should contribute minimally to the elastic stiffness and should dominate the damping coefficient of the contact. A third contribution may be due to wear or interfacial plasticity. For any crystalline solid wear may not radically alter the interfacial properties however the wear of quasi 2D sheets will result in a loss of lubrication

Recent molecular dynamics (MD) simulations by Fasilino and Wijk have investigated the solid lubrication and wear properties of sliding diamond surfaces under compressive

pressure with single and few layer graphene sheets between contacting diamond surfaces [10]. The simulations suggest that the sliding of the diamond surface over a single layer of graphene results in the destruction of sp^2 bonds, creating amorphous carbon with sp^3 bonding which rapidly results in the destruction of the integrity of the 2D graphene sheet and its lubrication properties. The simulations also suggest that the formation of sp^3 bonds between the layers of few layer graphene is suppressed since it requires the interlayer distance to be within 0.2 nm of one another, which is prohibited by the interlayer repulsion. For this reason they suggest that few layer graphene has superior wear properties in comparison to single layer graphene.

The lateral oscillation imposed during the indentation testing described within this chapter, have produced a variety of unusual folded structures surrounding the residual impression left by the indentation. A detailed discussion of the folded structures is provided in chapter 4 however a series of schematic representations, shown in Figure 3.1.2, suggest a plausible mechanism to explain the fracturing and folding of the 2D membrane observed after indentation. The initial loading results in the deformation of a small volume under the tip which places a tensile stress on the 2D membrane, which is represented by Figure 3.1.2 (a). At some point during the indentation, the 2D membrane ruptures due to a wear process or a critical fracture stress being exceeded. This will result in a relaxation of the strain within the membrane, however no strain relaxation occurs within the substrate, which is set by the conventional normal indentation stress (Figure 3.1.2 (b)). This variation in the strain between the 2D membrane and the substrate may result in a reconfiguration allowing a new equilibrium position to be established. Upon further loading the rupture will propagate outward along the membrane. Once ruptured a new effect may arise within the membrane under the rapid lateral oscillations of the loaded tip. The lateral displacement of the tip will result in a tensile stress on one side of the membrane and a compressive stress on the other side, however the strong in plane bonding and the weak out of plane bending stiffness result in easy bending under compression and high strength under tension, shown in Figure 3.1.2 (c). On subsequent oscillations the membrane may be withdrawn from the interface by discriminating adhesive or friction properties between the membrane, the tip and the substrate surface which is shown schematically by Figure 3.1.2 (c-e). The final impression will result in a bunched or wrinkled structure of the membrane at the periphery of the contact.

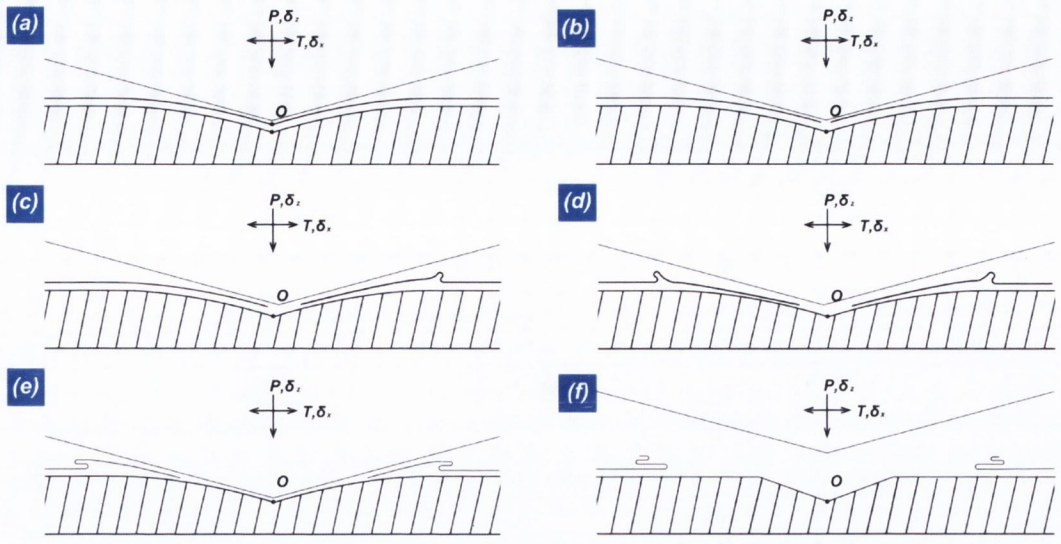

Figure 3.1.1: Suggested mechanism for the deformation of the quasi 2D sheets under the nanoindentation testing with lateral oscillations. (a) The initial loading resulting in tension within the 2D sheet, (b) rupture of the 2D sheet, (c-e) successive oscillations resulting in bunching and the withdrawal of the sheet from the interface and (f) the final residual impression left after the indentation is complete.

3.2 Experimental details

Graphene flakes were exfoliated by mechanical means from Kish graphite (Graphene Supermarket) by the scotch tape method and deposited onto silicon substrates with 300 +/- 5 nm amorphous oxide. The thinnest flakes were then selected for nanoindentation via optical microscopy (Zeis Axio Imager) and the silicon substrates were rigidly mounted within the 3D nanoindenter. Indentation was performed with a constant strain rate to a maximal load of between 0.35 and 10mN. Throughout the indentation a lateral oscillation of between 1nm and 5nm was selected and maintained by feedback sensing. The orientation of the graphene lattice at the point of indentation was unknown, which may vary from point to point within the flake depending on the grain structure of the graphene flake. The relative orientation between the direction of the oscillation and the facets of the triangular Berkovich tip was maintained throughout all the tests. The number of layers of the graphene flakes was determined by Raman spectroscopy (WiTec alpha 300R) and the residual impressions were inspected via tapping mode AFM (Asylum MFP 3D) with standard silicon tips. Similar indentation testing was also preformed on single layer of chemical vapour deposition (CVD) graphene (Graphenea). Hexagonal Boron Nitride (HQ Graphene) was exfoliated by the scotch tape method and deposited on Si substrates with

300 +/-5 nm amorphous oxide and the thinnest flakes were selected for nanoindentaiton. The thickness of the hBN was determined by AFM.

3.3 Results and discussion

3.3.1 Mechanically exfoliated graphene

The typical quasi-static load displacement behaviour of an indentation into a bare SiO_x surface using a Berkovich tip is shown below in Figure 3.3.1 (a). The lack of any pop-ins or discrete bursts indicates that the indentation resulted in continuous elastic and plastic deformation. The plot of the lateral stiffness against displacement is shown in Figure 3.3.1 (b) which is qualitatively similar to the behaviour of single crystal nickel under similar testing described in chapter 2. The relatively low stiffness at low depths is due to interfacial sliding at the periphery of the contact which transitions into a linearly elastic solution at large depths. Plotted in Figure 3.3.1 (c) is the damping coefficient (D_x) against indentation depth. The initial contact resulted in a phase change between the excitation in the tangential load and the resultant harmonic amplitude which is due to the energy dissipation of the interfacial sliding between the tip and the surface of the SiO_x. The damping coefficient continued to increase between depths of 0 and 20nm due to an increasing area of the sliding interface however beyond a depth of 20nm the annular slip zone ceased to increase. The ratio of the damping coefficient to the stiffness of the contact (D_x / S_x) is plotted against indentation depth in Figure 3.3.1 (c). At relatively small depths, below 40 nm, the damping coefficient is relatively large in comparison to the elastic stiffness. As the normal load increases the contact area increases and the slip zone recedes which results in an increase in the stiffness of the elastic contact and a relative decrease in the damping of the contact. Beyond a depth of approximately 40 nm the contact is nearly fully elastic since the ratio of the damping coefficient to the elastic stiffness is effectively zero. This stands in good agreement the plot of the lateral stiffness against indentation depth since the linear elastic regime can be seen above depths of 40nm (Figure 3.3.1 (b)). The residual impression left by the indentation was measured to be approximately 50nm deep from the tapping mode AFM image shown in Figure 3.3.1 (d). The depth of the final unload suggests that the residual depth of the impression is approximately 60nm. This discrepancy may be due to the AFM imaging, for example the AFM tip may not reach the bottom of the impression during scanning or may be due to an error in the calculation of the thermal drift during the indentation.

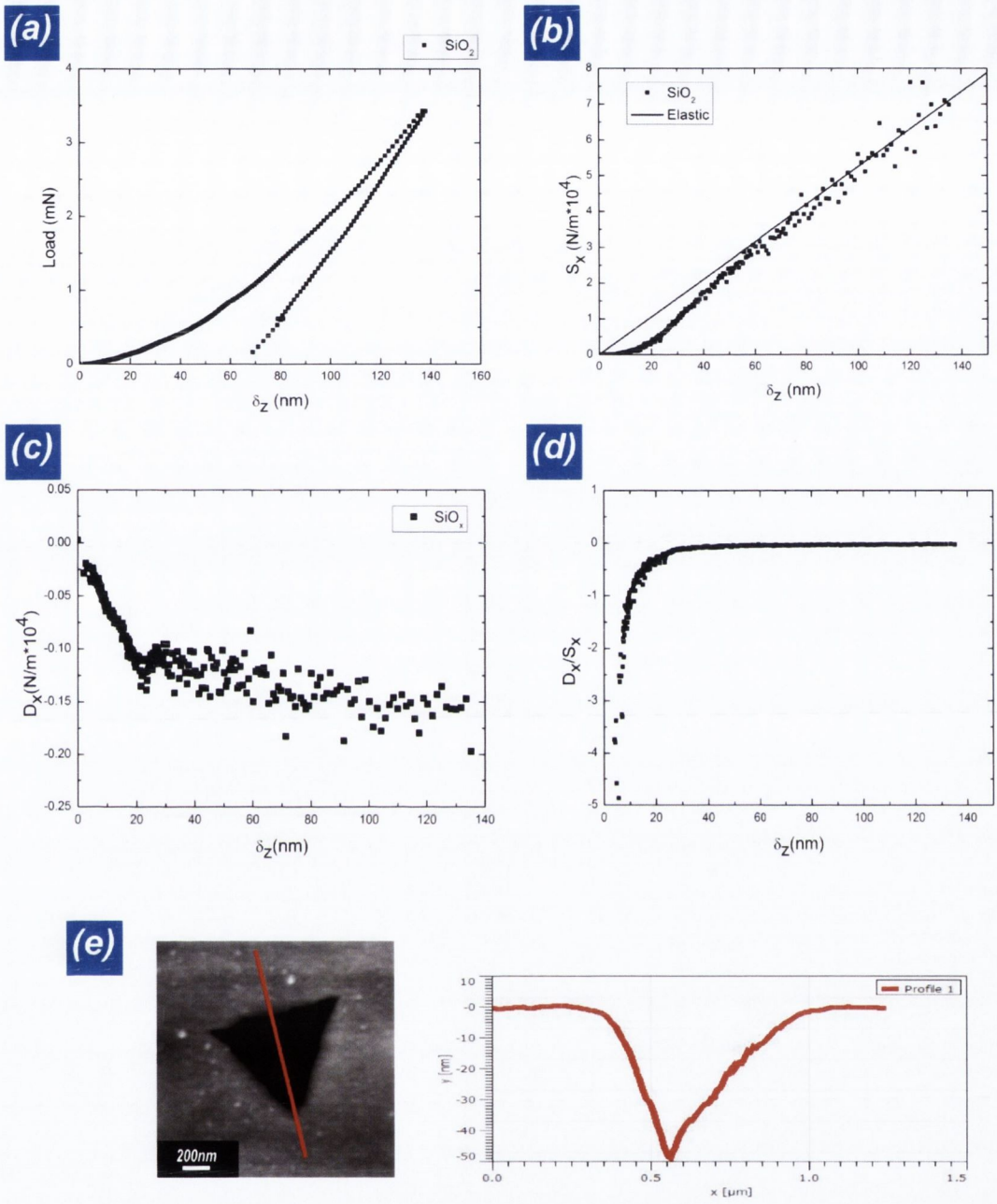

Figure 3.3.1: Example of an indentation into a bare SiO_x surface. (a) plot of the load vs indentation depth, (b) plot of the lateral stiffness vs indentation depth, (c) plot D_x vs depth, (d) plot of (D_x / S_x) vs indentation depth and (e) profile of the tapping mode height AFM image.

The load displacement behaviour of the indentations into the SLG surface is plotted comparatively with the example of the indentation into the bare SiO_x surface in Figure 3.3.2 (a) from which little difference in the gross elastic and plastic deformation between the indentations can be seen. The residual impression left by the indentations into the SLG surfaces is shown by the AFM image shown in Figure 3.3.2 (b) which is similar to the impression left by the indentation into the bare SiO_x surface shown in Figure 3.3.1 (d). Plotted in Figure 3.3.2 (c) and (d) is an example of lateral stiffness measurements as a function of depth for one indentation into an SLG surface, which is qualitatively different to the behaviour of the bare SiO_x surface. At low depths there is an extended region of low stiffness's which continues up to a depth of approximately34nm. The slope of the lateral stiffness is approximately linear from the initial point of contact until a depth of approximately 20nm after which the slope of the lateral stiffness began to increase. At a critical depth of 34nm a large discontinuous jump in the stiffness occurred after which the lateral stiffness became comparable to the stiffness of the bare SiO_x indentation. Beyond this critical depth the slope of the lateral stiffness with depth became linear which is comparable to the elastic regime of the indentation on the bare SiO_x surface. The comparability between the lateral stiffness's of the bare SiO_x and the measurements after the discontinuous jump is interpreted to mean that the graphene had been largely withdrawn from the interface. Plotted in Figure 3.3.2 (e) is the (D_x / S_x) ratio against indentation depth for an indentation into the SLG surface. Similar to the example of the indentation on the bare SiO_x surface there is comparatively large energy dissipation at low depths due to the relative sliding between the tip and the SLG surface however the elastic stiffness of the contact increased relative to the damping coefficient with increasing indentation depth. The elastic nature of the contact beyond the critical rupture depth of 34nm is evident from the measurement of the (D_x / S_x) ratio which is effectively zero. The increase in the (D_x / S_x) ratio between depths of 20 and 34 nm's indicate that the increase in the elastic stiffness between these depths, shown in Figure 3.3.2 (d), is not due to an energy dissipation mechanism. Instead the increase must be due to an increase in the elastic stiffness at higher contacting pressures. The indentation tests performed on the SLG surfaces show regularity in the magnitudes and the slopes of the lateral stiffness's and in the critical indentation depth where the stiffness jump occurred, which is shown in Figure 3.3.2 (f). The excellent lubrication of the SiO_x surfaces by the graphene is evident from the comparative plots of the lateral stiffness's in Figure 3.3.2 (g) and (h).

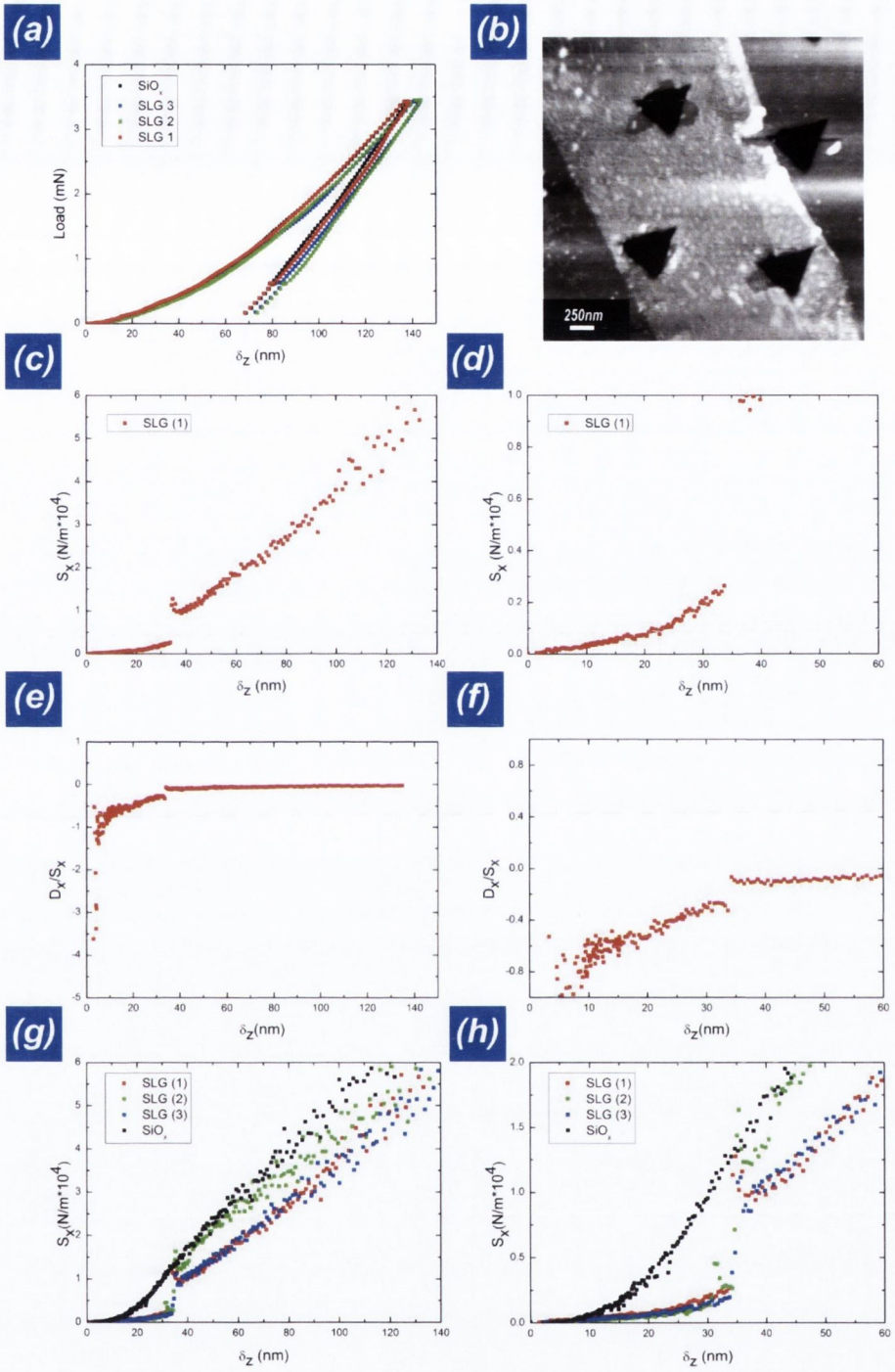

Figure 3.3.2: An example of indentations on an SLG surface. (a) plot of the load vs indentation depth, (b) tapping mode AFM image of the residual impression left by the indentations into the SLG surface, (c) and (d) plots of the lateral stiffness vs indentation depth of one indentation into an SLG surface, (e) and (f) plots of (D_x / S_x) the ratio of the damping coefficient to the lateral contact stiffness vs indentation depth, (g) and (h) comparative plots of the lateral stiffness's vs indentation depths for three indentations on the SLG surface with a single indentation on the bare SiO_x surface.

Shown in Figure 3.3.3 (a) is a plot of the load against displacement of an indentation into a BLG surface, which is similar to the load displacement behaviour of the bare SiO_x and SLG surfaces. The measurements of the lateral stiffness as a function of depth show qualitatively similar behaviour to the indentations on the SLG surface with an extended region of low stiffness from the initial point of contact until a discontinuous jump in the stiffness occurs, which occurred at a depth of 139 nm, shown in Figure 3.3.3 (b). The (D_x / S_x) ratio (Figure 3.3.3 (c)) indicates a relatively large damping coefficient below depths of 30nm. Above 30nm a non zero (D_x / S_x) ratio can be seen which suggests that the elastic and dissipative elements within the contact continued to grow in a self similar manner up to the critical depth of 139nm where the contact transitions into a purely elastic contact and the (D_x / S_x) ratio is effectively zero. The AFM images shown in Figure 3.3.3 (d) and (e) show the similar plastic deformation of the SiO_x substrate however the deformation of the graphene layer is qualitatively different. The AFM images clearly show that the BLG flake was punctured during the indentation and there appears to be no graphene remaining within the impression with wrinkling or bunching of the graphene sheet at the periphery of each of the three facets of the Berkovich impression. On one side of the impression a long thin piece of graphene that was withdrawn from the interface and folded over resulting in two fracture paths along the lattice. The wrinkling and bunching of the graphene at the periphery of the contact is assumed to be due to the cyclic lateral oscillations which have withdrawn the graphene from the interface.

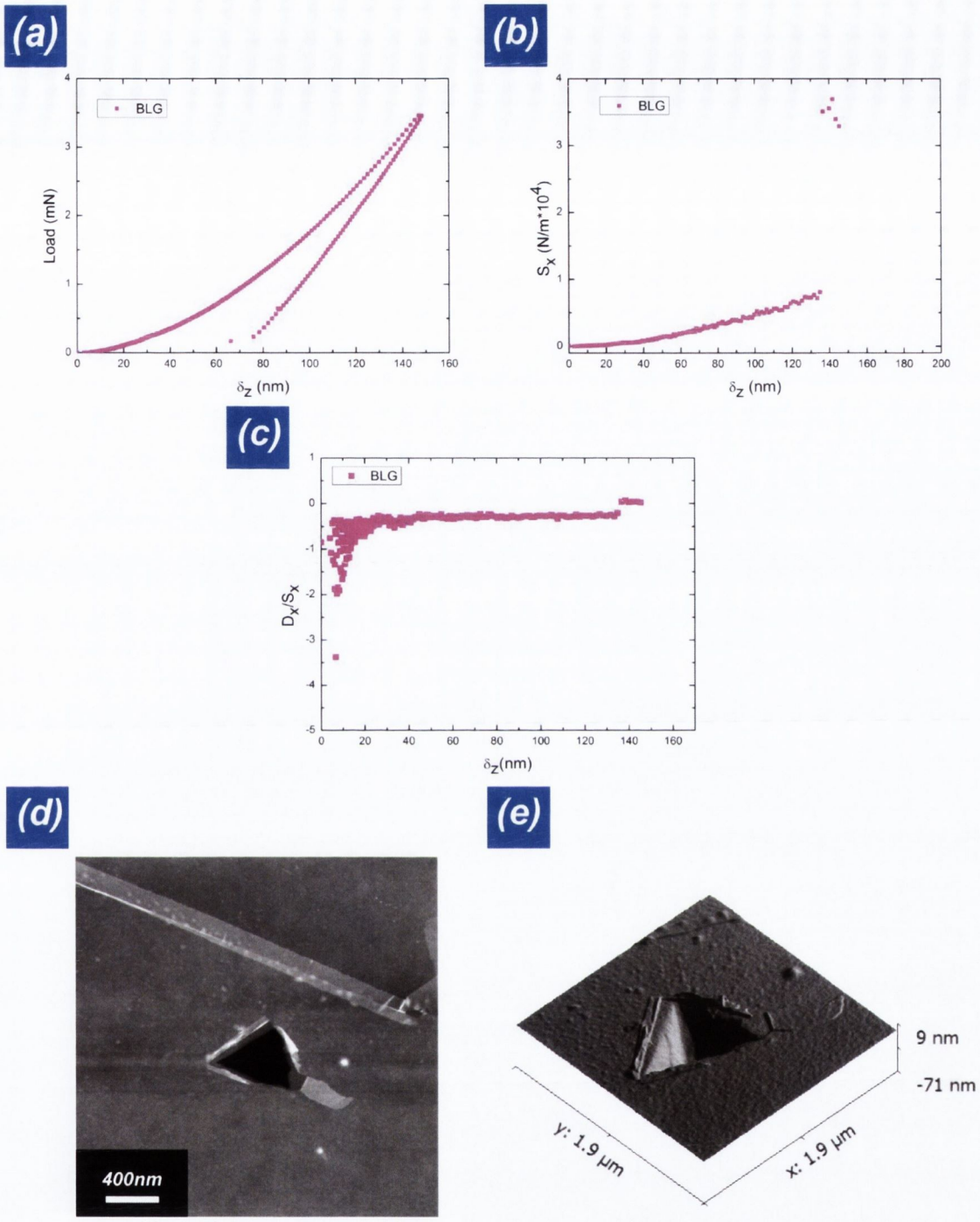

Figure 3.3.3: Example of an indentation into a BLG surface. (a) plot of load vs indentation depth, (b) plot of the Lateral stiffness vs indentation depth, (c) plot of (D_x / S_x) vs indentation depth (d) AFM image of the residual impression of the indentation and (e) 3D representation of the residual impression of the indentation.

An example of an indentation into a TLG surface is shown in Figure 3.3.4. The plot of the load against displacement in Figure 3.3.4 (a) is similar to the behaviour of the bare SiO_x and the other indentations into graphene surfaces with no observable large pop-ins or strain bursts. The lateral stiffness measurements of the TLG indentation was qualitatively similar to the other indentations into the graphene surfaces with relatively low stiffness at low depths followed by the characteristic large discontinuous jump in the stiffness at a critical depth of 165nm which can be seen in Figure 3.3.4 (b). The plot of the (D_x / S_x) ratio is shown below in Figure 3.3.4 (c) which is similar to the indentation into the BLG surface with an extended region of energy dissipation with a finite (D_x / S_x) ratio up to a critical indentation depth of 165nm. The AFM images of the TLG indentation, shown in Figure 3.3.4 (d) and (e), show similar bunching at the periphery of the contact.

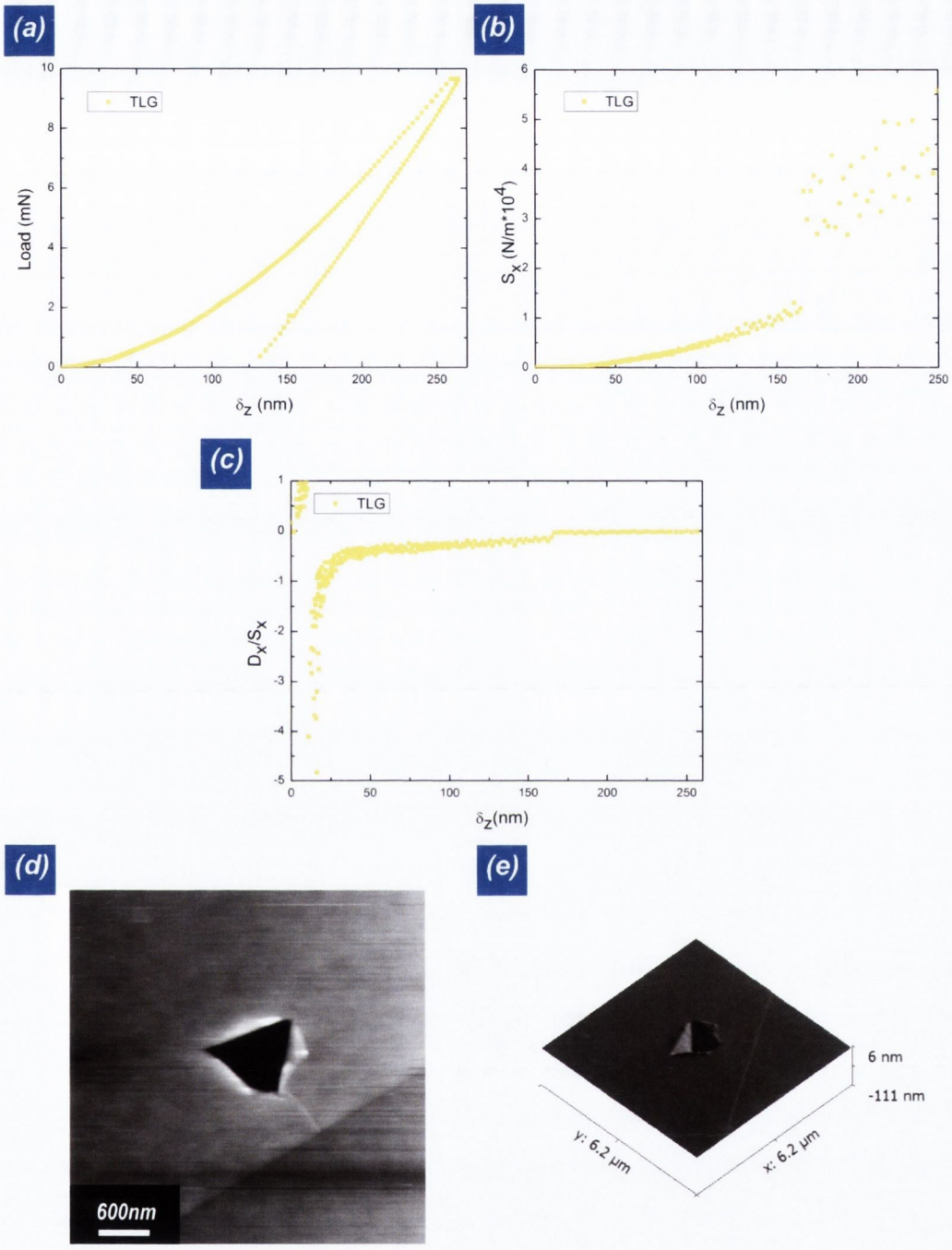

Figure 3.3.4: An example of an indentation into a TLG surface. (a) plot of the load vs indentation depth, (b) plot of the Lateral stiffness vs indentation depth, (c) (D_x / S_x) ratio vs indentation depth, (d) tapping mode AFM image of the residual impression of the indentation and (e) 3D representation of the residual impression of the indentation.

Plotted in Figure 3.3.5 is a comparative plot of the lateral stiffness' against depth for indentations into the bare SiO_x, SLG, BLG and TLG surfaces. The indentations into the

SLG surface resulted in significantly larger lateral stiffness's than the BLG and TLG surfaces. An increased divergence between the slopes of the lateral stiffness's of the SLG and the other FLG surfaces can be seen between depths of 20 and 34 nm's. Considering the similarity of the load displacement curves of all the indentations it is unlikely that the difference in the lateral stiffness's is due to a variation in the contact areas between tests. The measurements of the (D_x / S_x) ratios during the indentation indicate that the divergence between the stiffness's of the SLG and FLG surfaces is due to an increased elastic contribution within the contact. This may be the result of an increase in the Van der Waals interactions within the few layer graphene sheet however the single layer sheet is in direct contact with both the tip and the substrate which may result in increased elastic contributions at higher contacting pressures.

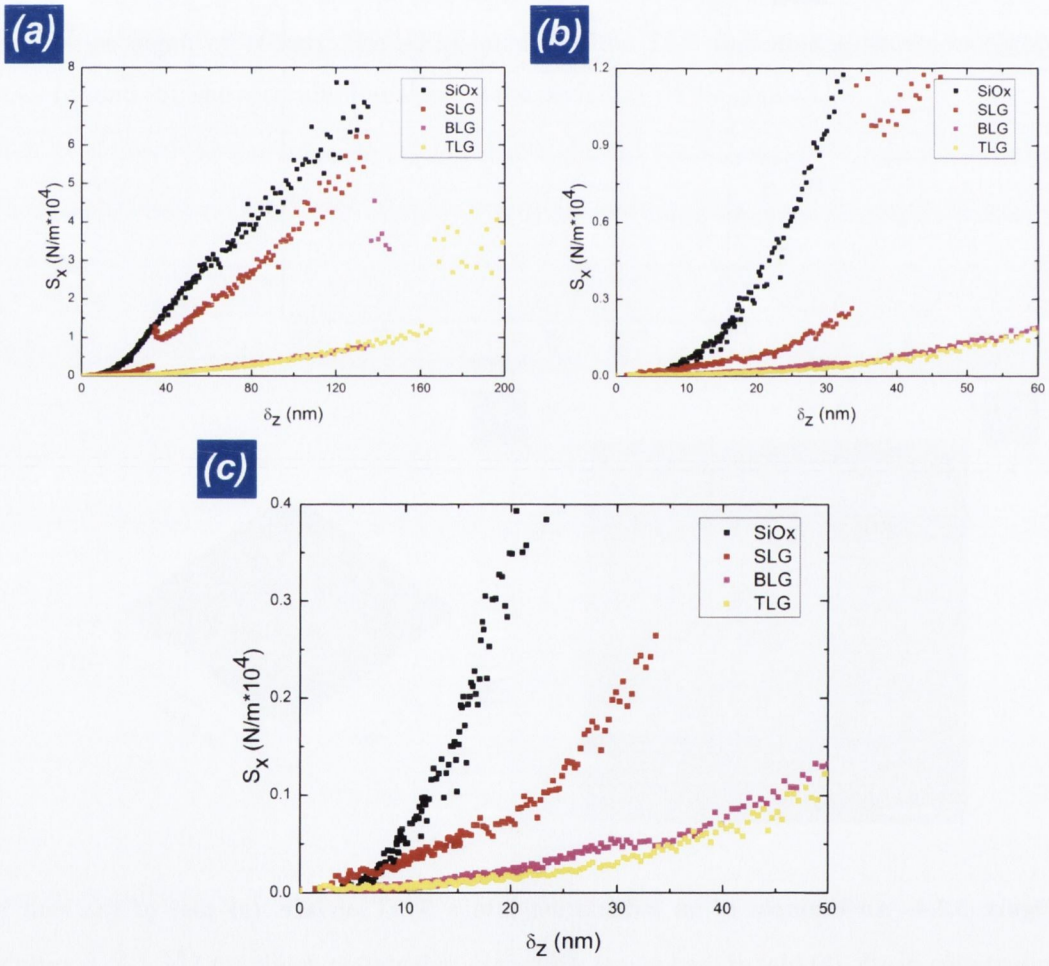

Figure 3.3.5: Comparative plots of the lateral stiffness's against displacement for indentations into SiO_x, SLG, BLG and TLG surfaces. (a) plot of the lateral stiffness vs depth, (b) and (c) zoomed in versions of (a).

Shown below in Figure 3.3.6 is an example of an indentation into a BLG surface to a maximal load of 0.35mN. The plot of the load displacement behaviour, shown in Figure 3.3.6 (a), demonstrates the largely elastic behaviour of the indentation with nearly identical loading and unloading curves and minimal plasticity of a few nanometers. The plot of the lateral stiffness, shown in Figure 3.3.6 (b), demonstrates the lubrication properties of the graphene layer with a lateral stiffness of approximately 600N/m at a depth of 30nm which is approximately 20 times smaller than the lateral stiffness of bare SiO_x at a depth of 30nm. The lateral stiffness of the contact during loading and unloading demonstrates that the lubrication was largely unaffected by the loading cycle which was below the critical rupture threshold. The tapping mode AFM image of the residual impression indicates a lack of any deformation of the graphene layer which supports the suggestion that the discontinuous jump in the stiffness at larger loads is the result of the rupture of the graphene flake.

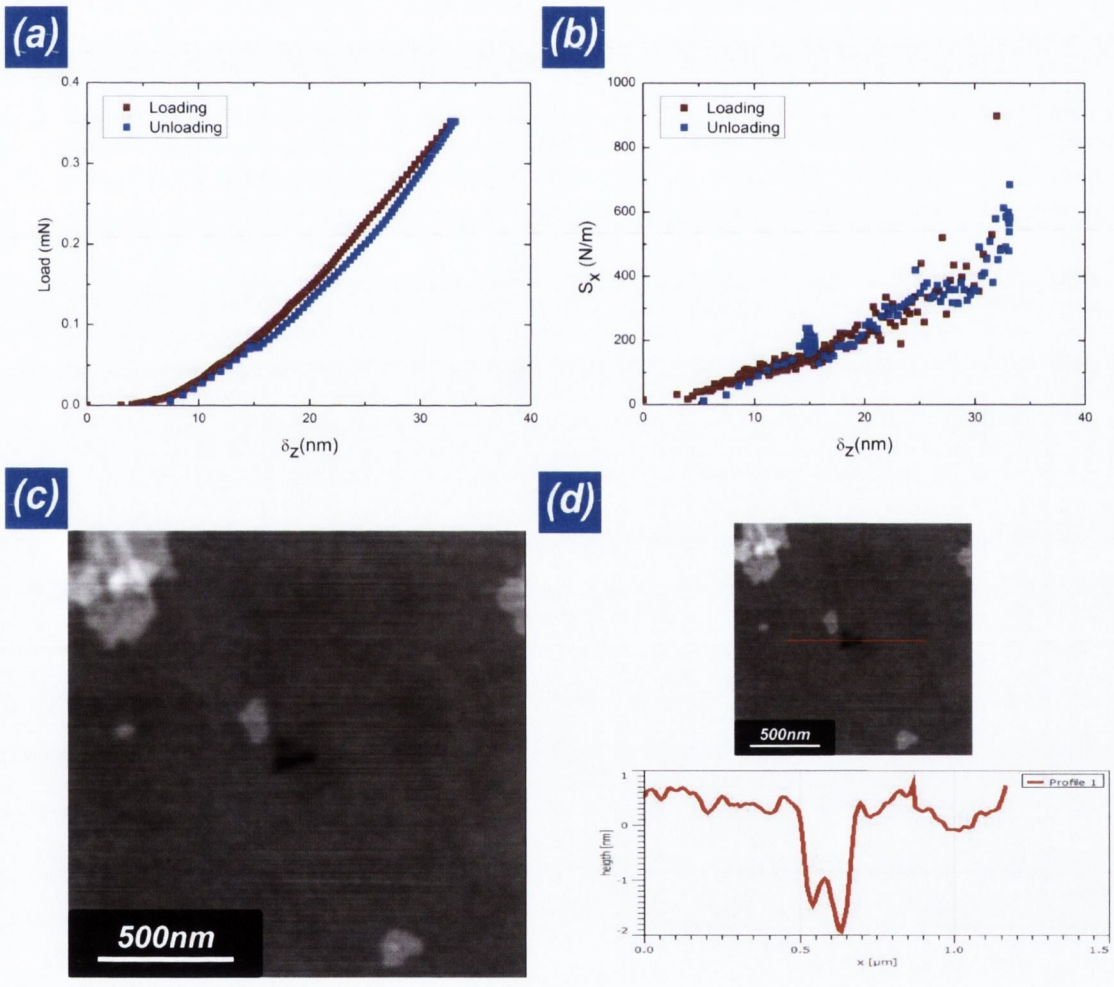

Figure 3.3.6: An example of an indentation into a graphene layer to a maximal load of 0.35mN. (a) plot of the load vs indentation depth, (b) lateral stiffness vs indentation depth, (c) tapping mode AFM image of the residual impression of the indentation and (d) height profile of the residual impression.

A study of 20 indentations performed on 3SLG flakes, 5 BLG flakes and 3 TLG flakes, with a lateral oscillation of 2nm, is summarised by the plots of the critical rupture displacement, the critical rupture load and the critical rupture pressure are shown in Figure 3.3.7 (a-c). The plots illustrate the degree of scatter in the rupture event between tests which may be due to local surface roughness, defects within the graphene, orientation of the graphene lattice or the initial state of stress of the graphene layer during deposition. The data suggests that the rupture event will occur at larger depths with increasing thickness. The plot of the average contact pressure at the rupture event, plotted in Figure 3.3.7 (c), suggests that the graphene layer can support lubrication at high normal contact pressures up to approximately 10 GPa. Further experimental studies are required to determine the origin of the scatter however the critical rupture does not appear to be solely dependent on the normal contacting pressures. This indicates that the rupture is due to wear of the graphene sheet which may depend on the normal contacting pressure, number of lateral oscillation cycles, the initial state of stress within the graphene layer, and environmental contaminants within the contact. Shown in Figure 3.3.7 (d) is a plot of $dS_x / d\delta_z$ against the number of graphene layers which was obtained by linearly fitting the lateral stiffness, (S_x) against the initial indentation depth (δ_z) of between 0 and 20nm. The data suggests that there is a thickness dependency upon the friction of graphene with decreasing friction with increasing number of layers.

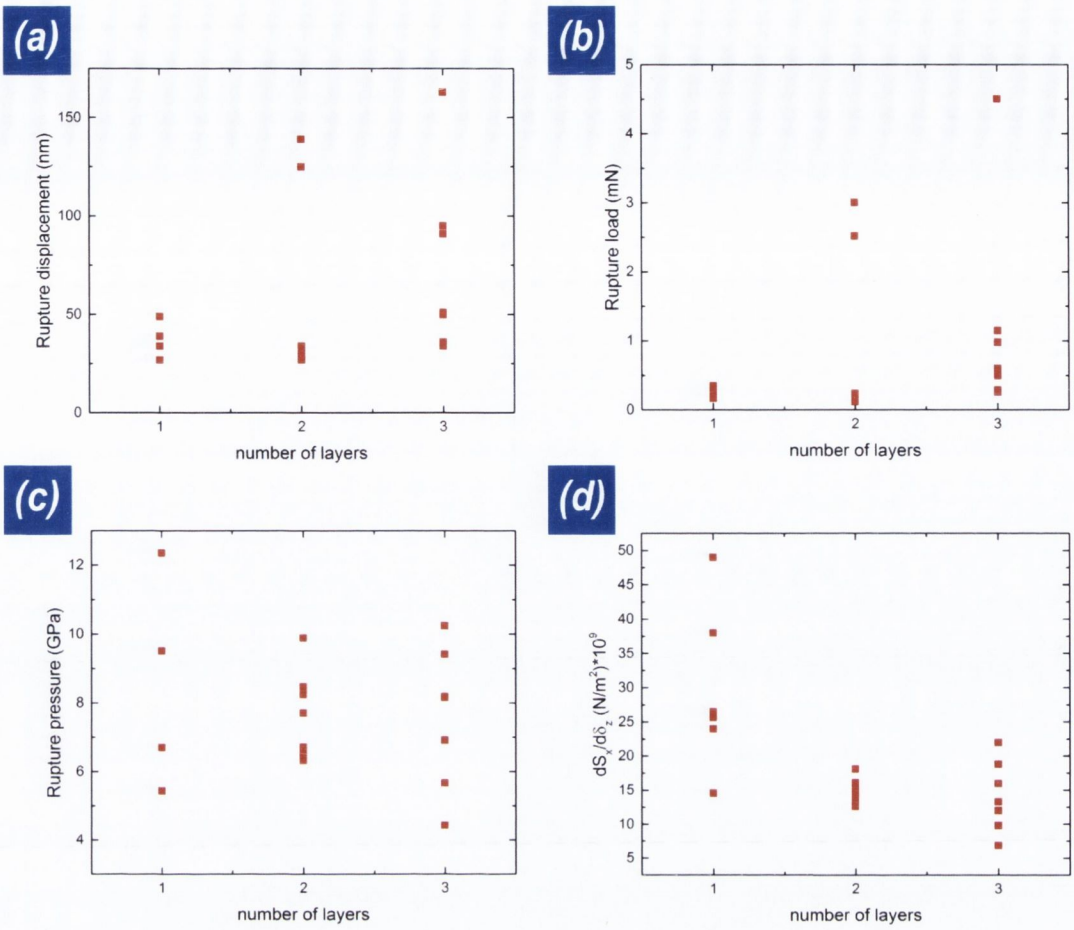

Figure 3.3.7: Summary of the critical rupture events of 20 indentations into SLG, BLG and TLG surfaces. (a) Plot of the critical rupture displacement against the number of layers, (b) plot of the critical load against the number of layers, (c) plot of the average contact pressure at rupture against the number of layers and (d) plot of $dS_x / d\delta_z$ against number of layers.

Shown below in Figure 3.3.8 (a) is a plot of the load against displacement of a series of indentations on a BLG and SiO_x surfaces without any lateral oscillations. While the plot shows a small amount of scatter in the maximum displacement and the final depth of the impression the overall elastic and plastic behaviour is similar to the previous indentations performed on the SiO_x and graphene surfaces. The AFM images shown in Figure 3.3.8 (b) and (c) indicate a lack of any bunching or wrinkling at the periphery of the contact. This provides confirmation that the bunching and wrinkling of the examples shown in Figures 3.3.4 and 3.3.5 are due to the cyclic oscillations in the lateral direction.

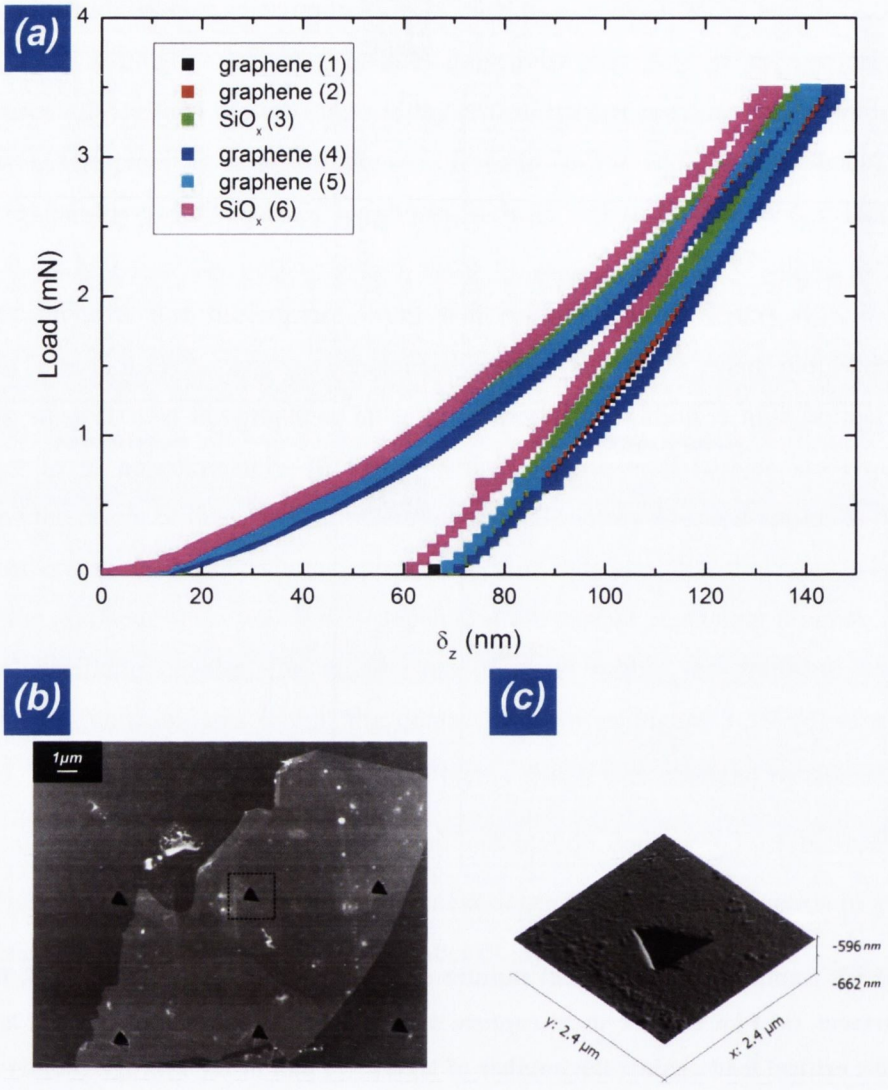

Figure 3.3.8: Example of an indentation into a BLG surface without any lateral oscillation. (a) plot of the load vs indentation depth, (b) tapping mode height AFM image of the residual impression, (c) 3D representation of the residual impression shown by the black box within (b).

3.3.2 CVD graphene

Shown below in Figure 3.3.8 (a) is a plot of the load against displacement of a series of indentations performed on a single layer of CVD graphene deposited on an SiO_x substrate. The load displacement curves are qualitatively similar to all of the previous indentations on graphene/SiO_x and bare SiO_x surfaces however there is a relatively large scatter in the maximal displacements and the depths of the final impressions between tests. The measurements of the lateral stiffness, shown in Figure 3.3.8 (b), show qualitatively similar behaviour to the indentations on the mechanically exfoliated graphene, with low lateral stiffness up to depths of approximately $40nm$ followed by a discontinuous jump however

there is large scatter in the lateral stiffness behaviour. The AFMs of the residual impression demonstrate the surface roughness and contamination of the CVD graphene layer which may be the source of the scatter in the load displacement behaviour and the lateral stiffness of the contact during indentation.

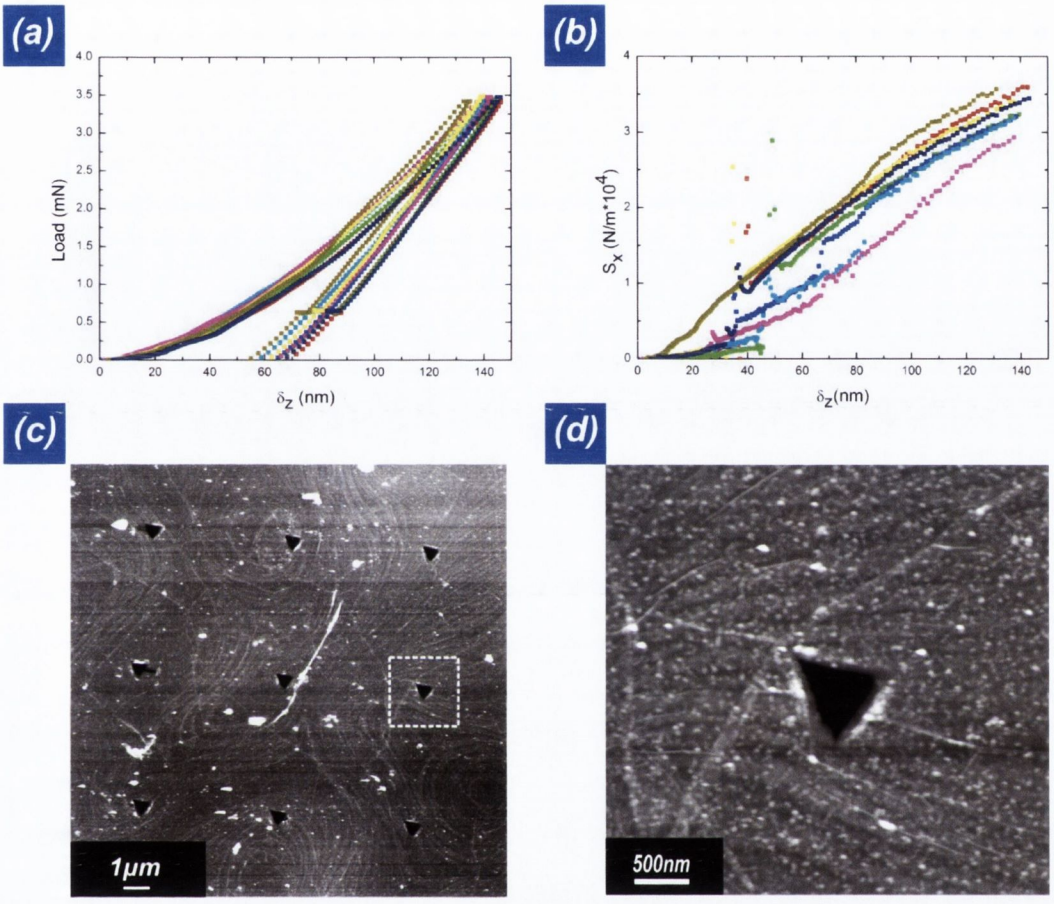

Figure 3.3.9: Series of indentations into a single layer of CVD graphene. (a) plot of the load vs indentation depth, (b) plot of the lateral stiffness vs indentation depth, (c) tapping mode AFM image of the residual impressions of indentations (d) zoomed in tapping mode height AFM image of the residual impression of one of indentation which is shown by the white box within (c).

3.3.3 hBN

The indentations performed on the mechanically exfoliated hBN sample show similar behaviour to indentations performed on the bare SiO_x with little difference between the gross elastic and plastic deformation. The lateral stiffness measurements also show similar behaviour to the graphene surfaces with an extended region of low lateral stiffness's followed by a non linear increase in the lateral stiffness with a large discontinuous jump in the lateral stiffness's at depths between 30 and 50nm. The fact that the low stiffness is

common to both the graphene and the hBN sheets suggests that the low lateral stiffness is due to the weak Van der Walls bonding between the tip, the quasi 2D sheet and the substrate. The bunching and folding of the hBN can be seen at the periphery of the residual impression shown by the AFM in Figure 11 (c), which is most likely due to the oscillatory lateral motion of the tip after the rupture of the hBN as outlined in the introduction.

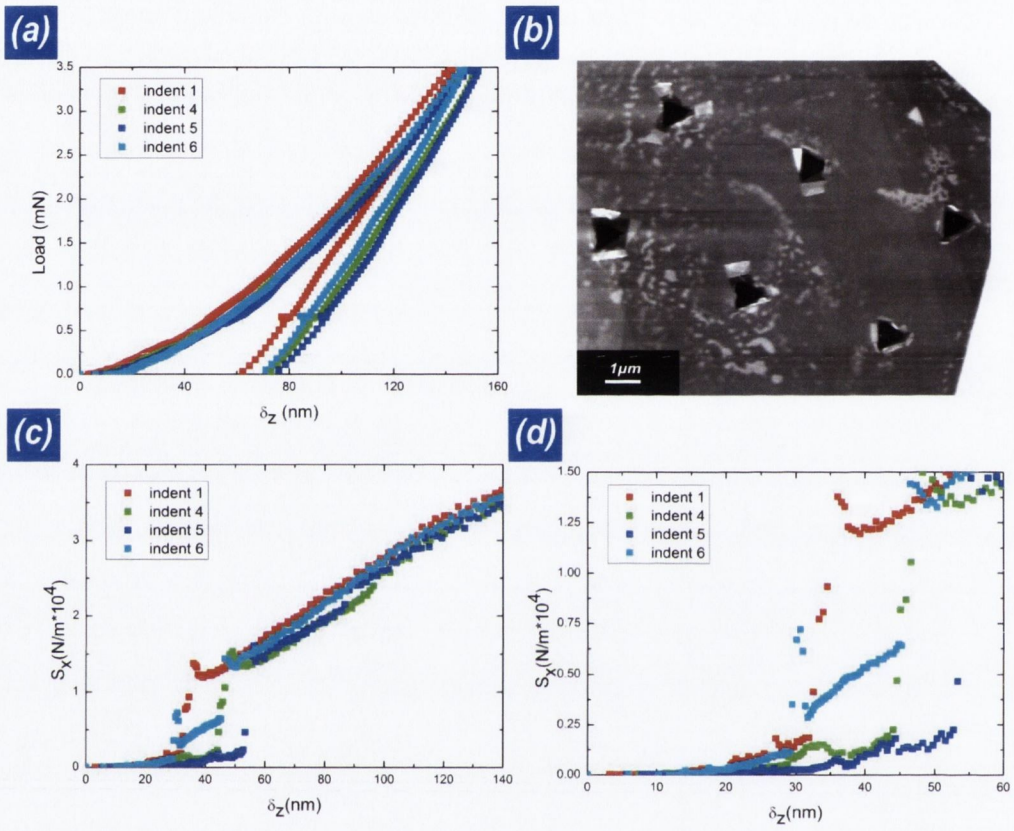

Figure 3.3.10: Example of indentations into hBN surface. (a) plot of the load vs indentation depth, (b) tapping mode AFM image of the residual impression of indentations,(c) and (d) plot of the lateral stiffness measurements vs indentation depth.

3.4 Conclusion

The tribological properties of quasi 2D sheets have been investigated by the 3D nano contact system by imposing oscillations of between 1 and 2 nm's in the lateral direction during conventional indentation. The phase sensitive lateral oscillations allow for the measurement of an in phase elastic stiffness and an out of phase damping coefficient, from which the elastic and dissipative contributions can be determined. The experiments have shown the general lubrication properties of graphene by the dramatically reduced lateral stiffness of the contact when even a single layer of graphene is placed between the contacting surfaces. The lateral stiffness's of the SLG contacts were found to be significantly higher than contacts in BLG or TLG surfaces, at all depths prior to rupture, which suggests that few layer graphene has superior tribological properties in comparison to SLG. We suggest that the reduced lateral stiffness's of the contacts in few layer graphene is due to an increase in the weak Van der Waals interactions between graphene layers. Single layer graphene, in direct contact with the tip and the substrate, results in different interactions with an increased elasticity within the contact at higher contacting pressures. The reproducibility of the lateral stiffness's during loading and unloading prior to the critical jump in the stiffness indicates that the critical jump is due to irreversible rupture of the graphene layer which results in a loss of lubrication however the load displacement curves indicate that no significant deformation occurs within the indentation volume during the critical rupture.

The CVD and the hBN samples were both found to lubricate the SiO_x surface which indicates that the lubrication is inherently due to the weak Van der Waals interactions between the tip, the sheets and the substrate. The scatter in both the load displacement and the lateral stiffness measurements of indentation testing on the CVD sample indicate that the lubricating properties of the sheets are sensitive to contamination. The lateral stiffness measurements during indentation have been shown to be a useful method of investigating the tribological properties of surfaces because the measured lateral stiffness's of the contacts are sensitive to alteration of the surfaces by wear or plasticity.

Chapter 4: Self Assembly of Graphene

4.1.1 Introduction

The reorganisation of matter through the minimisation of surface free energy is ubiquitous throughout nature. This is commonly observed in liquid solid interfaces where a film of liquid reforms into droplets on the solid through free energy minimisation. While the reforming of solids through minimisation of free energy is possible, for example Wulff facets in nanoparticles [91-92]. It is, however, most usually prohibited on experimental time scales since solids typically have very limited degrees of freedom and require relatively high energies to reform. The focus of this chapter is in presenting a new phenomenon which involves spontaneous and directed reorganisation of graphene, a quasi 2D solid, into self assembled folded structures through spontaneous folding, sliding and fracture. We believe this self-assembly process is ultimately driven by a reduction of the free energy of the graphene sheet by the reduction of the area of the exposed graphene surface. It is demonstrated within this chapter, that the self assembly process can be nucleated and directed by an indentation process that may be scalable over large areas. The graphene self assembly process in some ways resembles liquid reorganisation, however there are significant differences. The shape change of liquid involves multiple local degrees of freedom, while the reorganisation of the carbon atoms in the graphene sheet is constrained by the 2D bonding within the lattice. This leads to a difference in the inherent length scales of the processes. Liquid reforms on the order of the molecular length in all directions however the strong in plane C-C bonds in graphene require the cooperative collective behaviour over the entire length scale of the structure which can be on the μm length scale.

Self-assembly is the autonomous organization of material into spatial patterns and structures which is of particular importance in the fabrication and processing of materials at the nanoscale where conventional top-down forming techniques can be prohibitively time consuming, expensive or ineffective. The self-assembly of the folded structures described within this chapter requires a graphene sheet free edge to fold over onto itself. This requires an initiation process. Once the fold has been formed the self-assembly will progress by sliding and tearing by driven thermal energy and residual stress within the sheet. Spontaneous nucleation, although rare, has been observed throughout the course the experiments and is represented by the schematic representation in Figure 4.1.1.

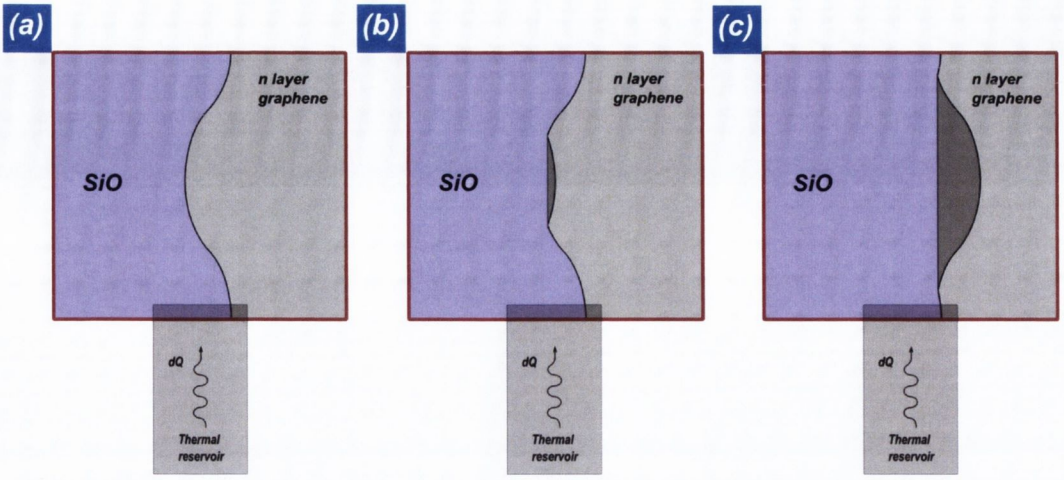

Figure 4.1.1: A schematic representation of a spontaneous nucleation and growth of a folded structure in graphene. (a) The initial free edge, (b) the nucleation of a fold by thermal energy and (c) the final state.

Alternatively the folding process can be directly achieved by nanoindentation, the main features of which are shown by the schematic in Figure 4.1.2. The nucleation occurs by creating a new free edge within the flake by puncturing the graphene with the indenter. The folding of the free edge is achieved by the rapid and successive lateral oscillations imposed on the contact, which was described in chapter 3. The self assembly can then progress by the propagation of two distinct fracture paths which propagate in union. The first, labelled fracture 1, is a conventional mode I interfacial fracture between the graphene and the SiO_2 surfaces. The second fracture, labelled fracture 2, is a quasi 1D mode III fracture which propagates on both sides of the fold along the graphene lattice by the dissociation of individual carbon-carbon bonds. The indentations have produced a variety of folded structures however the vast majority of the structures resemble the tapered ribbon structure shown in Figure 4.1.2. The self assembly process may eventually prove to be a useful, scalable, high throughput imprint technique for producing folded structures in graphene. The process also involves fracturing of the graphene lattice which could be a potential route for controlling the edge structure in fabricated graphene structures. More generally the process could provide an experimental platform for investigating the mechanics of quasi 2D materials such as fracture, adhesion, sliding and folding.

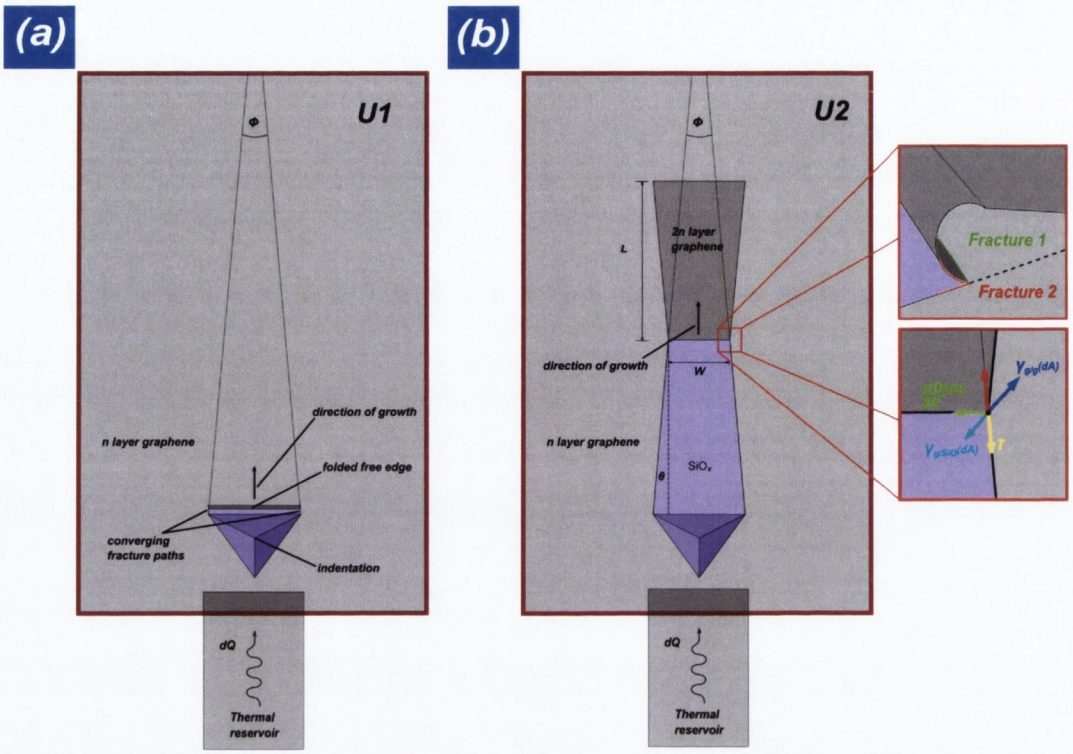

Figure 4.1.2: Schematic representation of the geometry of the folded ribbons produced through indentation. The tapering angle is represented by θ. The geometry of the fold line is represented within the red inset and the graphene lattice is represented within the blue inset.

In the following sections the sliding, peeling, folding and fracture are discussed separately before attempting to show how each aspect cooperates together to produce the growth of the folded structures. Since the predominant way in which the phenomenon could be studied was through nucleation via nanoindentation the focus of our discussion is mainly on the folded ribbon structure shown in Figure 4.1.2. It should be noted however that the presented analysis may be applied to the more general spontaneous self-assembly processes in 2D materials.

4.1.2 Superlubricity

The growth of the folded ribbon occurs by the relative sliding between the surface of the ribbon and the underlying flake. This involves the traversing of a potential landscape which is strongly dependant on the stacking order between the contacting graphene surfaces. The lowest energy AB Bernal stacking configuration between two graphene surfaces in contact is shown by the schematic in Figure 4.1.3. In this configuration the relative motion between the two surfaces is hindered by the relatively high potential corrugation associated with the perfect matching of the periodicities of the lattices. As the in plane orientations of the lattices are rotated with respect to one another, between 0^0 and

60^0, the lattice matching breaks down and the interface becomes incommensurate. The sliding behaviour of incommensurate graphite has been studied by imposing an external lateral force on the contact which has revealed the remarkably small friction coefficient between incommensurate contacts and a much higher friction coefficient between commensurate contacts [26-27, 55]. Theoretically, Shibuta et al used the Lenard-Jones potential to calculate an energy barrier of 0.15meV/atom and 0.03meV/atom for transitions between successive commensurate AB states along the zig-zag and armchair directions, which is shown schematically in Figure 4.13, however for incommensurate graphene surfaces no AB states exist and the potential corrugation is effectively flat with a very small potential barrier opposing the tangential or rotational motion of the surfaces [93]. While the energy barrier per atom for successive transitions between AB states, for both the ZZ and AC directions, is low in comparison to the room temperature thermal energy of 0.025eV the collective energy barrier is proportional to the number of sliding atoms within the contact [28]. This ensures the stability of commensurate graphite of any appreciable size.

Recently the sliding behaviour of incommensurate, nanosized graphene flakes ($100nm^2$) has been studied in the absence of any external lateral force, instead the sliding is activated by thermal energy which results in the diffusion of the nano flake across the underlying graphene sheet, even at temperatures as low as 5K [94]. This diffusion confirms the remarkably small potential corrugation between the incommensurate graphene surfaces however the motion of the graphene flake by diffusion is only expected to be dominant where the thermal energy is larger than the collective energy barrier opposing the motion of the flake [95]. The contact areas of the self assembled structures we have produced are on the order of micrometers and so we do not expect diffusion to dominate the growth.

A series of experimental studies on the self retraction of sheared micrometer sized graphite blocks have revealed thermally activated motion between the incommensurate graphite surfaces whereby the motion is driven by the minimisation of the exposed surfaces due to the shearing [33, 36]. This self retraction behaviour of the sheared incommensurate graphite blocks resembles fluid like behaviour since the incommensurate graphite appears to be unable to support shear stress. The full reversibility of the sliding graphite surfaces under repeating shearing cycles indicate that the interface remains largely unaffected by adsorbed atmospheric molecules even when the experiments are conducted in ambient conditions. From this we can infere that atmospheric contamination does not play a significant role in the sliding behaviour of the folded ribbons produced during the experiments is made.

Theoretical considerations of superlubricious behaviour assume perfectly rigid contacting surfaces however graphene behaves as a 2D membrane with out of plane fluctuations [86]. It is not well understood how flexural, non rigid behaviour over large contact areas may effect superlubricity or what effect the edge states have on the sliding behaviour. Recent experiments performed by Yang et al suggest that the edges of the sliding interfaces may have a large effect on the superlubricious behaviour since the velocity of the self retraction was dramatically altered by deliberately introducing defects on the edges of the graphite blocks [96]. This suggests that the edge defects introduce local pinning points which affect the overall sliding behaviour.

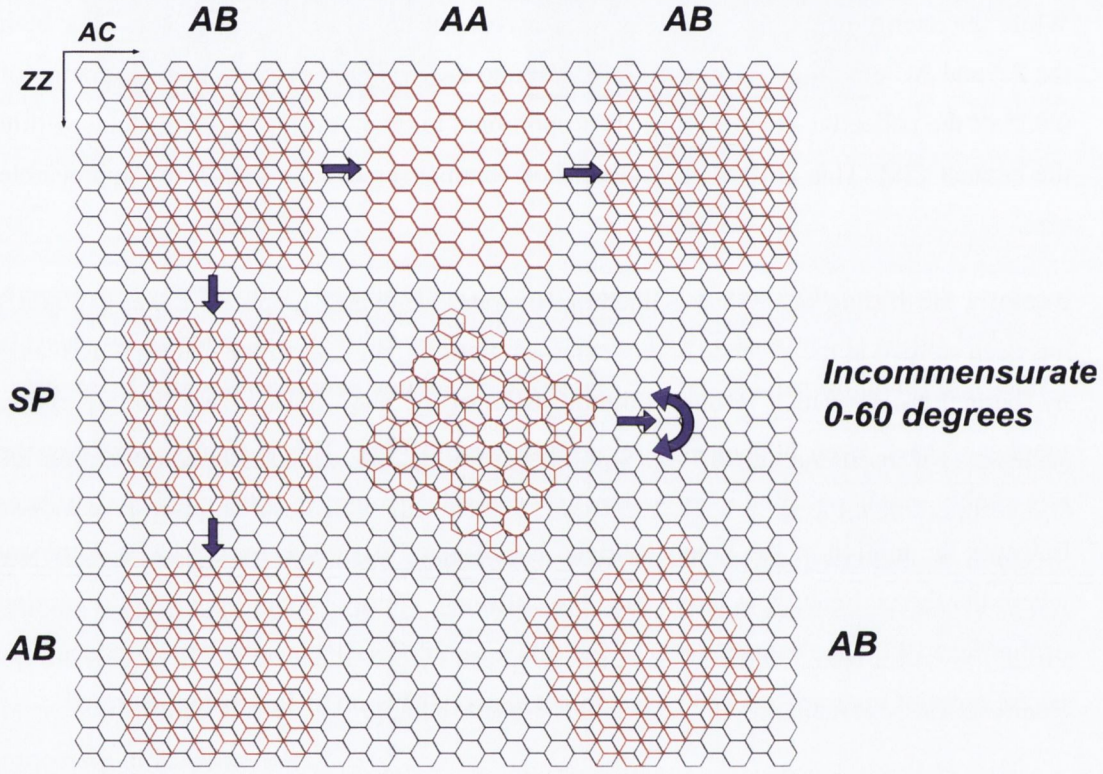

Figure 4.1.3: Schematic representation the sliding of commensurate surfaces along the ZZ and AC directions and incommensurate contacts.

We define the direction of growth as the vector perpendicular to the fold line which is shown in Figure 4.1.2. The initial direction of the growth is governed by the nucleation event which involves the creation of the free edge, the two converging fracture paths and the fold. The direction of the growth is only conserved if the fracture rates along both sides of the lattice are equal however since there is negligible opposition to the relative rotation between the folded ribbon and the underlying sheet we suggest that the direction of the growth is free to rotate if the fracture rates differ between the sides of the fold. Rotation can also occur if there is a barrier or pinning point which fixes only one side of the folded

ribbon. In that case the fracture will propagate only on one side of the fold which may produce significant rotation of the direction of the growth. The rotation may be sufficient to allow the ribbon to fall into commensurability with the underlying flake which completely stalls the growth, which has been observed during the course of our experiments.

We determine the stacking order of the folded ribbons via the characteristic Raman signature of non AB stacked graphene, which stands in good agreement with previous studies [76-77]. AB Bernal stacking of graphene results in a broadening of the 2D band with increasing thickness due to the interaction of the electronic band structure between layers, however incommensurately stacked graphene does not result in a broadening of the 2D band. Instead the 2D band remains effectively the same as the underlying flake although the 2D intensity continues to rise nearly linearly with increasing thickness. This provides a quantitative determination of the stacking order of the folded ribbons which we have used to demonstrated the incommensurability between the ribbons and the underlying flake and we suggest that the growth of the folded ribbons is due to the inherent easy sliding between the incommensurate surfaces.

4.1.3 Fracture/Wetting mechanics

In the spirit of both classical fracture and wetting analysis a thermodynamic energy balance approach is taken to try to understand the growth and stopping conditions of the folded structures. This thermodynamic analysis was first introduced by Griffith to understand the failure criterion in brittle materials [97]. The theory attempts to model a static fracture as a reversible thermodynamic process where the total energy within the system, U, is composed of released elastic energy, $U_{elastic}$, and the energy expended in creating free surface area within the crack front, $U_{fracture}$.

$$U = U_{elastic} + U_{fracture} \tag{4.1}$$

Any advance of the fracture results in a reduction of the stored elastic energy within the system thereby driving the growth forward however the advancing fracture results in an energetic cost in creating free surface within the crack front. The system will always find the lowest energy configuration and the equilibrium condition is given by

$$\frac{dU}{dL} = 0 \tag{4.2}$$

where L is the length of the crack.

Usually the stored elastic energy within the system is applied by some external load. We take the example of uniform tension acting across an elliptical crack [98], which is shown by the schematic in Figure 4.1.4, to illustrate the stability condition. The change in the stored elastic energy per unit crack width is given by

$$U_{elastic} = \frac{\pi L^2 \sigma_A^2}{E} \tag{4.3}$$

where σ_A is the applied stress and E is the elastic modulus.

The fracture energy per unit crack width is given by

$$U_{fracture} = 4L\gamma \tag{4.4}$$

where γ is the energy expanded per unit area in creating free ideal surfaces and the factor of 4 accounts for the for the propagation of the cracks in both directions.

The total energy of the system is then given by

$$U = 4L\gamma - \frac{\pi L^2 \sigma_A^2}{E} \tag{4.5}$$

By taking the differential of the total energy of the system with respect to the length of the crack we can obtain the equilibrium condition which is given by

$$\frac{dU}{dL} = 4\gamma - \frac{2\pi L_{eq} \sigma_A^2}{E} = 0 \tag{4.6}$$

where L_{eq} is the length of the crack during the equilibrium condition.

The Griffith criterion led to the prediction that the critical stress, σ_{crit} , that any pre existing crack can support is inversely proportional to the square root of the initial length of the crack, L_{in} , which is given by

$$\sigma_{crit} = \sqrt{\frac{2\gamma E}{2\pi L_{in}}} \tag{4.7}$$

The second stability condition is given by the sign of the second derivative of the total energy of the system with respect to the length of the crack which is given by

$$\frac{d^2U}{dL^2} = -\frac{2\pi\sigma_A^2}{E} < 0 \tag{4.8}$$

If the critical stress is overcome the fracture will propagate forward attempting to reach a new equilibrium however if the second derivative with respect to the length is negative, as in the case of equation (4.8), then the reduction in the elastic energy released will always be larger than the energy required to fracture. This results in catastrophic dynamic fracture of the material. If the second derivative is positive then the fracture can propagate until a new equilibrium is reached. The example of the elliptical crack with the energy defined by equation (4.5) is unstable under any perturbation which either results in unbounded fracture under by surpassing the critical stress or in the full healing of the crack under the removal of stress.

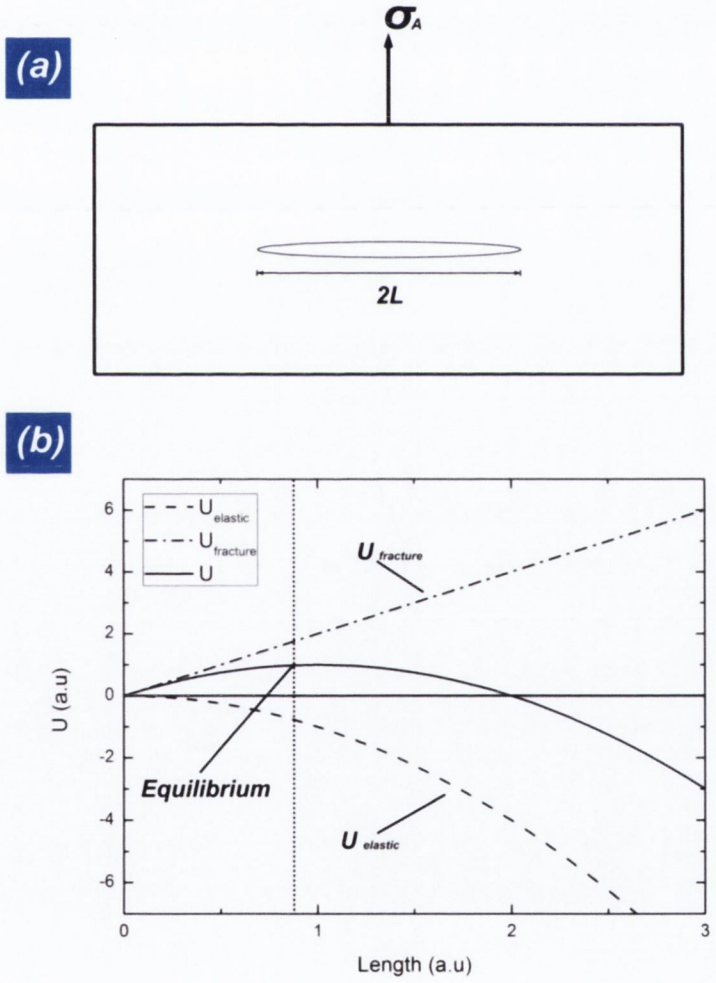

Figure 4.1.4: (a) schematic representation of a tensile stress acting across an elliptical crack in a semi infinite half space, (b) plot of the total energy of the system against the crack length in arbitrary units.

Dynamic fracture is term used to describe non equilibrium states of fracture where

$$\frac{dU}{dL} \neq 0 \tag{4.9}$$

This typically results in the crack propagating at high velocities which is limited by the speed of elastic waves within the material, which ranges from km/s to m/s. Subcritical fracture can also occur where the state of stress within the crack front is less than the critical stress for dynamic fracture to occur, which is usually described as kinetic growth with crack velocities typically ranging from m/s to less than nm/s. Kinetic growth can only be described by the local behaviour of the material within the crack front which may be due to extraneous variables such as the concentration of environmental species and temperature.

4.1.4 Sub-critical atomic scale fracture

Continuum mechanics is governed by macroscopic elastic and plastic properties, which are length scale independent, however it becomes inapplicable at length scales where microstructure become significant. A crack front cannot be infinitely sharp and must be limited by the lattice bond length which is shown schematically in Figure 4.1.5. The terminating bond within the crack front is subject to the maximal stress and strain. It is also subject to thermal fluctuations, so if the state of stress within the crack front is less than the critical bond dissociation stress the discrete bond breaking steps necessary for crack propagation can still occur by overcoming an activation energy barrier, ε_b [99]. If a thermal fluctuation is sufficient to break the bond the fracture propagates forward by one atomic step. Alternatively the bond can heal by thermal energy and the fracture can recede by an atomic step, which is shown schematically by Figure 4.1.5. The forward and reverse fracture processes result in successive discrete changes in the energy of the system. This process can be understood by rate activation theory where the rate of activation, ψ , is the average number of times the energy barrier will be overcome per unit of time, given by

$$\psi = \frac{k_B T}{h} \exp^{\left(\frac{-\varepsilon_b}{k_B T}\right)} \tag{4.10}$$

where k_B is Boltzmans constant, T is the absolute temperature and h is planks constant.

The velocity of the crack, v will then be given by the product of the rate of activation and the atomic spacing over which the discrete event occurs which is given by

$$v = a_0\psi = \frac{a_0 k_B T}{h} \exp^{\left(\frac{-\varepsilon_b}{k_B T}\right)} = v_0 \exp^{\left(\frac{-\varepsilon_b}{k_B T}\right)} \tag{4.11}$$

where v_0 is a constant used to simplify the expression.

For the case of the atomic scale fracture shown in Figure 4.1.5 there are two rates in question: The rate of bond breaking and the rate of bond healing. The crack front is said to be in equilibrium if the rate of bond breaking is the same as the rate of bond healing which is represented by the schematic in Figure 4.1.5 (e). Any additional elastic strain energy within the crack front will distort the energy barrier, ε_b , by an amount, E_f , however the elastic energy also prohibits the reverse healing direction by an amount, E_r , [100] which is shown by the schematic in Figure 4.1.5 (f). Similarly the reduction of any elastic energy within the crack front can result in distortion of the energy barrier, ε_b , which favours the healing direction, shown in Figure 4.1.5 (d). This distortion results in an effective energy barrier which is given by

$$\varepsilon_b + E_{f/r} \tag{4.12}$$

The crack velocities for the breaking and healing directions will then be given by

$$v_f = a_0\psi_f = v_0 \exp^{-\left(\frac{\varepsilon_b + E_f}{k_B T}\right)} \tag{4.13}$$

and

$$v_r = a_0\psi_r = v_0 \exp^{-\left(\frac{\varepsilon_b + E_r}{k_B T}\right)} \tag{4.14}$$

where v_f and v_r are the velocity of the fracture in the breaking and healing directions and , E_f and E_r are the free energies which distort the energy barrier for the bond breaking and healing directions.

The net direction and velocity of the crack front can be found by adding the forward and backward velocities which is given by

$$v = v_0 \exp^{-\left(\frac{\varepsilon_b + E_f}{k_B T}\right)} + v_0 \exp^{-\left(\frac{\varepsilon_b + E_r}{k_B T}\right)} \tag{4.15}$$

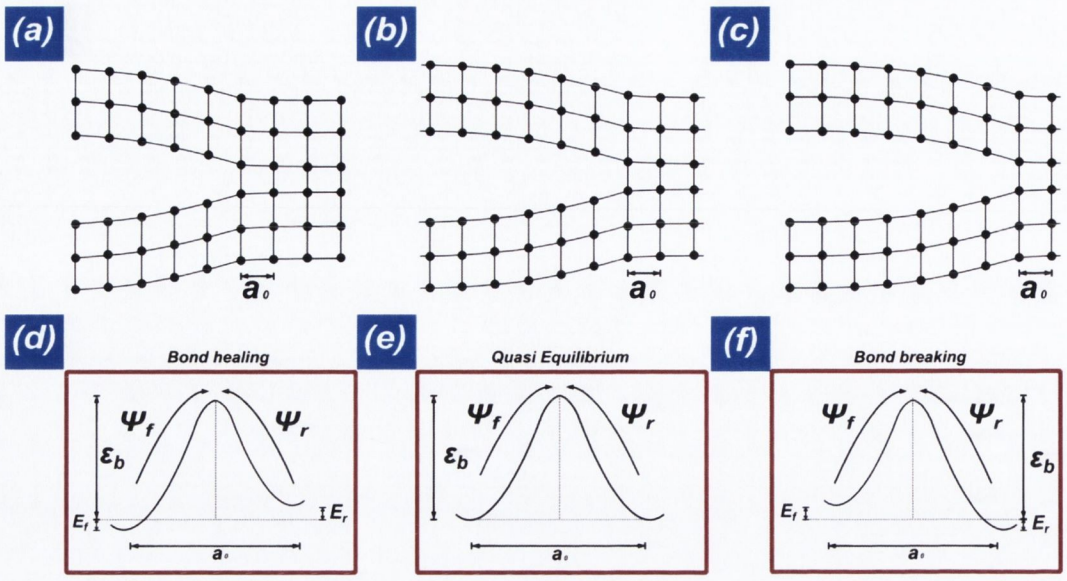

Figure 4.1.5: Schematic representation of atomic scale fracture. (a) receding atomic scale fracture, (b) quasi equilibrium fracture, (c) propagating fracture, (d) energetic landscape of a receding atomic scale fracture, (e) energetic landscape of an atomic scale fracture in quasi equilibrium, (f) energetic landscape of a propagating atomic scale fracture.

Rate activation theory is usually experimentally studied in one of two ways. The first is to fix the temperature and see the exponential scaling with a change in the effective energy barrier and the second is to fix the energy barrier and to see the exponential scaling in the rate with change in temperature. For example Schuh et al have used nanoindentation to study the rate activated onset of atomic scale plasticity in metals by changing the rate of loading [101] and by changing the temperature [102] which were both found to have exponential scaling in the rate like that of equation (4.10). The versatility of rate theory is in the exponential scaling resulting in sensitivity to small changes in the energy barrier or in the temperature.

In a similar way to the Griffith fracture analysis we attempt to establish the thermodynamic potentials which quantify the surface energies, the stored elastic energies and the energies of fracture to determine the conditions for the growth of the folded structures. Although the folded ribbons are not in thermodynamic equilibrium during the growth it is suggested that the energy within the system boundary is determined by summing the instantaneous values of the thermodynamic potentials. For the purpose of the analysis of the chapter we focus on the folded ribbon structure produced by nanoindentation, shown by the schematic in Figure 4.1.2. Two distinct tapering angles ϕ and θ are defined to characterise the tapering of the ribbon. The total tapering angle (ϕ) is defined as the separating angle between fracture paths which is representative of the global tapering of the ribbons. The

local tapering angle (θ) is defined in relation to the fold which is representative of the individual fracture path along the graphene lattice on either side of the fold. The two tapering angles are defined since the folded ribbons were often not symmetrical with respect to the direction of growth, where $\theta_1 \neq \theta_2$. The length of the ribbon is defined by the distance between the leading edge and the fold line. The measurements of the ribbons incur a systematic error since the leading edge is typically arbitrary in shape. In this case the length is measured by the furthest point perpendicular to the fold line. The final geometric parameter is the width, W which is shown by the schematic in Figure 4.1.2. The geometric system can only be applied to ribbons with smooth tapering where no abrupt changes in the width or tapering occur. Abrupt changes in the width have only occurred at high temperatures and the parameters were sufficient to characterise the geometry of the folded ribbons which were formed at room temperature.

4.1.5 Interfacial energy

We first consider the change in the energy of the system by considering the advance of fracture 1. Conventional fracture mechanics usually involves only the separation of surfaces however any advance of fracture 1 results in an increase of surface area, dA, of exposed SiO_x and of the graphene/graphene interface between the ribbon and the underlying flake together with a, $2dA$, reduction of the exposed underlying graphene flake. The binding energy between two surfaces in contact is usually defined as the reversible work required to separate two ideal free surfaces, in the absence of any dissipative mechanisms [103]. This assumption is adopted with the understanding that it represents an idealisation. We combine the Dupree equations for the advance of the graphene/graphene interface and the receding of the graphene/SiO_x interface as

$$\frac{dU_{surface}}{dA} = \gamma_{graphene/graphene} + \gamma_{SiOx/air} + \gamma_{2n/air} - 2\gamma_{n/air} - \gamma_{SiOx/graphene} = \gamma_{net} \tag{4.16}$$

Recent experimental and theoretical studies have given values of the binding energy between graphene and SiO_x ($\gamma_{SiOx/graphene}$) which range between 0.4-0.2J/m^2 [104-107], which may vary depending upon surface roughness and atmospheric contamination [108]. The experimental and theoretical investigations into the binding energy between graphene sheets ($\gamma_{graphene/graphene}$) appear stand in reasonable agreement with values ranging from 0.26-0.23J/m^2 [93, 109]. It is not clear what affect the number of layers may have on the binding energies and for the sake of the analysis within this chapter we assume that it is independent of the number of layers and a value of γ_{net} =0.04J/m^2 was obtained by fitting

the experimental data to the model. The change in energy, $dU_{surface}$, due to the advance of fracture 1 is represented by

$$dU_{surface} = dA_{ribbon}[\gamma_{net}] \tag{4.17}$$

We define $F_{surface}$ as the change in energy per unit change in length which represents an effective force driving the growth of the folded ribbons as

$$F_{surface}(\theta, L) = \frac{dA_{ribbon}}{dL}[\gamma_{net}] \tag{4.18}$$

A typical example of the tapering of the folded ribbons is shown schematically in Figure 4.1.6 (a). The area of the folded ribbon can be formulated in terms of the length, L , the initial width, $W_{initial}$, and the tapering angle, θ , given by

$$A_{ribbon} = W_{initial}L - L^2\tan(\theta) \tag{4.19}$$

from which the change in the area per unit change of length can be obtained by differentiation with respect to the length as given by

$$\frac{dA_{ribbon}}{dL} = W_{initial} - 2L\tan(\theta) \tag{4.20}$$

Plotted in Figure 4.1.6 (b) is a plot of the expected change in the energy of the system due to the advance of fracture 1 for an initial width of 800nm and tapering angles of 1^0, 5^0 and 10^0 with γ_{net} =0.04J/m^2. The analysis suggests that the propagation of fracture 1 results in an overall decrease in the energy of the system which favours the growth of the ribbon. The analysis also suggests that fracture 1 should not result in an unstable propagation since the thermodynamic potential which drives the growth diminishes with the length of the ribbon, which can be seen by the plot of $F_{surface}$ in Figure 4.1.6 (c). Both plots also highlight the effect of increasing the tapering angle which is less energetically favourable with regards to the advancement of fracture 1. Any finite tapering ensures that the change in the energy of the system is bounded by the area of the ribbon at the break off point. The breaking off of the folded ribbons has not been observed during the course of the experiments described within this chapter which may be due to the diminishing thermodynamic potential as the break off point is approached.

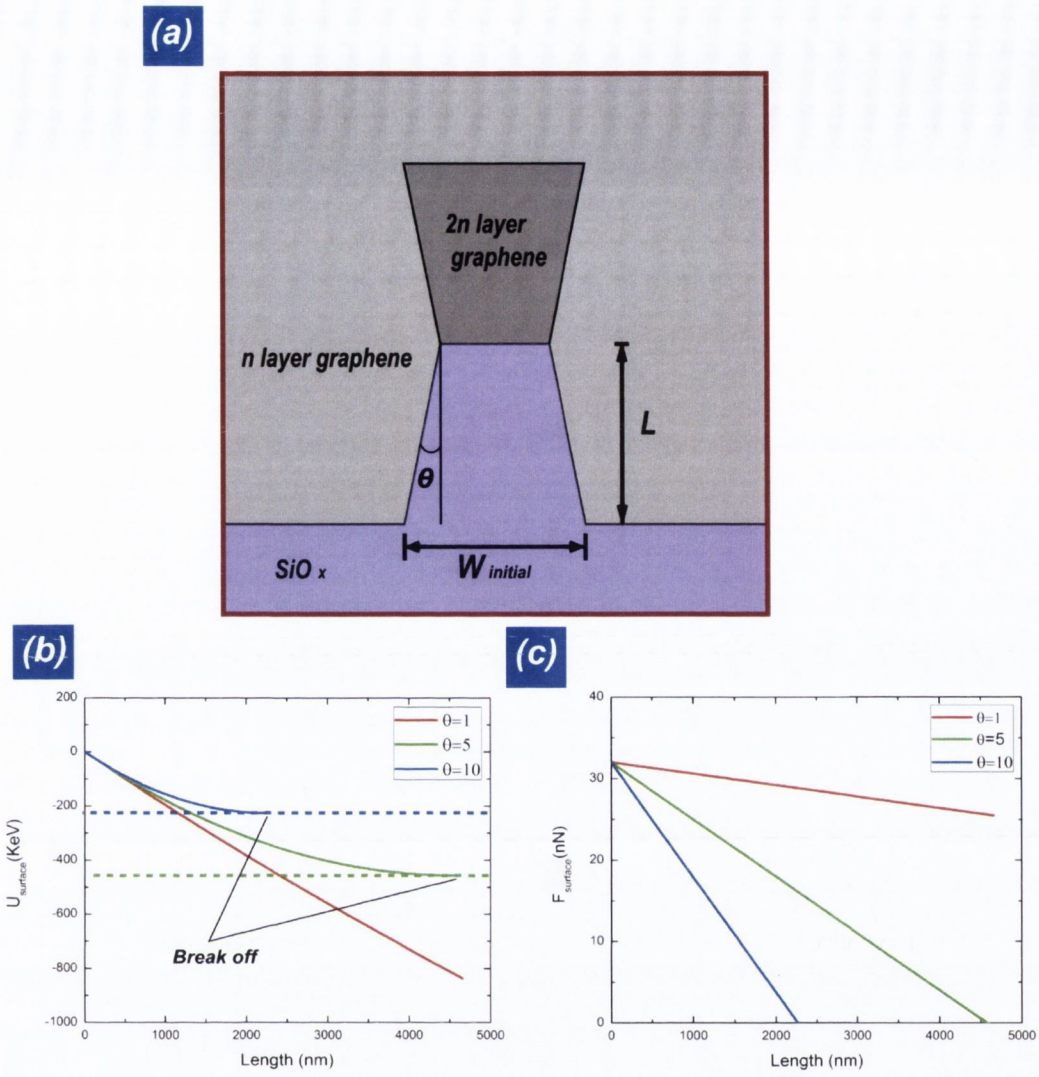

Figure 4.1.6: (a) Schematic representation of the change in the area of a folded ribbon, (b) plot of the change in the energy of the system due to the change in the surface energies of the SiO_x, n and 2n layer graphene against the length of the ribbon (c) plot of the effective force $F_{surface}$ against the length of the ribbon.

4.1.6 Elastic strain energy

Since no external forces act upon the folded ribbons during the growth it is concluded that all of the elastic strain energy remains within the fold. The folded ribbon lies in conformal contact with the underlying flake due the unique mismatch between the relatively high in plane bond strength and the low bending stiffness of graphene. This quasi 2D folding produces a small volume of strained C-C bonds along the fold line which is represented by the schematic in Figure 4.1.7. The strain energy per unit area of the fold, E_{fold} , can be written as

$$E_{fold} = \frac{D\kappa^2}{2} \tag{4.21}$$

where D is the out of plane bending modulus and κ is the curvature of the fold [110].

The area of the fold can be approximated by ignoring edge effects, which are small in comparison to the typical size of the widths, by the product of the circumference of the fold and the width, which is shown schematically in Figure 4.1.7 (c) and is given by

$$A_{fold} = \pi RW \tag{4.22}$$

The total elastic strain energy within the fold is given by

$$U_{fold} = A_{fold}\left[\frac{D\kappa^2}{2}\right] = \frac{\pi \mathrm{RW}\, D}{2R^2} \tag{4.23}$$

Due to the converging tapering of the FR's, the width of the fold decreases as the length of the ribbon increases thereby reducing the strain energy [111]. The change in the strain energy per unit change in length is then given by

$$\frac{dU_{fold}}{dL} = F_{fold}(\theta) = \frac{\pi \tan(\theta) D}{2R} \tag{4.24}$$

A summary of the measurements of the radius, R , of the fold, the bending modulus per unit area, D , and the strain energies per unit area for single bi and tri-layer graphene are given below in table 4.1.1. While Sen et al [110] have only considered complete AB stacking during the bending of the graphene lattice, Gong et al [112] have shown the loss of Bernal stacking of graphene under strain by the nucleation of dislocations. Considering that the folded ribbons produce a tight fold resulting in large strain producing a high density of dislocations, it is assumed that there is full slip between adjacent graphene layers [109]. For this reason it is assumed that the bending modulus increases linearly with increasing thickness, where D=2.1eV [110], as given in table 4.1.1.

Number of layers	R(nm)	D(eV)	$E_{fold}(eV/nm^2)$
1	0.8	2.1	1.64
2	1.8	4.2	0.64
3	2.2	6.3	0.65

Table 4.1.1: Measurements of the Radius of the fold, the bending modulus and the strain energy per unit area for single bi and tri layer graphene.

Plotted in Figure 4.1.7 (d) is the theoretical change in the elastic strain energy of the system against the length of the ribbon, from which the energetic favourability of the tapering can be seen since diverging fracture paths would result in an increase in the width of the fold thereby increasing the elastic strain energy within the system. The theoretical effective force, F_{fold} , which drives the shortening of the fold is plotted in Figure 4.1.7 (e) against the individual tapering angle, θ , for single bi and tri-layer graphene. Similar to the advance of fracture 1 the elastic energy released by the shortening of the fold favours the growth of the ribbons and considering that the driving force, F_{fold} , remains constant at all lengths with constant tapering, this will result in a stable fracture.

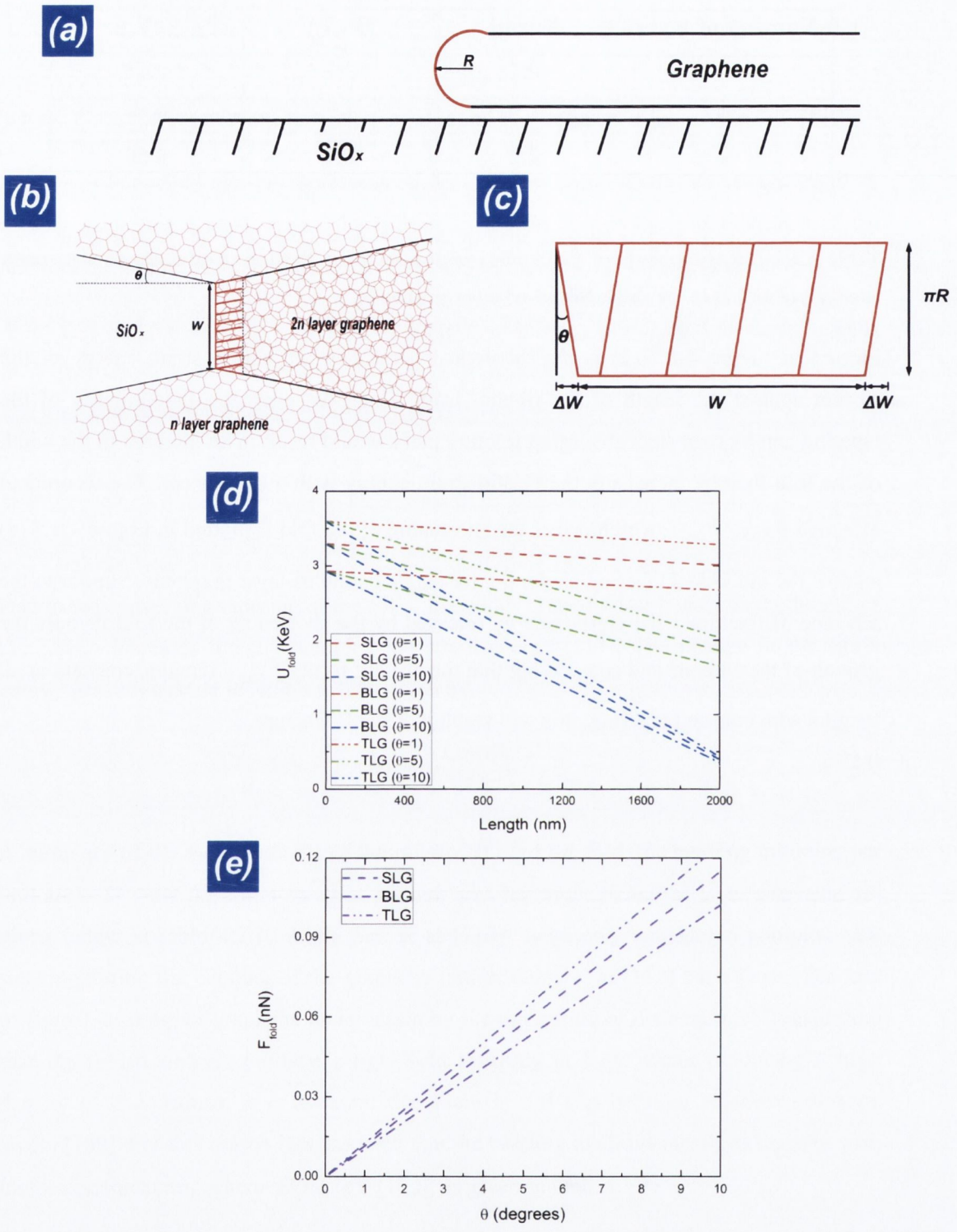

Figure 4.1.7: (a) schematic representation of the fold along the graphene sheet, (b) schematic representation of the geometry of the strained C-C bonds within the fold, (c) geometric representation of the area of the fold, (d) plot of the change in the energy of the system due to the reduction of the elastic energy within the fold against the length, (e) plot of the effective force due to the reduction of the elastic energy within the fold against the individual tapering angle, θ .

4.1.7 Fracture energy

The advance of the folded ribbons occurs by the fracture of the lattice along both sides of the fold, labelled fracture 2 within the schematic in Figure 4.1.2. An energy cost is associated with the advancement of fracture 2 due to the breaking of the C-C bonds along the lattice. A recent experimental study by Kim et al has verified that graphene tears preferentially along either zig-zag or armchair directions [40]. While the crystallographic orientation of the graphene lattices were not know during the course of the experiments it is concluded that the tearing could not be of purely zig-zag or armchair directions since most of the total tapering angles of the FR's did not reflect the 30^0 symmetry between the preferred directions. Detailed knowledge of the crystallographic orientation as well as the state of stress within the crack front is required to quantitatively determine both the direction and the cost of energy in fracturing the graphene lattice [113], however it is suggested that the fracture propagates by a combination of steps along the ZZ and AC directions and by taking values of 2.35eV/A and 2.19eV/A for the work of fracture, ΔE, along the ZZ and AC directions respectively [110], we establish a bimodal equation to represent the change of the energy of the system due to the fracture along the graphene lattice which is given by

$$U_{fracture} = \left\{ \begin{matrix} 2n\Delta E_{ZZ} \dfrac{L}{\cos(\theta)} \\ 2n\Delta E_{AC} \dfrac{L}{\cos(\theta)} \end{matrix} \right\} \tag{4.25}$$

The effective force opposing the growth of the ribbons, $F_{fracture}$, is then given by

$$\frac{dU_{fracture}}{dL} = F_{fracture}(\theta) = \left\{ \begin{matrix} \dfrac{2n\Delta E_{ZZ}}{\cos(\theta)} \\ \dfrac{2n\Delta E_{AC}}{\cos(\theta)} \end{matrix} \right\} \tag{4.26}$$

where n is the number of layers.

Shown below in Figure 4.1.8 is a plot of the change in the energy of the system due to the propagation of fracture 2 along both sides of the fold as given by equation (4.25). It is assume that the work of fracture remains constant provided that the tapering remains

constant and we estimate an effective force, $F_{fracture}$, opposing the motion growth of the folded ribbons of 7.4nN, 14.8nN and 22.2nN for single bi and tri-layer graphene respectively. The fracture along the graphene lattice is a purely atomic scale fracture and in the case of a single layer of graphene the crack front is terminated by a single C-C bond which is subject to the maximal stress and strain within the crack front as well as thermal fluctuations. We suggest that sub-critical fracture is possible, where thermal fluctuations provide sufficient energy to break the C-C bonds within the crack font thereby allowing subcritical growth of the fracture to occur. The complex state of stress within the crack front may result in dissimilar states of stress and strain on the C-C bonds at the leading edge of the crack [113]. One direction may be heavily favoured however the crystallographic orientation of the graphene sheets remained unknown during the course of the experiments which presents difficultly in determining the fracture path.

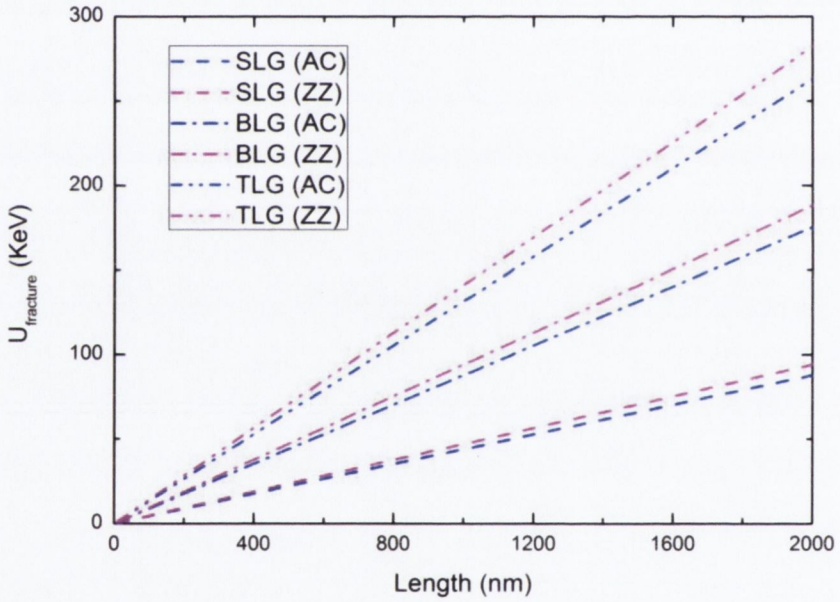

Figure 4.1.8: Plot of the change of energy of the system due to the advancement of fracture 2 against the length of the folded ribbons for single bi and tri-layer graphene along the ZZ and AC directions.

4.1.8 Total energy of the system

Similar to the Griffith analysis we obtain the total energy of the system by summing the surface energy, the work of fracture and the stored elastic energy as given by

$$U = U_{surface} + U_{fracture} + U_{fold} \tag{4.27}$$

A family of plots of the total energy of the system as a function of length for single, bi and tri-layer folded ribbons with individual tapering angles of 1^0, 5^0 and 10^0 is shown below in Figure 4.1.9. The analysis suggests that the growth of the ribbons is energetically favourable since the total energy of the system decreases with increasing length. It also suggests that the growth of the ribbons should not be unstable or be of runaway type since the total energy of the system always approaches a finite minimum value.

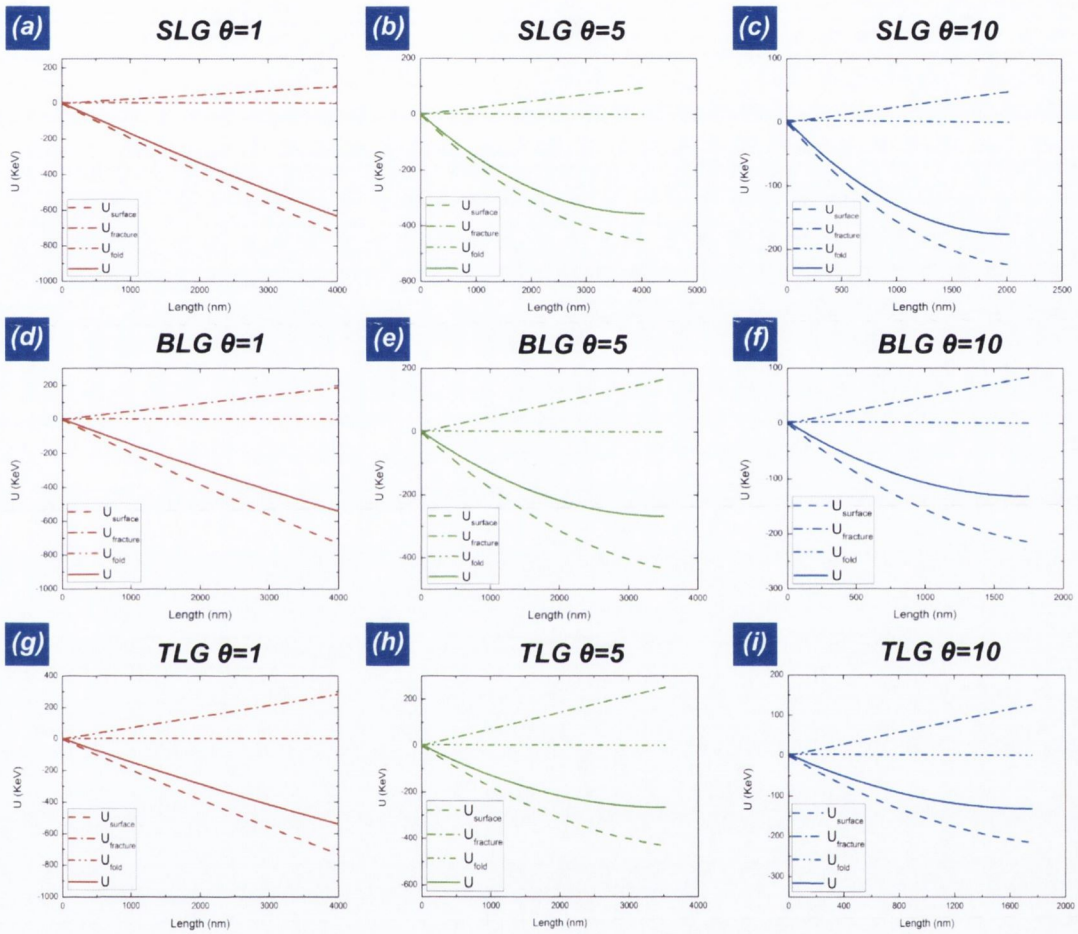

Figure 4.1.9: Summary of the surface, fracture, fold and total energies of single bi and tri-layer graphene for $\theta = 1^0$, 5^0 and 10^0 . (a), (b) and (c) plots of the energies vs length for SLG with $\theta = 1^0$, 5^0 and 10^0, (d), (e) and (f) plots of the energies vs length for B LG with $\theta = 1^0$, 5^0 and 10^0,(g), (h) and (i) plots of the energies vs length for TLG with $\theta = 1^0$, 5^0 and 10^0.

The energy release rate, for any given tapering angle, can be found by summing the instantaneous changes in the thermodynamic quantities, as given by

$$\left(\frac{\partial U}{\partial L}\right)_{\theta} = F_{surface} + F_{fold} + F_{fracture} \tag{4.28}$$

The nucleation event raises the total energy of the system by creating a free edge which is folded over creating two fracture paths. Once the nucleation event has occurred the growth of the ribbons can progress through a reduction of the total energy of the system if the energy released is larger than the work of fracture of the graphene lattice which is given by

$$-F_{fracture} > F_{fold} + F_{surface} \tag{4.29}$$

The system will be in equilibrium where

$$\frac{dU}{dL} = \left[W_0 - 2L\tan(\theta)\right]\gamma_{net} + \frac{\pi D\tan(\theta)}{2R} + \frac{2\Delta E_{ZZ/AC}}{\cos(\theta)} = 0 \tag{4.30}$$

This can be rearranged to solve for L in terms of θ , γ_{net} , D , $\Delta E_{ZZ/AC}$ and W_0 which is given by

$$L = \frac{\dfrac{\pi D\tan(\theta)}{2R} + \dfrac{2\Delta E_{ZZ/AC}}{\cos(\theta)} + W_0\gamma_{net}}{2\tan(\theta)\gamma_{net}} \tag{4.31}$$

By taking the average value of θ, W_0 and taking the literature values of D and $\Delta E_{ZZ/AC}$ the experimentally obtained values of the equilibrium length can be fitted to obtain a value of γ_{net} which was found to be 0.04J/m^2.

The direction of the fracture path and hence tapering angle of the ribbons is determined by the maximum energy release rate [98, 111] which is given by

$$\frac{d\left(\dfrac{\partial U}{\partial L}\right)}{d\theta} = 0 \tag{4.32}$$

By taking the derivative of equation (4.28) with respect to θ we obtain an expression for the maximum energy release rate given by

$$2n\Delta E_{ZZ/AC}\sec(\theta)\tan(\theta) + \frac{4\pi\tan^2(\theta)D}{2R} + 2L\tan^2(\theta)\left[\gamma_{net}\right] = 0 \tag{4.33}$$

and by rearranging we obtain

$$2n\Delta E_{ZZ/AC}\sec(\theta)\tan(\theta) = -\tan^2(\theta)\left(\frac{4\pi D}{2R} + 2L\left[\gamma_{net}\right]\right) \tag{4.34}$$

The maximum energy release rate can then be given in relation to θ by

$$\frac{1}{\sin(\theta)} = -\frac{\left(\frac{\pi D}{2R} + 2L\left[\gamma_{net}\right]\right)}{2n\Delta E_{ZZ/AC}} \tag{4.35}$$

This general expression suggests that the tapering angle may change as a function of length. It also suggests that the tapering angle will change according to the ratio of the parameters in the right hand side of equation (4.35). Since the work of fracture of the graphene lattice, ΔE , is anisotropic, with respect to the crack front the energies of the specific reactions involved in breaking the C-C bonds within the crack front remains undetermined and a clear analytical solution is not easily available.

4.1.9 Kinetics of growth

The initial growth of the folded ribbons remains largely unobserved since AFM has been used to measure the lengths of the ribbon as a function of time which introduces two large experimental constraints. The first is the time taken between the nucleation of the folded ribbon and the recording of the first image which is usually on the order of 30 minutes during which time most of the growth has already occurred. The second constraint is the time for an AFM to obtain an image which is usually on the order of 10 minutes which limits the measurements of the velocities of the folded ribbons however the AFM affords considerable advantages in spatial resolution. For this reason we focus mainly on the very slow subcritical growth which occurs over long periods of time of approximately 24 hours and slow velocities of nm/min. The very slow growth rates over long periods are indicative of a subcritical thermally activated process which can be understood in terms of rate theory where an energy barrier, ε_f , opposes the motion of the folded ribbon and an energy barrier, ε_r, opposes the motion of the folded ribbon in the healing direction. It is suggested that there are two sources which act together to provide the collective energy barrier. The first is the potential corrugation due to the sliding of the contacting surfaces and the second is the activation energy required to break the C-C bond. The folded ribbons typically grow rapidly at the beginning of the growth which transitions sharply into a much slower growth regime. This sharp transition indicates that the initial and later growth rates are limited by

different processes. We suggest that the initial large growth rate is due to the relatively large energy release rates however as the folded ribbon grows the thermodynamic quantities which drive the growth diminish which then transitions into a much slower sub critical regime. During the subcritical regime we represent the velocity of the growth by

$$v = v_0 \left[\exp^{-\left(\frac{\varepsilon_f}{k_B T}\right)} + \exp^{-\left(\frac{\varepsilon_r}{k_B T}\right)} \right] \tag{4.36}$$

For the purpose of the analysis in this thesis, it is assumed that $\varepsilon_r >> k_B T$ because any step in the healing direction requires an increase in energy approximately equal to the product of the atomic step size (a_0) and the width (W). By taking a minimum value of the width to be 100nm and the step size to be 0.14nm the change in energy will then be given by

$$a_0 W \gamma_{net} \approx 5eV \tag{4.37}$$

It is therefore assumed that the trapped state during the thermally activated transition is stable at room temperature, where $k_B T$ =0.025eV. The rate in the forward direction is limited by the two C-C bonds at each side of the crack front. The forces driving the growth, $F_{surface}$ and F_{fold} lower the intrinsic energy barrier required for the growth to proceed resulting in growth rates in the order of nm/min. The transition from the growth rate of nm/min to the eventual equilibrium of the folded ribbons remains unknown, due to limitations of the spatial resolution of the AFM, and this remains a research objective for future work.

Adopting this assumption the velocity can then be written in terms of the length as a function of time by

$$\frac{dL}{dt} = v_0 \exp^{-\left(\frac{\varepsilon_f}{k_B T}\right)} \tag{4.38}$$

where t is time.

Since the growth typically decays with length we represent the collective energy barrier as a function of the length of the ribbon $\varepsilon_f(L)$ and we assume a linear decay since $F_{surface}$ decreases linearly with length and $F_{fracture}$ and F_{fold} remain constant with a constant tapering angle. We then represent the collective energy barrier by

$$\varepsilon_f(L) = \varepsilon_i + \alpha L \tag{4.39}$$

where ε_i is the initial energy barrier at the beginning of the subcritical growth, and α is a constant.

The length of the ribbon can then be found as a function of time by integrating with respect to L and t which is given by

$$\int \exp^{\left(\frac{\alpha L}{k_B T}\right)} dL = v_0 \exp^{\left(\frac{\varepsilon_i}{k_B T}\right)} \int dt \tag{4.40}$$

This integration yields

$$\frac{k_B T}{\alpha} \exp^{\left(\frac{\alpha L}{k_B T}\right)} = t v_0 \exp^{\left(\frac{\varepsilon_i}{k_B T}\right)} + c \tag{4.41}$$

where c is a constant of integration.

At the initial point of the subcritical growth, where $t = 0$, the length of the folded ribbon is given by L_i, and by applying these boundary conditions and rearranging equation (4.41) we obtain

$$c = \frac{k_B T}{\alpha} \exp^{\left(\frac{\alpha L_i}{k_B T}\right)} \tag{4.42}$$

By combining and rearranging equations (4.42) and (4.41) we obtain an expression for the change in the length, ΔL as a function of the time for the subcritical growth of the folded ribbons which is given by

$$\frac{k_B T}{\alpha} \exp^{\left(\frac{\alpha \Delta L}{k_B T}\right)} = t v_0 \exp^{\left(\frac{\varepsilon_i}{k_B T}\right)} \tag{4.43}$$

Taking the natural logarithm of both sides of equation (4.43) yields

$$\Delta L = \frac{k_B T}{\alpha} \ln[t] + c_0 \tag{4.44}$$

where c_0 is a constant given by

$$c_0 = \frac{k_B T}{\alpha} \left(\ln\left[\frac{\alpha v_0}{k_B T} \right] + \frac{\varepsilon_i}{k_B T} \right) \tag{4.45}$$

The analysis of the subcritical growth suggests that the growth rate will exponentially decay with time for a linear increase in the collective energy barrier opposing the growth of the ribbon. This exponential decay will only apply in the absence of any abrupt changes in the energy barrier which may be introduced by a physical barrier or in the presence of a pinning defect.

4.2 Experimental Details

Graphene flakes were exfoliated by mechanical means, from kish graphite (graphene supermarket), through the use of scotch tape and deposited onto silicon chips with 300 +/- 5nm amorphous oxide. The thinnest flakes were then selected for nanoindentation via optical microscopy (Zeis Axio Imager) and the silicon chips were mounted in the 3D nanoindenter (Fast Forward Devices). Indentation was performed with a Berkovich tip using a constant strain rate to a maximal load of 3mN. Throughout the indentation a lateral oscillation of between 2 and 5nm was superimposed, similarly to the experimental procedure described in chapter 2. While the orientation of the Berkovich tip remained constant with respect to the direction of the lateral oscillation the orientation of the graphene lattice remained random. The residual impression was imaged via tapping mode AFM (Asylum MPF3D), using standard silicon taping mode AFM tips and was monitored until the growth had ceased. Raman spectroscopy (WiTec alpha 300R) was then performed to characterise the thickness, the quality of the graphene and to determine the stacking order between the ribbon and the underlying flake. Thermal treatment of the samples was performed in an oven by preheating the over to the required temperature and depositing the samples within resulting in a rapid thermal treatment or by depositing the sample within the oven at room temperature and slowly increasing the temperature.

4.3 Results and Discussion

4.3.1 Growth and Characterisation

The typical residual impression produced by Berkovich nanoindentation into a mechanically exfoliated bi-layer graphene flake on an SiO_x substrate is shown by the tapping mode AFM image in Figure 4.3.1 which was recorded approximately 30 minutes after the indentation. The 60nm deep pyramidal impression, defined by three sharp edges is typical of the plastic deformation associated with indentation into an amorphous flat surface, as discussed in chapter 3. The deformation of the covering graphene layer is clearly distinguishable from the deformation of the substrate and has several striking features. The graphene sheet has been complete pierced and no evidence of it remains inside the indentation impression. Decorating the two lower edges of the triangular impression are folded over and wrinkled up sections of graphene which retain a single, distinct long fold parallel to the indentation edge. The pattern of graphene at the top edge of the impression is entirely different. No graphene is present there, but instead a long, approximately $1\mu m$ in length, inward tapering piece of graphene has been removed revealing the SiO_x substrate below. Above this, the mirror-image of this piece is found, revealing the torn graphene strip lying in conformal contact with the top of the underlying graphene flake. The leading edge of this ribbon shows a wrinkle-like formation resembling those on the other sides of the impression, while the bottom appears still attached to the lower graphene flake with a long, uniform fold like structure. The formation of the folded ribbon like structure is difficult to explain in terms of the indentation procedure since the maximal lateral motion of the tip was 2nm. The topography of the folded graphene ribbon shows that the ribbon lies in very close conformal contact with the underlying flake as demonstrated by the height profiles in Figure 4.3.1 (b). As a result of the conformal contact a very tight fold or tube like structure is produced which results in a small volume of highly strained carbon bonds. The tapering remains approximately constant with a slight increase nearer the fold however we measure the local tapering angle on hand side to be 9.9 degrees and 6.8 degrees on the right hand side and which results in a total tapering value of 15.7 degrees which is shown in Figure 4.3.1 (b).

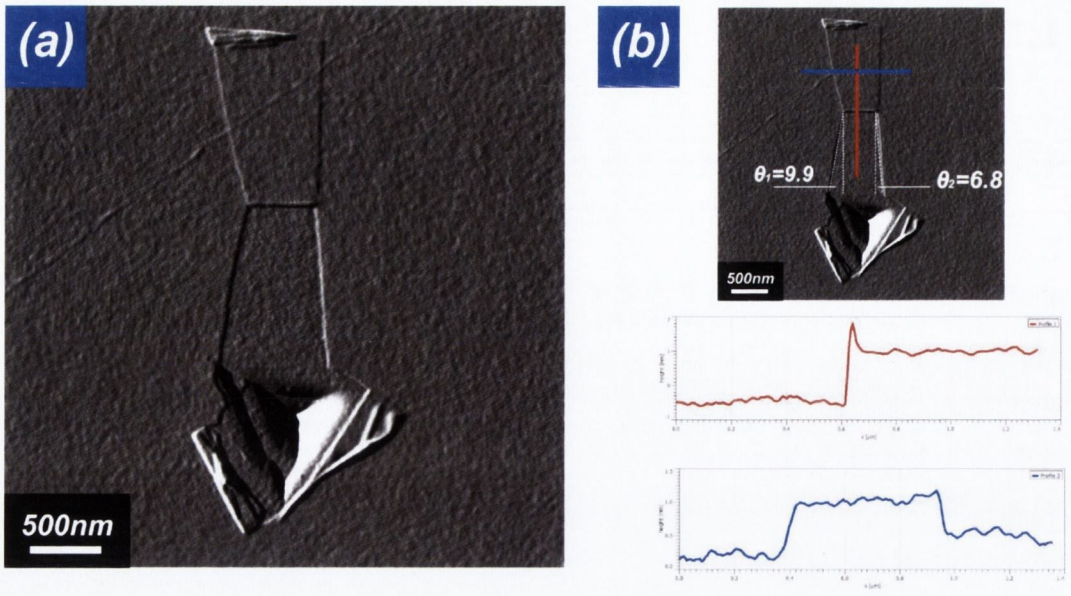

Figure 4.3.1: (a) Tapping mode height AFM image of the residual impression of an indentation into BLG/SiO_2 surface and (b) with height profiles indicated by the red and blue lines.

The series of tapping mode AFM images shown in Figure 4.3.2 (a-c) demonstrates the growth of two folded ribbons at room temperature (21^0C) and ambient atmospheric conditions on a bilayer graphene flake. The first image in the series was recorded approximately 30 minutes after the indentation was performed, which we define as a reference image from which we measure the change in the folded structures surrounding the impression. The second and third images in the series were recorded 4.2 hours and 4 days, respectively, after the initial image during which time we can see that the folded ribbon on the top of the impression grew by approximately $150nm$ however we can also see the emergence of a new folded ribbon on the lower left hand side of the impression which grew away from the impression by approximately 1μm.

Figure 4.3.2 (c-e) shows the effect of locally heating static ribbons by focused laser illumination with a power of 30mW focused on a spot size of approximately 1μm, using the WiTec Raman spectrometer. Considerable growth on both of the established folded ribbons on the upper and lower left hand sides of the impression can be seen however a third folded ribbon was nucleated on the right hand side of the impression by creating a second fracture path on the lower side of the fold. This allowed the third folded ribbon to emerge and grow away from the indentation site in a similar way to the other two folded ribbons. The robustness of the growth can be seen in particular in Figure 4.3.2 (c-d) since the growth of the folded ribbon on the lower left hand side did not seem to be inhibited by the relatively large defect. While it is not clear what the defect is it resembles a sub surface

defect and we assume that it is the result of some trapped gas or liquid between the graphene and the SiO_x surfaces [114]. Any subsurface defect may result in an energetic barrier to the growth since elastic deformation of the ribbon is required to surpass the defect however the interface between the ribbon and the underlying flake remains unchanged. The total tapering angles, ϕ, of the ribbons shown in Figure 4.3.2 did not reflect the symmetry of the graphene lattice and we suggest that the fracture paths are composed of a combination of both ZZ and AC directions. The direction of the growth appeared to have been maintained throughout the growth on all three of the folded ribbons with a 60^0 symmetry between them, shown in Figure 4.3.2 (f). We suggest that the reason for the conserved direction of growth is due to equal fracture rates on both sides of the fold.

All three of the folded ribbons ceased to grow beyond the dimensions shown in Figure 4.3.2 (e). No clear visible reason for the stalling of the growth of the folded ribbons on the upper and lower left hand sides of the impression can be seen by the AFM images however the folded ribbon on the right hand side of the impression failed to grow beyond the edge of the graphene flake. We suggest that the growth of the folded ribbons on the upper and lower left hand side of the impression stalled due to the diminishing thermodynamic quantities which drive the growth however the growth of the folded ribbon on the lower right hand side of the impression ceased to grow beyond the edge of the graphene sheet.

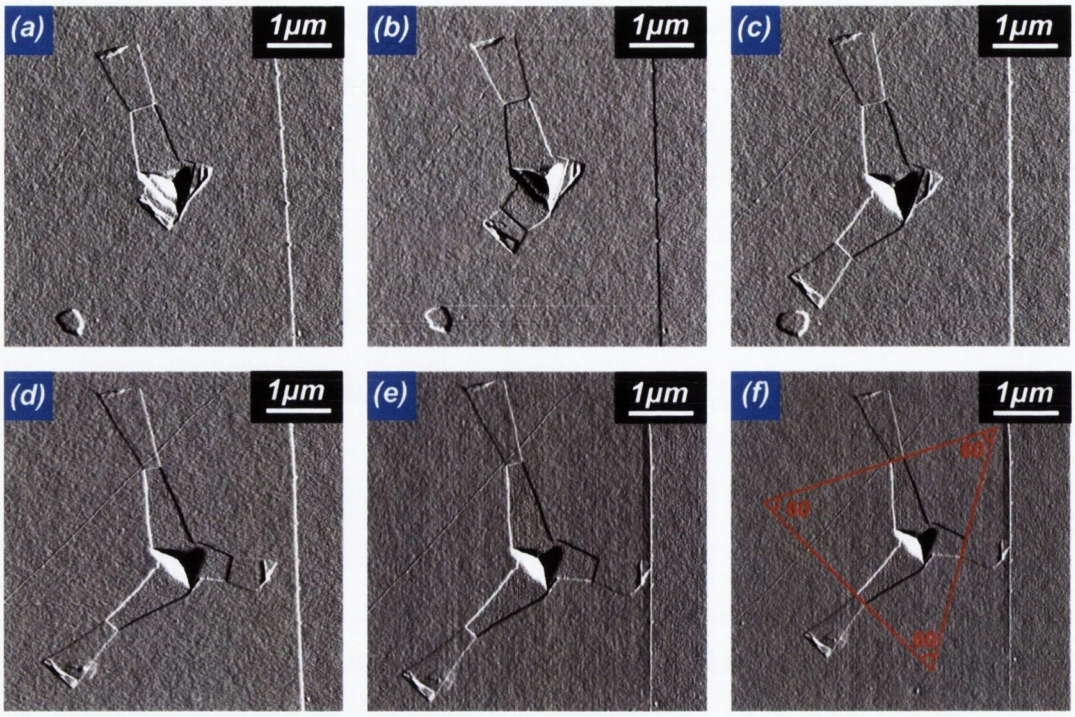

Figure 4.3.2: Example of the growth of folded ribbons on a bi-layer graphene flake. (a) Reference tapping mode AFM image recorded approximately 30 minutes after indentation where t=0, (b) AFM image recorded t=4.2 hours, (c) AFM image recorded at t=4 days, (d) AFM image recorded at t=15 days after laser irradiation, (e) AFM recorded at t=36 days and (f) AFM image demonstrating the 60^0 symmetry of the fold line.

Shown below in Figure 4.3.3 (a) is an AFM image of a folded ribbon produced on a single layer graphene flake with a small tapering angle of approximately 3^0. The growth of the folded ribbon with such small tapering provides confirmation that the interfacial fracture 1 is energetically favourable since any relaxation of the stored elastic energy within the fold is effectively negligible with such low tapering. The orientation of the graphene lattice was not known during the experiment however we suggest that the low tapering angle may be a result of the lattice being predominantly fractured along an easy ZZ or AC direction. The local tapering on the left hand side was measured to be 14.4 degrees and -9.8 on the right hand side of the folded ribbon. This large asymmetry may be due to different fracture rates between the two different paths along the lattice which results in a rotation of the direction of growth.

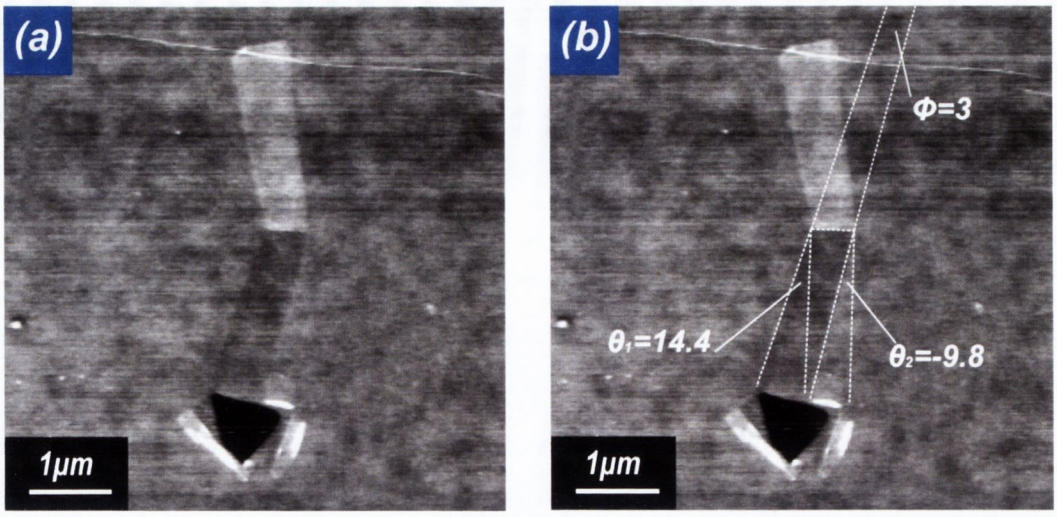

Figure 4.3.3: Tapping mode AFM height images of (a) a folded ribbon produced on single layer of graphene, (b) the folded ribbon with the local and total tapering angles shown.

The characterisation of 36 folded ribbons (10 SLG, 19 BLG, 7 TLG), which were nucleated with identical nanoindentation tests, are summarised by the four plots in Figure 4.3.4. The measurements of the total tapering angles (ϕ) are shown in Figure 4.3.4 (a). The average value of the total tapering angles decreased with increasing thickness of graphene. This may be due to an increase in the stored elastic energy within the fold with increasing thickness which results in an increase in the numerator of equation (4.35). A large amount of scatter in the total tapering angles of the ribbons produced on single layer graphene was found, ranging between 3^0 and 33^0. This may be due to the 30^0 symmetry between the easy tearing along the ZZ and AC directions. The total tapering angels appear to be randomly distributed between the maximum and minimum which indicates that the process may be nucleated along any crystallographic orientation. The scatter in the total tapering angle decreased with increasing thickness which may be due to discrete bond breaking processes which are suppressed with increasing thickness due to the increased complexity of the fracture process with increasing thickness. The measurements of the local tapering angles (θ), shown in Figure 4.3.4 (b), illustrate a similar dependence to the measurements of the total tapering angles with an increase in the scatter of the ribbons produced on single layer graphene, which range from -14^0 to 23^0. Similar to the total tapering angles, a decrease in the local tapering angles is found with increasing thickness. Only negative values of the local taper angles were found on single layer ribbons which may be due to different fracture rates along the graphene lattice which is suppressed in thicker graphene flakes due to the increased complexity of the fracture process. The measurements of the final lengths of the folded ribbons show no clear trend, Figure 4.3.4 (c). This may be dependent upon the scatter in the tapering angles or initial widths or on some environmental variation in the

stopping conditions, for example density of pinning points. The final widths of the folded ribbons (Figure 4.3.4 (d)) suggest that there is a threshold below which growth is no longer favourable which may be due to the diminishing driving force, $F_{surface}$. The application of the model, outlined in the introduction, is shown by the blue data points connected by the broken line. The average values of the tapering angle were determined from the empirical data. The equilibrium length for the given values of θ , D , R , $\Delta E_{ZZ/AC}$ and W_0 =800nm were determined using equation (4.31) and a least squares fit was used to obtain a value of γ_{net} =0.04J/m^2.

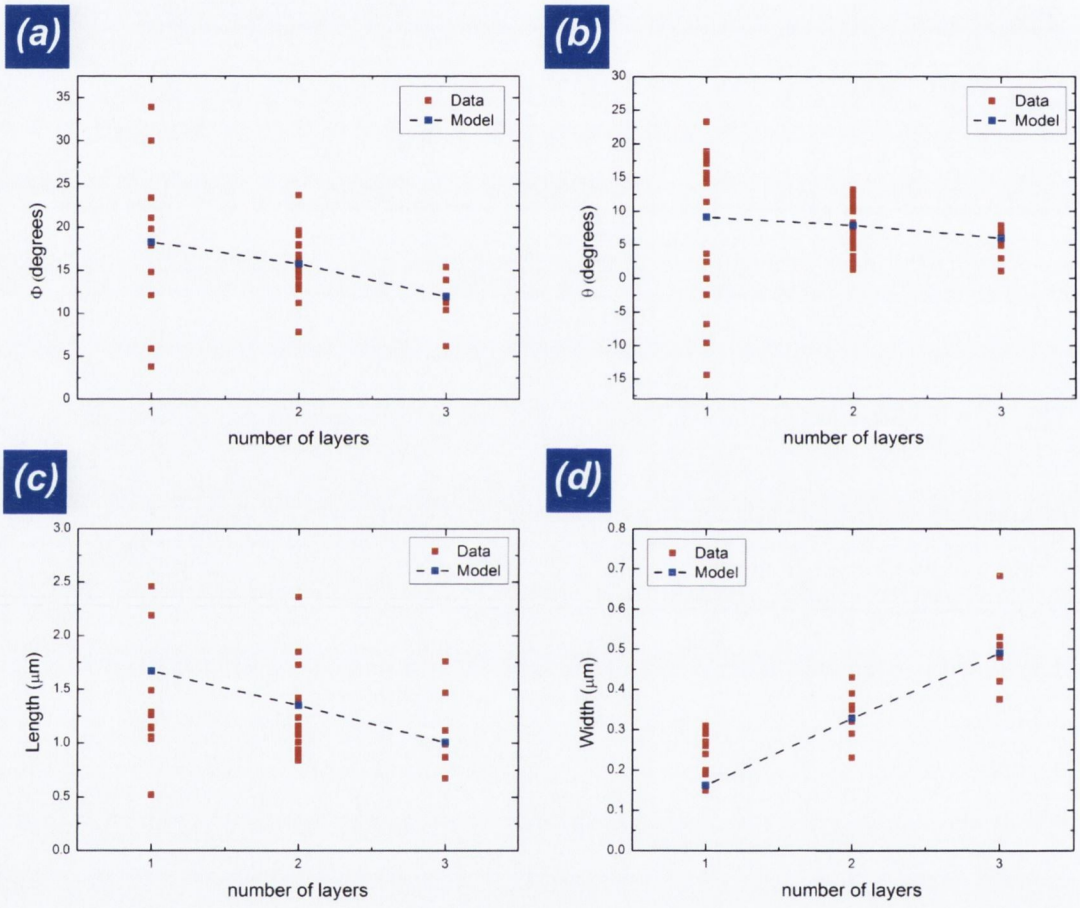

Figure 4.3.4: Summary of the geometric characterisation of 36 folded ribbons, shown by the red data points, and the application of the model, shown by the blue data points. (a) plot of the total tapering angle vs number of layers, (b) individual tapering angles vs number of layers, (c) final length vs number of layers and (d) final width vs number of layers.

4.3.2 Kinetics of growth

An example of the spontaneous growth of a folded ribbon is shown below by the series of images in Figure 4.3.5 (a-d). The first image in the series was recorded approximately 30 minutes after the indentation from which we can see an established folded ribbon on the upper side of the indentation with familiar bunching at the periphery of the contact on the lower and left hand sides of the impression. The second image in the series illustrates the rapid and spontaneous growth of a second folded ribbon on the lower side of the impression, which appears to have been nucleated by tip sample interaction as the AFM tip scanned across the folded structure. The initial rapid growth rate resulted in approximately 2.1μm of growth in the first 7 minutes followed by approximately 350nm of growth in the following hours. This sharp variation is difficult to understand in terms of the thermodynamic quantities which scale with the dimensions of the folded ribbon. This suggests that the initial growth rate is limited by a different physical process. We suggest that the initial fast growth rate is a result of the relatively large energy release rate the velocity of which is limited by the dissipation of energy between sliding interface of the ribbon and the underlying flake. After the initial rapid growth rate the velocity significantly diminishes due to the diminishing thermodynamic quantities which results in a very slow growth rate of nms/min which is indicative of a thermally activated sub critical fracture process where we suggest that the velocity is limited by the rate of breaking the C-C bonds within the crack front.

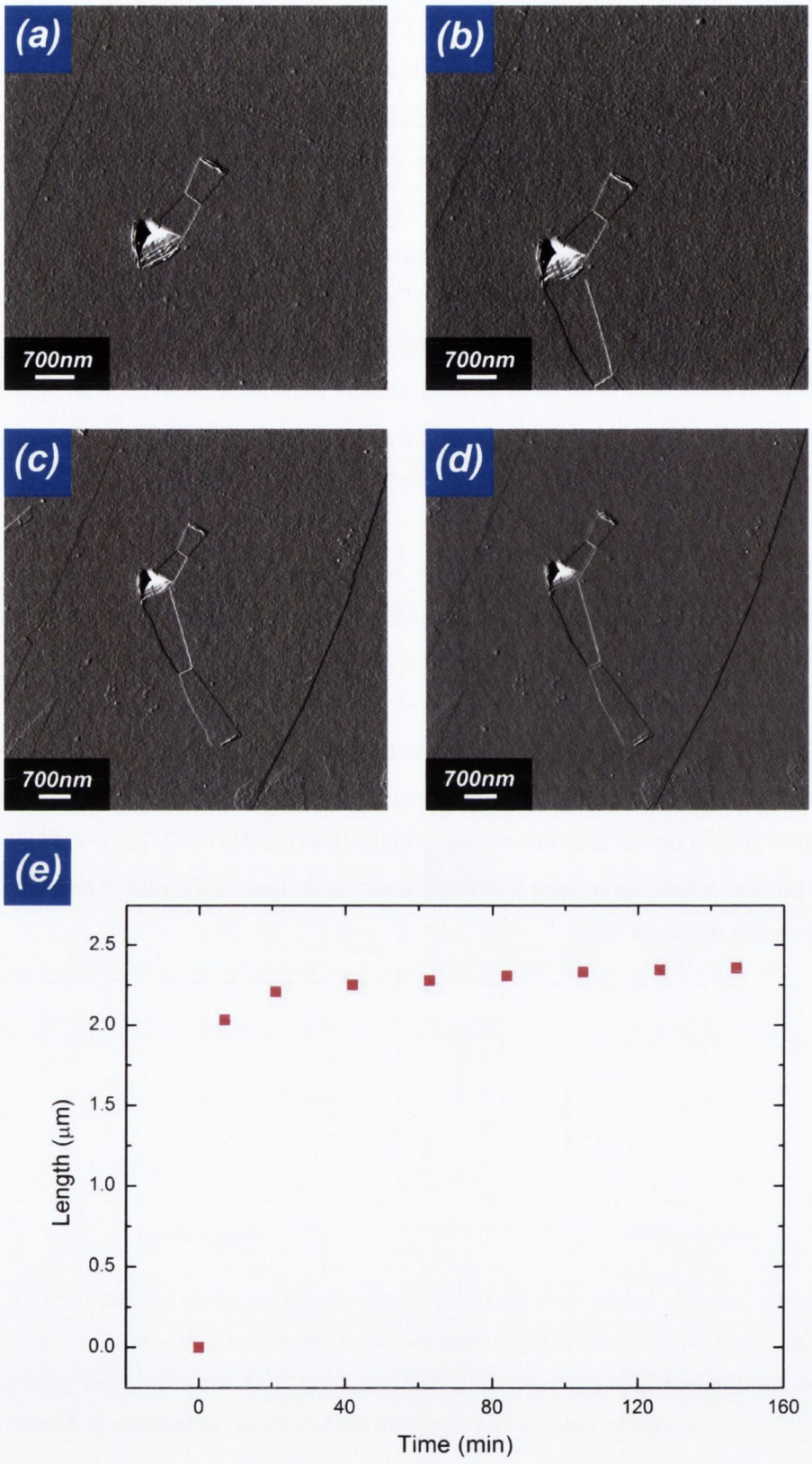

Figure 4.3.5: (a) Reference tapping mode AFM image recorded approximately 30 minutes after indentation, (b) AFM image recorded at t=21 minutes from which we can see the spontaneous growth of a folded ribbon (c) AFM image recorded at t=42 minutes, (d) AFM image taken at t=4 hours and (e) plot of the length of the folded ribbons against time.

In contrast to the rapid growth of the folded ribbon shown in Figure 4.3.5 the series of AFM images given in Figure 4.3.6 (a-d) illustrates the intermittent growth of a folded ribbon in the presence of a defect which hindered the growth. The initial location of the defect can be seen in Figure 4.3.6 (a) at the leading edge of the ribbon. The AFM image revealed a variety of defects however during the growth only one of the defects changed location and appeared to hinder the growth of the folded ribbon. It is assumed that the other defects were located between the SiO_x and the graphene interface. No growth of the ribbon was observed during the initial course of AFM scanning, which is shown by the plot of the length against time in Figure 4.3.6 (e). After 22 AFM scans, approximately 4 hours of AFM scanning, the defect at the leading edge shifted to the lower side of the leading edge which can be seen in Figure 4.3.6 (b), which allowed for approximately 200nm of growth and a relative rotation of the ribbon. The ribbon remained stationary during another 20 AFM scans, 4 hours of scanning, until the defect moved again which allowed the ribbon to grow by a further 300nm. The stochastic nature of the growth can be seen from the plot of the length of the ribbon against time in Figure 4.3.6 (e).

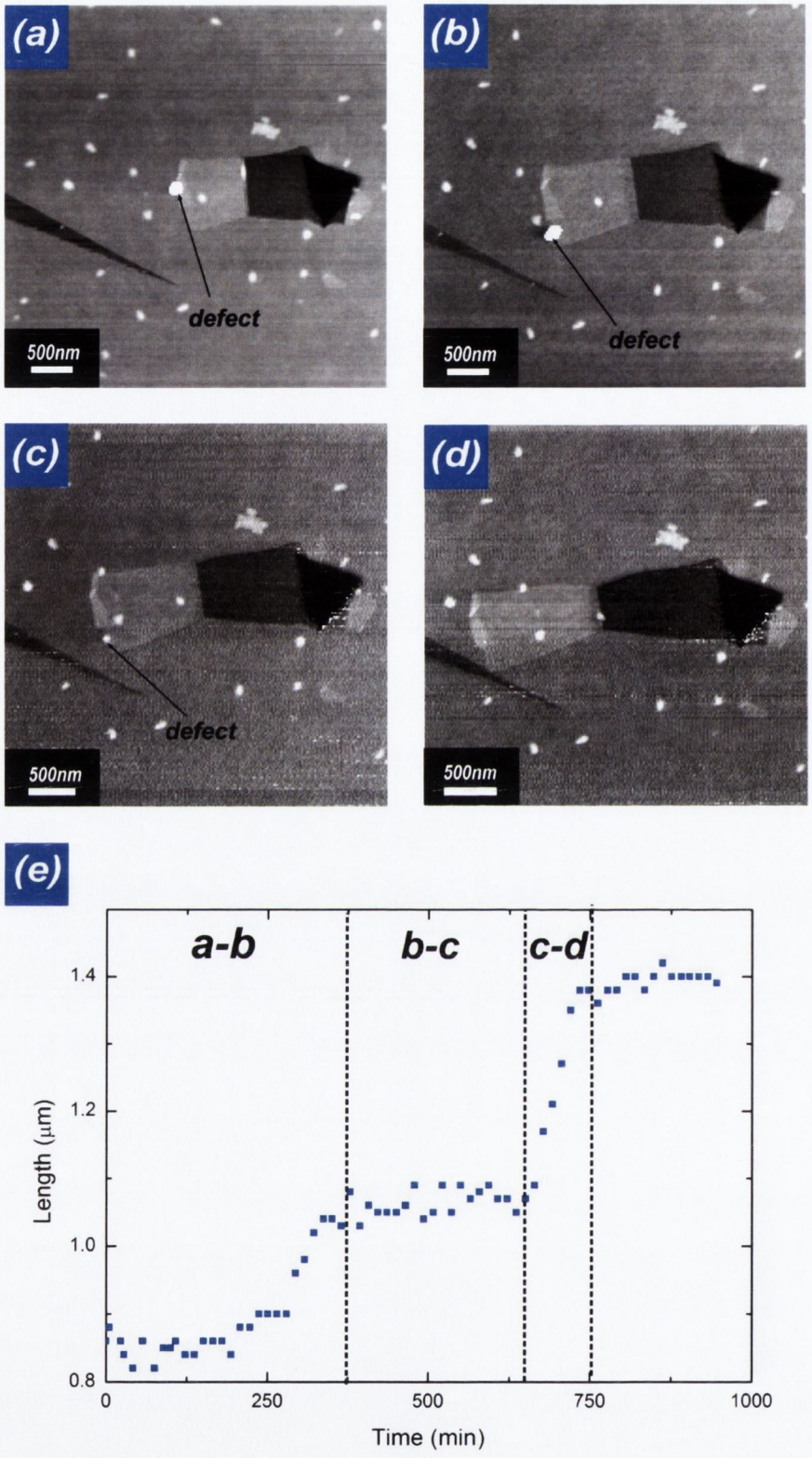

Figure 4.3.6: An example of the growth of a bi-layer folded ribbon in the presence of a defect. (a) the first tapping mode AFM image recoded at t=0, (b) AFM image recorded at approximately t=6 hours after the motion of the defect and ribbon, (c) AFM image recorded at approximately t=8hours before the final motion of the defect, (d) final image in the series recorded at t=15 hours and (d) plot of the length of the ribbon vs time.

The growth of nine folded ribbons is shown below in Figure 4.3.7 (a), where $t=0$ is defined as the time when the indentation and hence nucleation occurred. The measurements of the initial growth rates are obscured by the time taken between the indentation and the recording of the first image. It can be seen that the growth rates of the folded ribbons do not scale with the area of the folded ribbons. The initial growth rate appears to be rapid for all of the folded ribbons which sharply transitions into a much slower subcritical growth rate similar to the example shown in Figure 4.3.5. Some of the folded ribbons have exhibited intermittent, stochastic growth which is due to the presence of pinning points or defects. Shown below in Figure 4.3.7 (b) is a plot of the change of length, ΔL , against the natural logarithm of time, which appears to be linear in the absence of any intermittent growth. This stands in good agreement with the analysis in the introduction since the effective thermodynamic force driving the growth of the folded ribbons decreases linearly with the length. A linear plot of the change in length of the folded ribbons against the natural logarithm of time is therefore expected, as given by equation (4.44), for a thermally activated process.

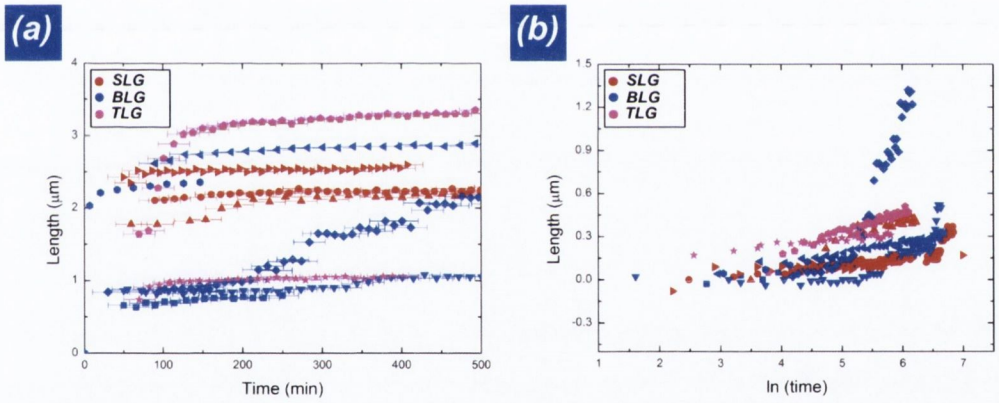

Figure 4.3.7: Summary of the measurements of the room temperature kinetics of a set of folded ribbons. (a) Plot of the length of the folded ribbons against time, where t=0 is the time of the indentation, (b) plot of the change in the length of the folded ribbon against the natural logarithm of time.

4.3.3 Thermal treatment and Self Assembly

Shown below in Figure 4.3.8 (a) and (b) are plots of the thermal history of a set of folded ribbons which were stable at room temperature. The change in length of the ribbons with increasing temperature can be attributed to a either an increase in the thermal energy of the fluctuations which allow the growth to progress or an additional stress due to a mismatch between the thermal expansion coefficients of graphene and SiO_x. The plot of the change

in length against number of layers is shown below in Figure 4.3.8 (c) from which we can see larger growth of ribbons which were treated under the rapid temperature increase, shown in green, in comparison to the slower thermal treatment, shown in red. The smaller average growth of the slower temperature increase is not likely to be due to additional thermal energy at higher temperatures since the slowly treated samples were held at higher temperatures for longer. We suggest that the rapid thermal treatment of the ribbons introduces a state of stress within the flake, due to a mismatch between the thermal expansion coefficients of the SiO_x and the graphene, which gets concentrated in the two crack fronts allowing the fracture to progress.

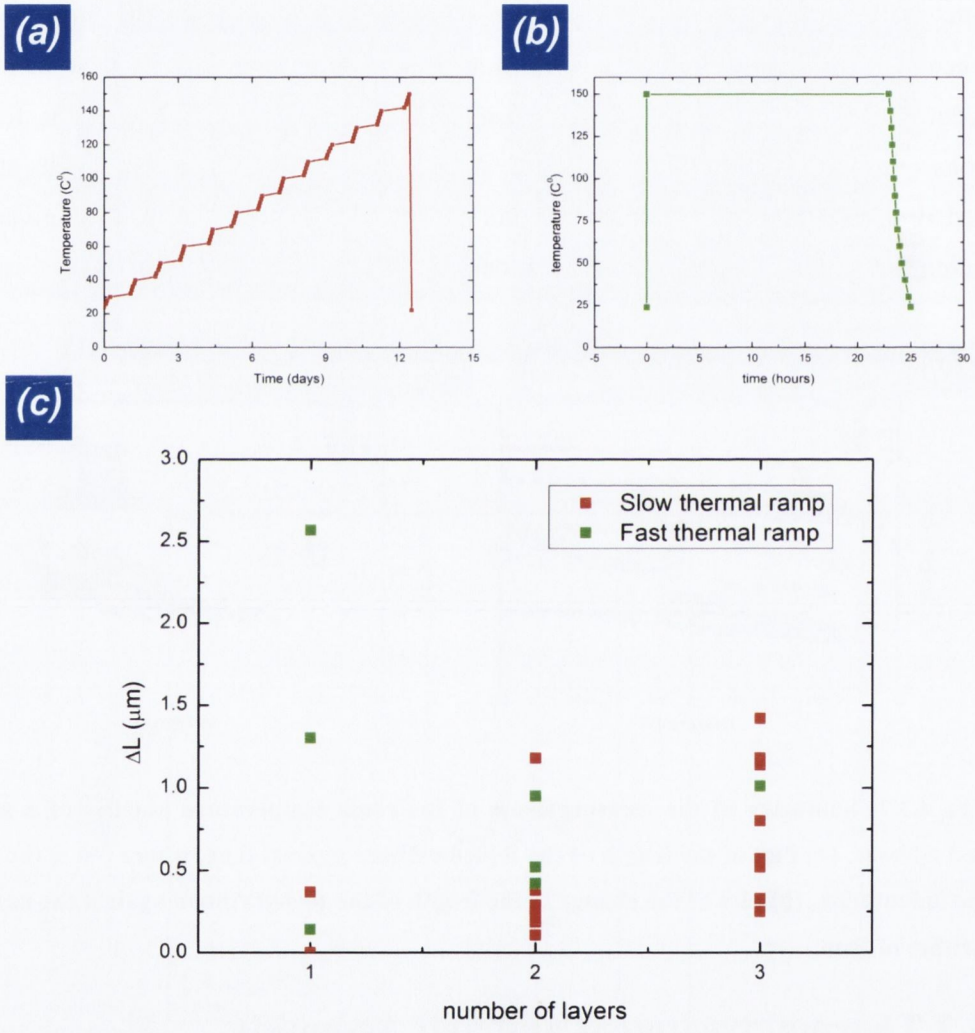

Figure 4.3.8: The thermal history of a set of folded ribbons for (a) the slow thermal treatment, (b) the fast thermal treatment and (c) the change in the length due to the fast and slow thermal treatments shown in green and red respectively.

Shown below in Figure 4.3.9 (a) and (b) is an example of a folded ribbon produced on a single layer of graphene which was thermally treated with previously described the slow rate, which enabled the ribbon to grow by approximately 370 nm. While observation of

the growth was not possible during the thermal treatment we suggest that the growth occurred slowly throughout the entire thermal treatment by the successive dissociation of C-C bonds along the crack fronts. While the increased temperature appears to have modified the fracture path of the ribbon the tapering remained typical since the fracture paths remained converging and not diverging. Shown in Figure 4.3.9 (c) and (d) are AFM images of a folded ribbon produced on a single layer flake before and after the rapid thermal treatment which enabled 2.6μm of growth. The rapid thermal treatment also resulted in diverging fracture paths however no diverging fracture paths resulted from the slow thermal treatment.

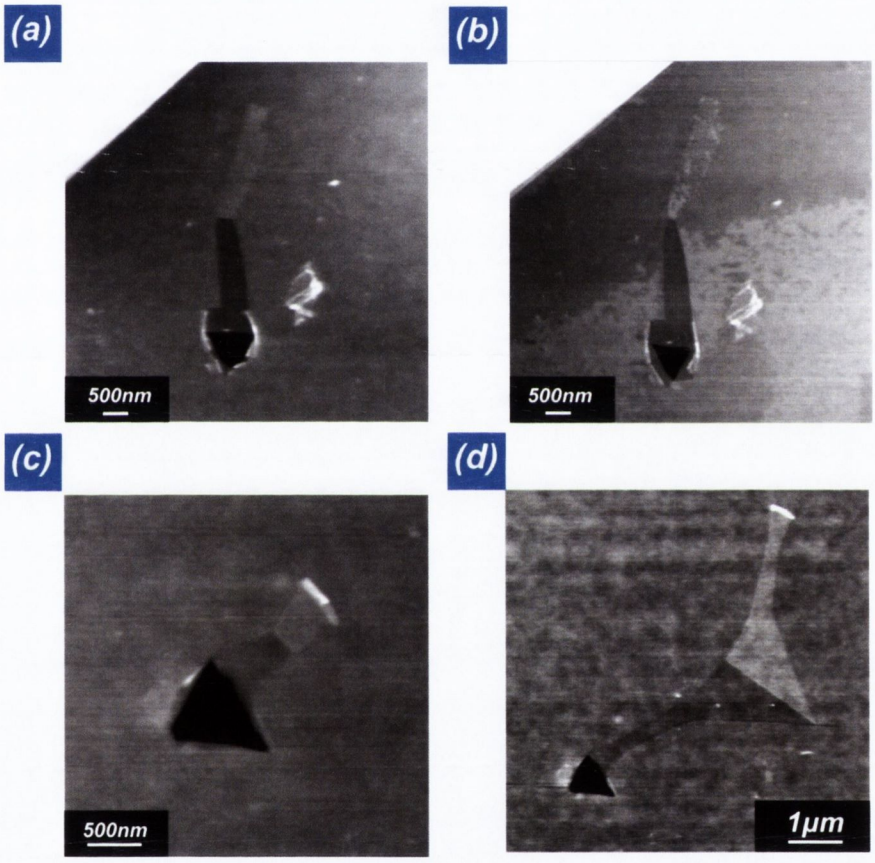

Figure 4.3.9: Tapping mode AFM height images of folded ribbons on single layers of graphene (a) before the slow thermal treatment, (b) after the slow thermal treatment, (c) before the fast thermal treatment and (d) after the fast thermal treatment.

An example of the spontaneous formation of a large folded structure on a single layer of graphene is shown by the optical images before and after the thermal treatment in Figure 4.3.10 (a-b). While no direct observation of the formation of the large fold was made during the thermal treatment a plausible mechanism is suggested that may account for the folded structure which is outlined in the series of schematic images in Figure 4.3.10 (c-f). At some time during the thermal treatment, most likely at higher temperature, the edge of the graphene sheet spontaneously folded over. It is assumed that this was formed at the point of highest curvature since a flipping a straight edge is prohibited by the relatively large amount of elastic energy required however folding a point of high concave curvature requires considerably less elastic energy. Through successive thermal fluctuations the fold grew towards the centre of the flake Figure 4.3.10 (d-e). Each successive step of the growth results in a small increase in the length of the fold which results in a small increase in the elastic strain energy within the system however each successive step also results in a relatively large change in the area of the folded structure, due to the large length of the fold, which results in a relatively large decrease in the total energy of the system. At some time during the growth a fracture path was nucleated, which may have been due to the presence of a defect along the edge of the flake. It is suggested that the growth continued until the point of inflection where the curvature of the edge of the sheet changes after which it appears that any increment of the change in the area of the fold results in a very large change in the length of the fold line therefore results in a large increase in the elastic strain energy.

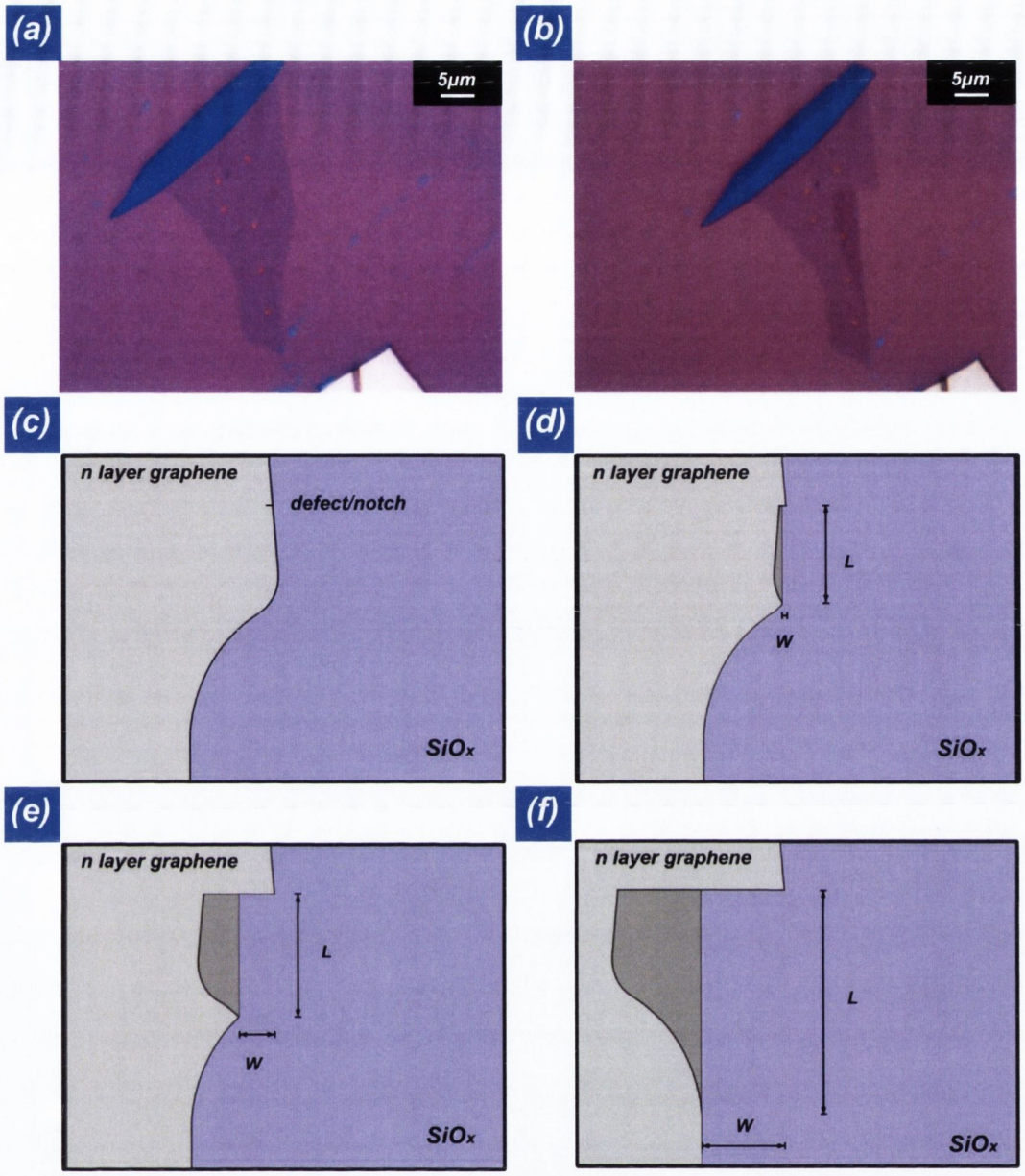

Figure 4.3.10: Example of the dewetting of a single layer of graphene on SiO_x substrate. (a) Optical image before the thermal treatment, (b) optical image after the thermal treatment showing the formation of a large folded structure, (c-f) schematic representation of the purposed method of formation.

Shown below in Figure 4.3.11 is a selection of folded ribbons which have interacted with external boundaries at high temperatures of 200^0C. Figure 4.3.11 (a) and (b) are two examples of FR's which interacted with the edge of the graphene flake. The first example, Figure 4.3.11 (a), is of a bi-layer folded ribbon which approached the edge of the flake at an angle of approximately 35^0 however instead of stalling the growth the ribbon continued to grow parallel to the edge of the flake. This demonstrates the sensitivity and the affinity of the graphene/graphene interactions in comparison to the graphene/SiO_x interactions. Only the leading edge was introduced to the boundary of the graphene edge however this was sufficient to alter the direction of the growth. The second example shown in Figure 4.3.11 (b) is of a bi-layer folded ribbon which approached the edge at a perpendicular angle which also illustrates the extreme sensitivity and affinity of the graphene/graphene interactions. The steep angle ensured that the folded ribbon could not continue to grow away from the impression in the conventional manner however the ribbon continued to grow in a doubly folded configuration. The subsequent images in Figure 4.3.11 are examples of folded ribbons which interacted with one another. Shown in Figure 4.3.11 (c) is an AFM image of three folded ribbons which converged causing them to grow over one another and eventually split. The last AFM image, Figure 4.3.11 (d) is of two folded ribbons, produced on a bi-layer flake, which grew into one another which caused the ribbon on the left to rotate. These examples illustrate the affinity of the graphene/graphene interactions in comparison to the graphene/SiO_x interactions. The examples also demonstrate the unique wetting like properties of the assembly process where low energy configurations are sampled by thermal energy eventually finding the lowest energy configuration. The superlubricity between the ribbon and the underlying flake coupled with the strong in plane C-C bonds result in unique sensitivity to external boundaries where weak Van der Waals interactions, on an atomic scale, result in a collective behaviour over the entire ribbon with a μm length scale. The examples also demonstrate the capability of forming complex folded structures which may prove to be useful as a self assembly process.

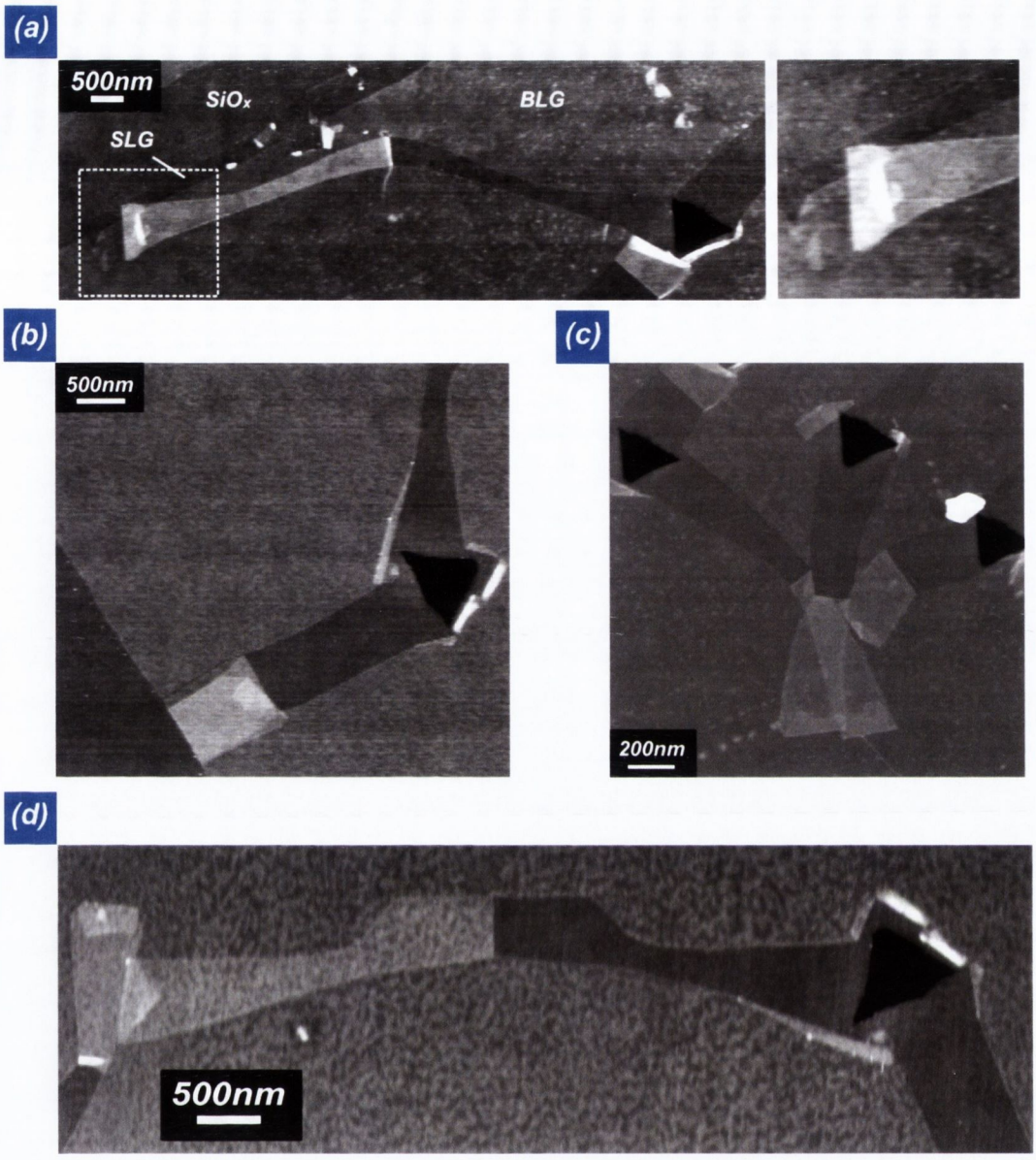

Figure 4.3.11: Tapping mode AFM height images of (a) and (b) bi-layer folded ribbons which interacted with the edge of a graphene sheet, (c) bi-layer folded ribbons which grew over one another and (d) two bi-layer folded ribbons which interacted with one another causing rotation of one of the folded ribbons.

Shown in Figure 4.3.12 is an example of an indentation which resulted in an alternative folded structure on a single layer of graphene. The AFM image in Figure 4.3.12 (a) shows the typical folded ribbon structure on the lower side of the impression however on the upper side of the impression a nearly perfectly rectangular folded structure was formed, which is approximately three times smaller than the length of the trench in the SiO_x from which it was formed. The growth of both of the folded structures can be seen by the AFM image in Figure 4.3.12 (b) which is due to the laser irradiation from performing Raman spectroscopy. The folded structure on the upper side of the impression remained approximately three times longer than the trench exposing the SiO_x. The sharp corners on the leading edge and the dimensions of the structure suggest that the folded ribbon is folded internally as shown by the schematic in Figure 4.3.12 (e). The conformal contact between the ribbon and the underlying flake can be seen by the AFM in Figure 4.3.12 (c) since the undulations which are present on the underlying flake are also present on the folded structure. The doubly folded structure grew by approximately 5μm while the ribbon like structure only grew by approximately 1μm under the same environmental conditions. The nearly parallel tapering angle of the doubly folded structure ensures that the reduction of the elastic energy was negligible and that the growth was facilitated by changes in the surface areas alone. The near parallel fracture paths along the lattice in comparison to the fracture paths on the lower side of the impression, as well as the diverging fracture paths shown in Figure 4.3.9 (d), suggest that the self assembly process may provide a route for controlling the edge structure in fabricated graphene.

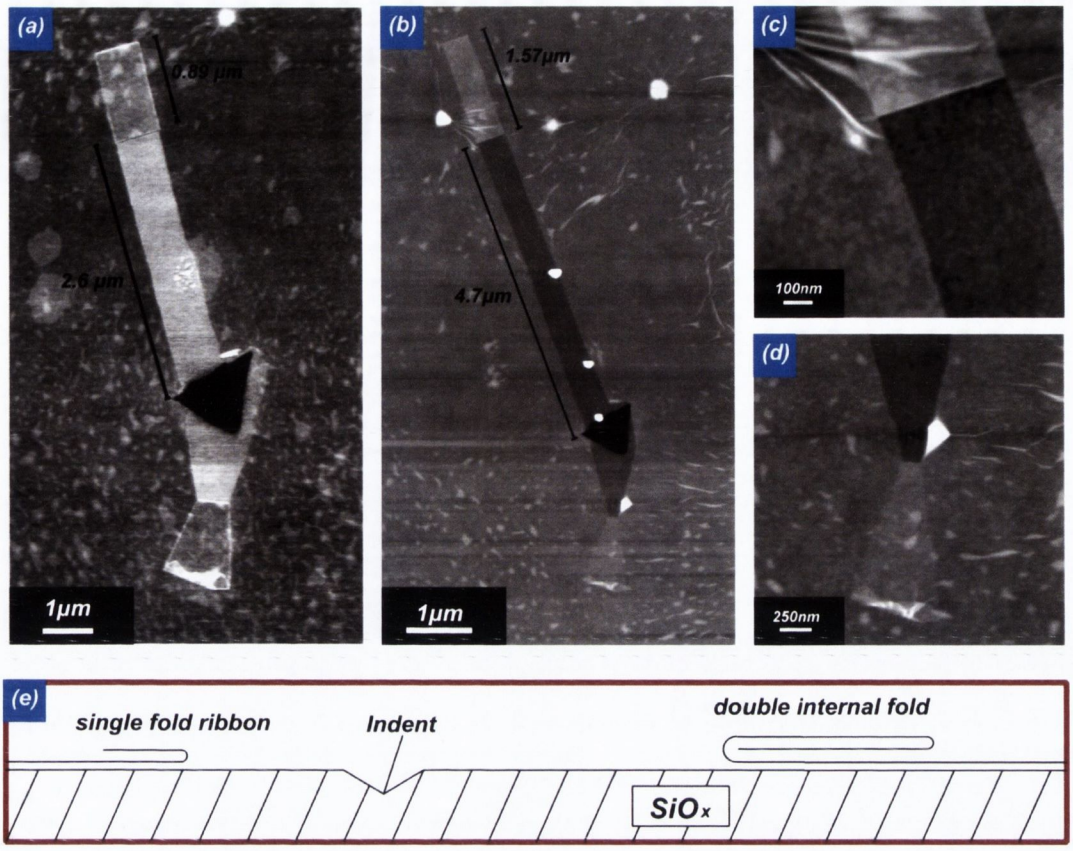

Figure 4.3.12: An example of an alternatively folded structure produced on a single layer of graphene. (a) Tapping mode AFM height image of the folded structures after nucleation, (b) Tapping mode AFM height image of the folded structures after Raman spectroscopy, (c) zoomed in tapping mode AFM image of the folded ribbon on the upper side of the impression, (d) zoomed in tapping mode AFM image of the folded ribbon on the lower side of the impression and (e) schematic representation of the folded structures.

4.3.4 Raman spectroscopy

The optical microscopy image shown in Figure 4.3.13 (a) is of a bi-layer mechanically exfoliated graphene flake. Within the flake is a thicker tri-layer strip which was left naturally from the mechanical exfoliation. Also within the flake are two folded ribbons nucleated from a single nanoindentation. Raman spectroscopy was performed within the area shown by the red box within Figure 4.3.13 (a). The relative G band intensity map shown in Figure 4.3.13 (b) is illustrative of the dependency on the thickness of the graphene with thicker areas producing a higher intensity which is due to an increasing probability of G band scattering with increasing thickness. The qualitatively different behaviour of the 2D band is illustrated in the 2D intensity map given in Figure 4.3.13 (c) with a comparable intensity between the underlying flake and the thicker tri layer strip and

approximately double the intensity within the folded ribbon. The G to 2D band intensity ratios can be seen in Figure 4.3.13 (e) with comparable ratios of 1.81 and 2 for the folded ribbon and the underlying flake and a much higher ratio of 2.7 for the tri-layer strip. The map of the FWHM of the 2D band shows significant broadening within the tri-layer strip with a value of 59 cm^{-1} while the map shows less broadening within the folded ribbon with a FWHM of 54 cm^{-1} which is comparable to the FWHM of the underlying flake of 52 cm^{-1}. The significant broadening of the 2D band in the thicker tri-layer strip is indicative of AB Bernal stacking of the graphene layers. This AB stacking causes an alteration of the band structure which results in an increase in the number of Raman active processes within the 2D band which result in different Raman shifts thereby broadening the 2D band. On the other hand, non AB stacking of graphene results in weak interaction between the electronic states of each layer leaving the scattering process unaltered, which can be seen by the nearly identical shape of the 2D band of the underlying flake and the folded ribbon shown in Figure 4.3.13 (f). The Raman spectroscopy confirms that the folded ribbon is incommensurate with the underlying flake. We suggest that the incommensurability produces easy sliding between the folded ribbon and the flake thereby allowing the growth to occur.

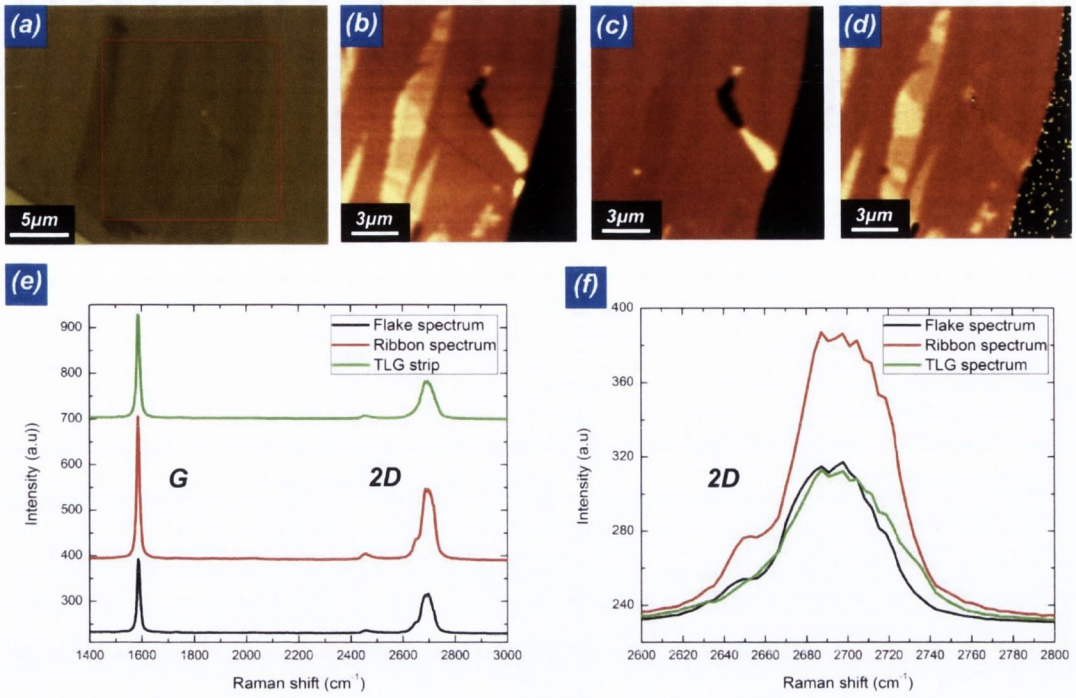

Figure 4.3.13: Experimental verification of the incommensurate staking of a folded ribbon via Raman spectroscopy. (a) Optical image of the underlying flake with a thicker strip and two folded ribbons, (b) G band intensity map, (c) 2D band intensity map, (d) map of the FWHM of the 2D band, (e) the spectral data showing the G and 2D band of the underlying flake, the thicker strip and the folded ribbon shown in black, green and red respectively, (f) the spectral data of the 2D band of the flake the thicker strip and the folded ribbon shown in black, green and red respectively.

The optical microscopy image shown in Figure 4.3.14 (a) is of a bi-layer graphene flake with a folded ribbon which has undergone a rotation of approximately 35^0 with respect to the direction of growth. The G band intensity map shown in Figure 4.3.14 (b) is qualitatively similar to the previous example with the thicker areas of graphene producing a relatively higher G band intensity. The 2D band intensity map shown in Figure 4.3.14 (c) indicates uniformity in the relative intensity between the folded ribbon and the underlying flake. The ratio of the G to 2D band intensities can be seen in Figure 4.3.14 (e) with a ratio of 1.5 and 2 for the underlying flake and the folded ribbon respectively. The map of the FWHM of the 2D band can be seen in Figure 4.3.14 (d) which shows significant broadening of the 2D band within the folded ribbon in comparison to the underling flake with values of 52 cm^{-1} and 59 cm^{-1} respectively. In contrast to the previous example the spectroscopy suggests that the folded ribbon is commensurately stacked. We suggest that folded ribbon was initially incommensurately stacked however during the growth the folded ribbon rotated through approximately 35^0 which resulted in the folded ribbon falling into commensurability with the underlying flake after which no further growth is possible.

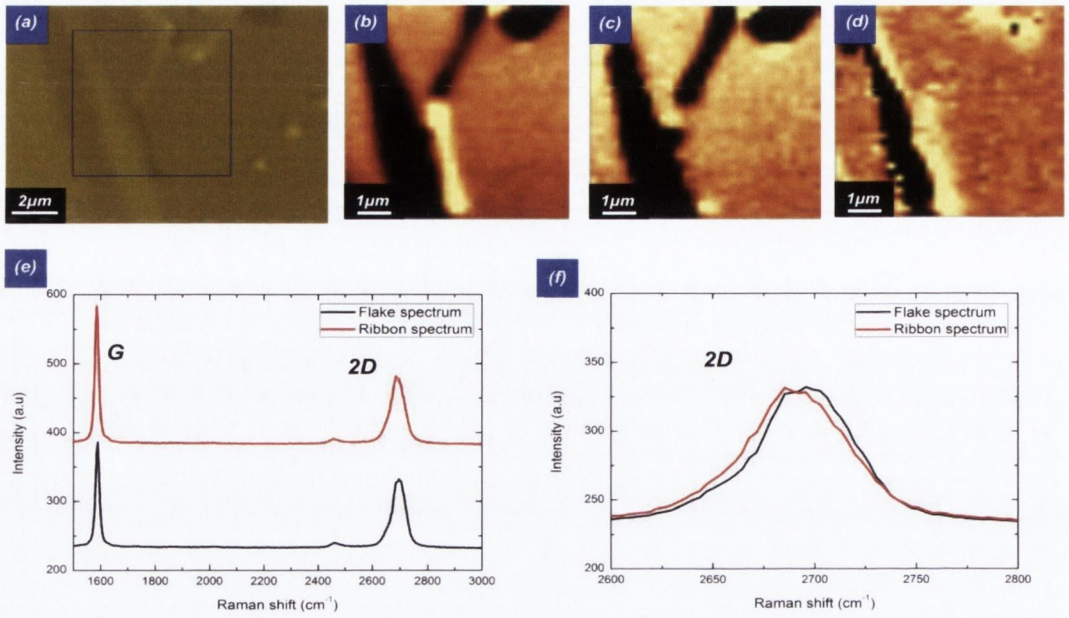

Figure 4.3.14: Experimental verification of a folded ribbon which is commensurate with the underlying flake. (a) Optical image of the flake and the folded ribbon, (b) G band intensity map, (c) 2D band intensity map, (d) map of the FWHM of the 2D band, (e) spectral data of the ribbon and the underlying flake shown in red and black respectively, and (f) the spectral data of the 2D band on the ribbon and the underlying flake, shown in red and black respectively.

4.4 Conclusion

We have observed the spontaneous and directed reorganisation of graphene into self assembled folded structures. The reorganisation can be viewed as a thermodynamic process which is nucleated along a free edge on the graphene sheet, which must be folded either by an external load or by thermal fluctuations. The assembly process may then progress by an overall reduction in the free energy within the flake. The majority of the folded structures were nucleated by nanoindentation, resulted in the characteristic ribbon structure with converging tapering. We suggest that the tapering is determined by the maximal energy release rate. A general trend of increasing tapering angle with decreasing thickness has been found with a large increase in the scatter of the tapering angles with decreasing thickness. This scatter may be due to the discrete fracture paths on either sides of the fold. The tapering angles of the single layer ribbons ranged from 3^0 and 34^0 which may reflect the preferred zig-zag and armchair tearing directions. The indentations have produced a variety of structures which involve multiple folding of the ribbons. The growth of the folded ribbons has been shown to be extremely sensitive to the interactions between the ribbon and the underlying flake since no growth has been observed beyond the edge of

the flake and the interaction with an external boundary has resulted in the distortion of the folded ribbons. Raman spectroscopy has revealed the incommensurate stacking between the ribbon and the underlying flake. We suggest that the growth of the ribbons is only possible between incommensurate contacts. The initial growth rates of the folded ribbons are typically rapid which remains largely unmeasured due to the experimental constraint of the relatively slow measurements during AFM scanning. The long term growth rates typically decay exponentially after the initial rapid growth rate. This suggests that the initial and long term growth rates are limited by different processes. We suggest that the large growth rates are limited by the energy dissipation of the sliding between the ribbon and the underlying flake however at slower growth rates the growth rate may be limited by the fracture rate of the C-C bonds along the graphene lattice. The folded structures have shown sensitivity to thermal treatment which has been imposed by either laser irradiation via Raman spectroscopy, or by direct heating within an oven. The thermal treatment of previously static folded ribbons has resulted in large growths which may be due to both increased thermal energy within the crack front and a mismatch between the thermal expansion coefficients of SiO_x and graphene.

Chapter 5: Summary and Future Work

Summary and future work

The general focus of the thesis has been the investigation and experimental characterisation of new ways in which atomic scale properties can directly influence the behaviour of nano to meso scale contacts in room temperature ambient conditions. This has been studied in three ways and the major findings of the thesis are summarised as follows

1) A crystallographic orientation dependence on the friction of nano to meso scale, single asperity contacts in single crystal Ni in air was found, where easy slip was found along the close packed [110] direction.

2) The role of graphene as a protective lubricating coating in nano to mesoscale contacts was investigated and even a single layer of graphene placed between the contacts was found to provide excellent lubrication.

3) We discovered and characterised a novel self-assembly phenomenon in graphene which resembles a solid state version of the wetting of liquids on surfaces. The phenomenon may extend to a broad class of 2D materials, and have uses in lithography and nano-electromechanical devices (NEMS). The phenomenon may also provide a new route for studying the mechanical of 2D materials such as folding, fracture and adhesion.

The 3D nanocontact system has been proven to be a useful tool for investigating the tribological properties of materials by imposing a frequency specific, phase sensitive, sinusoidal oscillation in the lateral direction during conventional indentation. This allows for the elastic stiffness and the damping coefficient of the contact to be measured in the lateral direction throughout conventional indentation. This differs from other tribological experiments because the contact size range from 10's to 1000 nm with measureable stiffness's ranging from 10 N/m to 10^6 N/m on single asperity contacts. Other triboligcal instruments such as FFM or surface force apparatus (SFA) typically measure lateral stiffness's between 10-10^2 N/m and larger than 10^6 N/m respectively. The small scale of the lateral oscillation, ranging from 1 to 2 nm in the experiments described within the thesis, is much smaller than the contact sizes. This differs from other tribological instruments such as FFM where the contact is typically scanned a large distance with respect to the contact size. The 3D nanocontact system offers a unique opportunity to

investigate the role of shear stress in nano to meso scale contacts under increasing contact sizes and normal contact pressures. The instrument also offers a unique opportunity to study the transition from a sliding to a fully elastic contact and the role of discrete plasticity in this transition. Further experiments on single crystals and on amorphous materials may provide insight into the role of discrete plasticity in nano to meso scale contacts under shear stress. The instrument offers a wide variety of testing parameters such as the amplitude and frequency of the lateral oscillation as well as the normal loading conditions which could be used to probe the length and time scale dependencies of the lateral contact stiffness.

The 3D nano contact system was used to investigate the friction anisotropy of the single crystal Ni in air. The frequency specific, phase sensitive sinusoidal oscillation in the lateral direction enabled the measurement of the elastic stiffness of the contact during conventional Berkovich quasi static indentation. The contact was modelled as a spherically symmetrical partial microslip contact with an inner stick zone resulting in elastic contributions and an outer slip zone resulting in energy dissipation during the interfacial sliding. The transition from a full slip condition, during the initial contact, to the fully elastic contact at large depths was investigated and using the bi-modal interfacial shear stress distribution, developed by Yan Fei Gao, the interfacial shear strength was obtained. A significant, 40% increase in the interfacial shear strength was found as the crystal was rotated from the [110] to the [001] direction.

The 3D contact system has also been used to investigate the role of graphene and other quasi 2D sheets as a protective lubricating coating in nano to meso-scale contacts. The excellent lubrication properties of graphene have been demonstrated by the significant decrease in the lateral stiffness, prior to rupture. The lubrication is maintained even at large average contacting pressures of up to 10 GPa which is large enough to cause plastic deformation of the substrate. Bi and tri-layer graphene were found to have superior lubricating properties. Significantly higher lateral stiffness's, at all depths prior to the critical rupture, was measured on the single layer contacts in comparison to the contacts on bi and tri-layer graphene. We suggest that the reduced lateral stiffness of the contacts in few layer graphene is due to the weak Van der Waals interactions between graphene layers. Single layer graphene, in direct contact with the tip and the substrate, results in different interactions with an increased resistance within the contact at higher contacting pressures. With sufficient contacting pressures and/or the number of lateral oscillation cycles the failure of the graphene layer is observed by the discontinuous jump in the lateral stiffness. The origin of the critical rupture is not clear however the large range of depths and loads at which the rupture occurs indicates that the process may be sensitive to

conditions such as contamination, local substrate roughness and/or the initial state of stress within the graphene sheet. Further experiments will help to provide insight into the origin of the rupture by varying the loading rates which will result in an effective increase in the number of cycles for any given depth. This will provide evidence that the rupture is due to a wear process. Alternatively varying the lateral oscillation amplitude may also provide evidence that the critical rupture is due to wear. Other quasi 2D sheets such as hBN, MoS_2, Bi_2Se_3 etc should also exhibit layer dependency in the tribological properties which may depend on the strong in plane bonding and the Van der Waals interaction between layers. The tribological properties are also expected to depend on the substrate properties such as roughness and adhesion etc. Varying the substrate will provide insight into the lubrication and tribological properties quasi 2D sheets on nano to meso scale contacts.

The fretting action of lateral oscillations, imposed during the indentation testing on graphene, resulted in folded structures at the periphery of the contact which led to the discovery of a new self assembly process in graphene. The self-assembly phenomenon requires a free edge within the flake which must be folded, either directly by an external force or through thermal energy. Once the fold has been nucleated the self assembly process may proceed through a minimisation of the free energy of the flake. The process involves sliding, fracture and the relaxation of elastic strain energy within the fold. Using the available values, within the literature, of the surface interactions, the elastic strain energy and the cost of fracturing the graphene lattice we have formulated a theory which predicts the energetic favourability of the growth of the folded structures. Further investigation and modelling may provide more accurate determination of the thermodynamic potentials which drive the growth. The orientation of the graphene lattices during the experiments, described within chapter 4, were unknown which presents a significant challenge in understanding fracture paths along the graphene lattices. Future experiments may require knowledge of the orientation of the lattices which could be achieved by atomic scale imaging via AFM, STM or TEM. This may provide insight into the fracture path selection. Atomic scale imaging of the edge roughness of the fracture paths will also provide insight into the C-C bond breaking process along the lattice. In this way the self-assembly process may be used to understand and control the edge structure in fabricated graphene structures such as nano ribbons. The self-assembly process has shown sensitivity to substrate interactions. Nucleating the self-assembly process on a variety of substrates may be useful in studying the Van der Waals interactions in graphene sheets.

References

1. Geim, A.K. and K.S. Novoselov, *The rise of graphene.* Nature Materials, 2007. **6**(3): p. 183-191.
2. Novoselov, K.S., et al., *Two-dimensional gas of massless Dirac fermions in graphene.* Nature, 2005. **438**(7065): p. 197-200.
3. Bolotin, K.I., et al., *Observation of the fractional quantum Hall effect in graphene.* Nature, 2009. **462**(7270): p. 196-199.
4. Du, X., et al., *Approaching ballistic transport in suspended graphene.* Nature Nanotechnology, 2008. **3**(8): p. 491-495.
5. Dean, C.R., et al., *Boron nitride substrates for high-quality graphene electronics.* Nat Nano, 2010. **5**(10): p. 722-726.
6. Geim, A.K. and I.V. Grigorieva, *Van der Waals heterostructures.* Nature, 2013. **499**(7459): p. 419-425.
7. Lee, C., et al., *Measurement of the elastic properties and intrinsic strength of monolayer graphene.* Science, 2008. **321**(5887): p. 385-388.
8. Lee, C., et al., *Elastic and frictional properties of graphene.* Physica Status Solidi B-Basic Solid State Physics, 2009. **246**(11-12): p. 2562-2567.
9. Lee, C., et al., *Frictional Characteristics of Atomically Thin Sheets.* Science, 2010. **328**(5974): p. 76-80.
10. van Wijk, M.M.F., *Minimal graphene thickness for wear protection of diamond.* arXiv, 2014.
11. Persson, B.N.J. and F. Mugele, *Squeeze-out and wear: fundamental principles and applications.* Journal of Physics: Condensed Matter, 2004. **16**(10): p. R295.
12. Hernandez, Y., et al., *High-yield production of graphene by liquid-phase exfoliation of graphite.* Nat Nano, 2008. **3**(9): p. 563-568.
13. Amontons, G., *De la resistance caus''ee dans les machines.* memoirs de lacademie royale, 1706. **A**: p. 257.
14. Bowden, F.P. and D. Tabor, *The Area of Contact between Stationary and between Moving Surfaces*. Vol. 169. 1939. 391-413.
15. Bowden, F.P. and L. Leben, *The Nature of Sliding and the Analysis of Friction.* Proceedings of the Royal Society of London. Series A, Mathematical and Physical Sciences, 1939. **169**(938): p. 371-391.
16. F.P. Bowden, D.T., *Mechanism of metallic friction.* Nature, 1942(150): p. 197-199
17. Park, J.Y. and M. Salmeron, *Fundamental Aspects of Energy Dissipation in Friction.* Chemical Reviews, 2013. **114**(1): p. 677-711.
18. Binnig, G., C.F. Quate, and C. Gerber, *Atomic Force Microscope.* Physical Review Letters, 1986. **56**(9): p. 930-933.
19. Mate, C.M., et al., *Atomic-scale friction of a tungsten tip on a graphite surface.* Physical Review Letters, 1987. **59**(17): p. 1942-1945.
20. Carpick, R.W., et al., *Measurement of interfacial shear (friction) with an ultrahigh vacuum atomic force microscope.* Journal of Vacuum Science & Technology B, 1996. **14**(2): p. 1289-1295.
21. Xiao, X., et al., *Chain Length Dependence of the Frictional Properties of Alkylsilane Molecules Self-Assembled on Mica Studied by Atomic Force Microscopy.* Langmuir, 1996. **12**(2): p. 235-237.
22. Tomlinson.G.A, *A molecular theory of friction.* Philisophical Mag, 1929. **7**: p. 905.
23. Bluhm, H., et al., *Anisotropy of sliding friction on the triglycine sulfate (010) surface.* Applied Physics A, 1995. **61**(5): p. 525-533.
24. Mancinelli, C.M. and A.J. Gellman, *Friction Anisotropy at Pd(100)/Pd(100) Interfaces.* Langmuir, 2004. **20**(5): p. 1680-1687.

25. Sheehan, P.E. and C.M. Lieber, *Nanotribology and Nanofabrication of MoO3 Structures by Atomic Force Microscopy.* Science, 1996. **272**(5265): p. 1158-1161.
26. Hirano, M. and K. Shinjo, *Atomistic locking and friction.* Physical Review B, 1990. **41**(17): p. 11837-11851.
27. Hirano, M., et al., *Anisotropy of frictional forces in muscovite mica.* Physical Review Letters, 1991. **67**(19): p. 2642-2645.
28. Dietzel, D., et al., *Scaling Laws of Structural Lubricity.* Physical Review Letters, 2013. **111**(23): p. 235502.
29. Dietzel, D., et al., *Frictional Duality Observed during Nanoparticle Sliding.* Physical Review Letters, 2008. **101**(12): p. 125505.
30. Hölscher, H., A. Schirmeisen, and U.D. Schwarz, *Principles of atomic friction: from sticking atoms to superlubric sliding*. Vol. 366. 2008. 1383-1404.
31. Hirano, M.a.S., Kazumasa and Kaneko, Reizo and Murata, Yoshitada, *Observation of Superlubricity by Scanning Tunneling Microscopy.* Phys. Rev. Lett., 1997. **78**(8): p. 1448--1451.
32. Bruschi, L.a.F., G. and Pontarollo, A. and Mistura, G. and Torre, B. and Buatier de Mongeot, F. and Boragno, C. and Buzio, R. and Valbusa, U., *Structural Depinning of Ne Monolayers on Pb at <6K.* Phys. Rev. Lett., 2006. **96**(21): p. 216101.
33. Liu, Z., et al., *Observation of Microscale Superlubricity in Graphite.* Physical Review Letters, 2012. **108**(20).
34. Yang, J., et al., *Observation of High-Speed Microscale Superlubricity in Graphite.* Physical Review Letters, 2013. **110**(25).
35. Zheng, Q. and Z. Liu, *Experimental advances in superlubricity.* Friction, 2014. **2**(2): p. 182-192.
36. Liu, Z., et al., *Interlayer shear strength of single crystalline graphite.* Acta Mechanica Sinica, 2012. **28**(4): p. 978-982.
37. Klein, J. and E. Kumacheva, *Confinement-Induced Phase Transitions in Simple Liquids.* Science, 1995. **269**(5225): p. 816-819.
38. Zaidi, H., F. Robert, and D. Paulmier, *Influence of adsorbed gases on the surface energy of graphite: consequences on the friction behaviour.* Thin Solid Films, 1995. **264**(1): p. 46-51.
39. Novoselov, K.S., et al., *Two-dimensional atomic crystals.* Proceedings of the National Academy of Sciences of the United States of America, 2005. **102**(30): p. 10451-10453.
40. Kim, K., et al., *Ripping Graphene: Preferred Directions.* Nano Letters, 2011. **12**(1): p. 293-297.
41. Kwon, S., et al., *Enhanced Nanoscale Friction on Fluorinated Graphene.* Nano Letters, 2012. **12**(12): p. 6043-6048.
42. Lin, L.-Y., et al., *Friction and wear characteristics of multi-layer graphene films investigated by atomic force microscopy.* Surface and Coatings Technology, 2011. **205**(20): p. 4864-4869.
43. Shin, Y.J., et al., *Frictional characteristics of exfoliated and epitaxial graphene.* Carbon, 2011. **49**(12): p. 4070-4073.
44. Woods, C.R., et al., *Commensurate-incommensurate transition in graphene on hexagonal boron nitride.* Nat Phys, 2014. **10**(6): p. 451-456.
45. Tai, Z., et al., *Tribological Behavior of UHMWPE Reinforced with Graphene Oxide Nanosheets.* Tribology Letters, 2012. **46**(1): p. 55-63.
46. Dieter, G.E., *Mechanical Metallurgy*. 1998.
47. Fisher-Crips, A.C., *Introduction to contact mechanics*. 2007.
48. Mo, Y.F., K.T. Turner, and I. Szlufarska, *Friction laws at the nanoscale.* Nature, 2009. **457**(7233): p. 1116-1119.

49. Adams, G.G., S. Müftü, and N.M. Azhar, *A Scale-Dependent Model for Multi-Asperity Contact and Friction.* Journal of Tribology, 2003. **125**(4): p. 700-708.
50. Dayo, A., W. Alnasrallah, and J. Krim, *Superconductivity-Dependent Sliding Friction.* Physical Review Letters, 1998. **80**(8): p. 1690-1693.
51. Budakian, R. and S.J. Putterman, *Correlation between Charge Transfer and Stick-Slip Friction at a Metal-Insulator Interface.* Physical Review Letters, 2000. **85**(5): p. 1000-1003.
52. Gao, Y.F., et al., *Nanoscale incipient asperity sliding and interface micro-slip assessed by the measurement of tangential contact stiffness.* Scripta Materialia, 2006. **55**(7): p. 653-656.
53. Kim, S.H., D.B. Asay, and M.T. Dugger, *Nanotribology and MEMS.* Nano Today, 2007. **2**(5): p. 22-29.
54. Szlufarska, I., M. Chandross, and R.W. Carpick, *Recent advances in single-asperity nanotribology.* Journal of Physics D: Applied Physics, 2008. **41**(12): p. 123001.
55. Dienwiebel, M., et al., *Superlubricity of Graphite.* Physical Review Letters, 2004. **92**(12): p. 126101.
56. E. Meyer, R.M.O., K. Dransfeld, T Gyalog, *Nanoscience: Friction and Rheology on the Nanometer Scale*. 1998.
57. Carpick, R.W. and M. Salmeron, *Scratching the Surface: Fundamental Investigations of Tribology with Atomic Force Microscopy.* Chemical Reviews, 1997. **97**(4): p. 1163-1194.
58. Hay, J., *INTRODUCTION TO INSTRUMENTED INDENTATION TESTING.* Experimental Techniques, 2009. **33**(6): p. 66-72.
59. Cross, et al., *Plasticity, healing and shakedown in sharp-asperity nanoindentation.* Nature Materials, 2006. **5**(5): p. 370.
60. Cross, G.L.W., *The production of nanostructures by mechanical forming.* Journal of Physics D: Applied Physics, 2006. **39**(20): p. R363.
61. Rowland, H.D., et al., *Measuring Glassy and Viscoelastic Polymer Flow in Molecular-Scale Gaps Using a Flat Punch Mechanical Probe.* Acs Nano, 2008. **2**(3): p. 419-428.
62. Oliver, W.C. and G.M. Pharr, *An improved technique for determining hardness and elastic modulus using load and displacement sensing indentation experiments.* Journal of Materials Research, 1992. **7**(06): p. 1564-1583.
63. Sneddon, I.N., *The relaxation between between load and penetration in the axisymmetric Boussinisq problem for a punch of arbitrary profile* Int. J Engng Sci, 1965. **3**: p. 47-57.
64. Johnson, K.L., *Contact Mechanics*. 1987.
65. Hay, J., P. Agee, and E. Herbert, *CONTINUOUS STIFFNESS MEASUREMENT DURING INSTRUMENTED INDENTATION TESTING.* Experimental Techniques, 2010. **34**(3): p. 86-94.
66. Herbert, E.G., et al., *Measuring the constitutive behavior of viscoelastic solids in the time and frequency domain using flat punch nanoindentation.* Journal of Materials Research, 2009. **24**(03): p. 626-637.
67. Lucas, B.N., J.C. Hay, and W.C. Oliver, *Using multidimensional contact mechanics experiments to measure Poisson's ratio.* Journal of Materials Research, 2004. **19**(1): p. 58-65.
68. Annett, J., et al., *Mesoscale friction anisotropy revealed by slidingless tests.* Journal of Materials Research, 2011. **26**(18): p. 2373-2378.
69. B. N. Lucas*, J.C.H., and W. C. Oliver**, *Using multi-dimensional contact mechanics experiments to measure Poisson's ratio of porous low-k films.* Materials research society, 2003.

70. Carpick, R.W., D.F. Ogletree, and M. Salmeron, *Lateral stiffness: A new nanomechanical measurement for the determination of shear strengths with friction force microscopy.* Applied Physics Letters, 1997. **70**(12): p. 1548-1550.
71. Ferrari, A.C., et al., *Raman Spectrum of Graphene and Graphene Layers.* Physical Review Letters, 2006. **97**(18): p. 187401.
72. Ferrari, A.C. and D.M. Basko, *Raman spectroscopy as a versatile tool for studying the properties of graphene.* Nat Nano, 2013. **8**(4): p. 235-246.
73. DasA, et al., *Monitoring dopants by Raman scattering in an electrochemically top-gated graphene transistor.* Nat Nano, 2008. **3**(4): p. 210-215.
74. Casiraghi, C., et al., *Raman Spectroscopy of Graphene Edges.* Nano Letters, 2009. **9**(4): p. 1433-1441.
75. Yu, T., et al., *Raman Mapping Investigation of Graphene on Transparent Flexible Substrate: The Strain Effect.* The Journal of Physical Chemistry C, 2008. **112**(33): p. 12602-12605.
76. Hao, Y., et al., *Probing Layer Number and Stacking Order of Few-Layer Graphene by Raman Spectroscopy.* Small, 2010. **6**(2): p. 195-200.
77. Ni, Z., et al., *Reduction of Fermi velocity in folded graphene observed by resonance Raman spectroscopy.* Physical Review B, 2008. **77**(23): p. 235403.
78. Ananthakrishna, G. and J. Kumar, *Correlation between stick-slip frictional sliding and charge transfer.* Physical Review B, 2010. **82**(7).
79. Ko, J.S. and A.J. Gellman, *Friction anisotropy at Ni(100)/Ni(100) interfaces.* Langmuir, 2000. **16**(22): p. 8343-8351.
80. Gao, Y., *A Peierls perspective on mechanisms of atomicfriction.* Journal of the Mechanics and Physics of Solids, 2010. **58**(12): p. 2023-2032.
81. Savkoor, A.R., *Dry adhesive friction of elastomers*. 1987, Dissertation, Delft University of Technology.
82. Bhushan, B., J.N. Israelachvili, and U. Landman, *NANOTRIBOLOGY - FRICTION, WEAR AND LUBRICATION AT THE ATOMIC-SCALE.* Nature, 1995. **374**(6523): p. 607-616.
83. Lee, C., et al., *Elastic and frictional properties of graphene.* physica status solidi (b), 2009. **246**(11-12): p. 2562-2567.
84. Lin, L.Y., et al., *Friction and wear characteristics of multi-layer graphene films investigated by atomic force microscopy.* Surface & Coatings Technology, 2011. **205**(20): p. 4864-4869.
85. Li, Q., et al., *Substrate effect on thickness-dependent friction on graphene.* physica status solidi (b), 2010. **247**(11-12): p. 2909-2914.
86. Choi, J.S., et al., *Friction Anisotropy-Driven Domain Imaging on Exfoliated Monolayer Graphene.* Science, 2011. **333**(6042): p. 607-610.
87. Ko, J.-H., et al., *Nanotribological Properties of Fluorinated, Hydrogenated, and Oxidized Graphenes.* Tribology Letters, 2013. **50**(2): p. 137-144.
88. Dong, Y., X. Wu, and A. Martini, *Atomic roughness enhanced friction on hydrogenated graphene.* Nanotechnology, 2013. **24**(37): p. 375701.
89. Filleter, T., et al., *Friction and Dissipation in Epitaxial Graphene Films.* Physical Review Letters, 2009. **102**(8): p. 086102.
90. Dong, Y., *Effects of substrate roughness and electron–phonon coupling on thickness-dependent friction of graphene.* Journal of Physics D: Applied Physics, 2014. **47**(5): p. 055305.
91. Barnard, A.S., *A Thermodynamic Model for the Shape and Stability of Twinned Nanostructures.* The Journal of Physical Chemistry B, 2006. **110**(48): p. 24498-24504.

92. Ringe, E., R.P. Van Duyne, and L.D. Marks, *Kinetic and Thermodynamic Modified Wulff Constructions for Twinned Nanoparticles.* The Journal of Physical Chemistry C, 2013. **117**(31): p. 15859-15870.
93. Shibuta, Y. and J.A. Elliott, *Interaction between two graphene sheets with a turbostratic orientational relationship.* Chemical Physics Letters, 2011. **512**(4–6): p. 146-150.
94. Feng, X.F., et al., *Superlubric Sliding of Graphene Nanoflakes on Graphene.* Acs Nano, 2013. **7**(2): p. 1718-1724.
95. Lebedeva, I.V., et al., *Fast diffusion of a graphene flake on a graphene layer.* Physical Review B, 2010. **82**(15): p. 155460.
96. Yang, J., et al., *Observation of High-Speed Microscale Superlubricity in Graphite (vol 110, 255504, 2013).* Physical Review Letters, 2013. **111**(2).
97. Griffith, A.A., *The Phenomena of Rupture and Flow in Solids*. Vol. 221. 1921. 163-198.
98. Lawn, B., *Fracture of Brittle Solids*. 2nd Edition ed. 1993.
99. Eyring, H., *Viscosity, Plasticity, and Diffusion as Examples of Absolute Reaction Rates.* The Journal of Chemical Physics, 1936. **4**(4): p. 283-291.
100. K.Krausz, A.S.K., *Fracture Kinetics of Crakc Growth*. Vol. 1. 1988.
101. Schuh, C.A. and A.C. Lund, *Application of nucleation theory to the rate dependence of incipient plasticity during nanoindentation.* Journal of Materials Research, 2004. **19**(07): p. 2152-2158.
102. Schuh, C.A., J.K. Mason, and A.C. Lund, *Quantitative insight into dislocation nucleation from high-temperature nanoindentation experiments.* Nat Mater, 2005. **4**(8): p. 617-621.
103. Finnis, M.W., *The theory of metal - ceramic interfaces.* Journal of Physics: Condensed Matter, 1996. **8**(32): p. 5811.
104. He, Y., et al., *Anomalous interface adhesion of graphene membranes.* Sci. Rep., 2013. **3**.
105. Koenig, S.P., et al., *Ultrastrong adhesion of graphene membranes.* Nat Nano, 2011. **6**(9): p. 543-546.
106. Bunch, J.S. and M.L. Dunn, *Adhesion mechanics of graphene membranes.* Solid State Communications, 2012. **152**(15): p. 1359-1364.
107. Zong, Z., et al., *Direct measurement of graphene adhesion on silicon surface by intercalation of nanoparticles.* Journal of Applied Physics, 2010. **107**(2): p. 026104.
108. Gao, W. and R. Huang, *Effect of surface roughness on adhesion of graphene membranes.* Journal of Physics D: Applied Physics, 2011. **44**(45): p. 452001.
109. Chen, X., et al., *Graphene folding on flat substrates.* Journal of Applied Physics, 2014. **116**(16): p. 164301.
110. Sen, D., et al., *Tearing Graphene Sheets From Adhesive Substrates Produces Tapered Nanoribbons.* Small, 2010. **6**(10): p. 1108-1116.
111. Hamm, E., et al., *Tearing as a test for mechanical characterization of thin adhesive films.* Nat Mater, 2008. **7**(5): p. 386-390.
112. Gong, L., et al., *Reversible Loss of Bernal Stacking during the Deformation of Few-Layer Graphene in Nanocomposites.* Acs Nano, 2013. **7**(8): p. 7287-7294.
113. Huang, X., et al., *Chemomechanics control of tearing paths in graphene.* Physical Review B, 2012. **85**(19): p. 195453.
114. Stolyarova, E., et al., *Observation of Graphene Bubbles and Effective Mass Transport under Graphene Films.* Nano Letters, 2008. **9**(1): p. 332-337.